Massive Star Formation and Molecular Cloud Core: A Case Study of W49A

大質量星形成と分子雲コア W49Aの場合について

宮脇亮介

Ryosuke Miyawaki

Massive Star Formation and Molecular Cloud Cores:

A Case Study of W49A

Ryosuke MIYAWAKI

Department of Science Education,
Fukuoka University of Education

A Thesis Presented
by
Ryosuke Miyawaki
to
the Faculty of the Graduate School of the University of Tokyo
in Partial Fulfillment of the Requirements
for the Degree of Doctor (Science)
December 1994

ACKNOWLEDGMENTS

First of all I would like to thank Dr. Testuo Hasegawa and Dr. Masahiko Hayashi for their continuous encouragement and useful comments on this work. They are my colaborators and, at the same time, my teachers on radio astronomy. They taught me many things when we wrote previous papers. I also thank for their critical readings of previous draft of this article.

I am grateful to all the staff of Nobeyama Radio Observatory for operating the 45-m telescope and Nobeyama Millimeter Array. Dr. Yasuhiro Murata and Dr. Hideyuki Kobayashi, who moved to ISAS, showed me how to use AIPS package for reducing of NMA data. I would like to thank Dr. Ryohei Kawabe who helped me for data reduction of CS observations with NMA presented in Chapter 5. Observations using JCMT are supported by Dr. Testuo Hasegawa, Dr. Masahiko Hayashi, and Dr. Saeko, S. Hayashi.

Professor Tsuneaki Daishido of Waseda University taught me astronomy and astrophysics in the undergraduate course, and he gave me a chance to handle a radio telescope with 8 element phased array. This experience lead me to take a course of astronomy. I also thank to the staff of Tokyo Gakugei University, especially to the late Prof. Mahiro Shimoda for his encouragement when I was in the graduate course. Prof. Fumio Sato of Tokyo Gakugei University gave me the telescope time of ^{12}CO observations with the 45-m telescope. I also thank to participants of the seminar entitled "Radio Astronomy" held at the National Astronomical Observatory, especially to Prof. Yoshiaki Sofue for his useful discussion on star formation.

Training with the 6-m millimeter telescope brought me to an exciting world of astronomy. I studied principals of radio telescopes by using the 6-m telescope. I would like to thank to Dr. Toshihiro Omodaka and others for operating the 6-m telescope and for discussing with me on its results.

I would like to thank the staff of Fukuoka University of Education for encouraging me to do research in radio astronomy. Prof. Masanori Hirai in particular encouraged me to continue this work. When I had troubles on software in a work station, Dr. Osamu Kanamitu kindly helped me to solve the problems.

Finally, I would like to thank my wife, my son, and my parents who have always been encouraging me to do what I would like to do.

TABLE OF CONTENTS

Abstract 1

Chapter 1. Star Formation 2
1. Formation of Low Mass Stars and Massive Stars 3
1.1. A Scenario of Star Formation 2
1.1.1. Low Mass Stars 3
1.1.2. High Mass Stars 4
1.2. Cloud Properties and Star Formation 5
1.3. The Initial Mass Function 6
2. Star Formation of External Galaxies 7
3. Star Burst in the Galaxy 8
4. Massive Star Formation in W49A 9

Chpater 2. Molecular Line Analyses of W49A 15
1. Molecular Line Studies 15
2. Observations with the 45m Telescope 16
3. Results of Molecular Line Studies toward W49A Core 18
3.1. Classification of Molecular Lines 18
3.2. Radial Distributions 23
4. Discussion 23
4.1. Interpretation of Line Profiles 23
4.1.1. The 8 km s^{-1} Dip 25
4.1.2. The 17 km s^{-1} Dip 27
4.1.3. Comparison with Interferometric Line Profiles 28
4.2. Density and Temperature Distribution 28
4.2.1. Density Distribution 28
4.2.2. Temperature Distribution 30
4.3. Collapse of the Durrounding Envelope 31
5. Conclusions 32

Chapter 3. Structure and Kinematics in Massive Core 33
1. Structure around Massive Core 33
2. Observations with the 45m Telescope 33
3. Results of Small Scale Mapping 34
3.1. Results of ^{12}CO Observations 34
3.1.1. Velocity Components of ^{12}CO toward W49A Core 34

3.1.2. Distribution of ^{12}CO around W49A Core 35
3.2. Results of ^{13}CO Observations 37
3.2.1 ^{13}CO Small scale Distribution 37
3.2.2. Velocity Structure 42
3.3. Results of Small Scale $H^{13}CO^+$ Observations 45
4. Discussion 47
4.1. Rotating Necklace and W49A Core 47
4.1.1.. Mass of the W49A core 47
4.1.2. Supporting Mechanism 48
4.2. Collapse of Massive Core 49
4.3. Massive Star Formation in W49A Core 50
5. Conclusions 53

Chapter 4. Dust Emission from W49A 54
1. Dust Emisson and Massive Core 54
2. Submillimeter Continuum Observations 54
3. Results of Submillimeter Continuum Emission 55
3.1. 450 μm and 1,100 μm Distribution 55
3.2. Radial Distribution of 450 μm and 1,100 μm 57
4. Discussion 58
4.1. Morphology of Dust Cloud and Dust Emission 58
4.2. Mass of W49A Deduced from Dust Emission 59
4.3. Dust Properties in Massive Core 60
4.4. Interpretation of the Spectral Index Map 65
5. Conclusions 66

Chapter 5. Inside of Massive Core 67
1. Star Formation and Massive Core 67
2. Observations with NMA 67
2.1. Observations of CS($J = 1 - 0$) Emission 67
2.2. Observations of SiO($J = 2 - 1$) and $H^{13}CO^+$($J = 1 - 0$) Emission 68
2.3. Data Reduction 68
3. Results of Interferometric Observations 75
3.1. Continuum Emission 68
3.2. Molecular Line Emission 69
3.2.1. CS($J = 1 - 0$) Emission 69
3.2.2. SiO($J = 2 - 1$) and $H^{13}CO^+$($J = 1 - 0$) Emission 73

3.3. Shell Structure of Position Velocity Map 74
4. Discussion 74
4.1. Dust Emisson Contributed from the Continuum Emission 74
4.2. SiO Emission Mechanism 79
4.3. Shell Structure of CS Emission and Cloud-Cloud Collision 80
4.4. Infall Gas and Accretion Shock 81
4.5. Star Formation in W49A Massive Core 83
5. Conclusions 84

Chapter 6. Large Scale Distribution 85
1. Large Scale Gas Distribution 85
2. Observations with the 45 m Telescope 85
3. Large Scale ^{13}CO Distribution 86
3.1. Large Scale Distribution of ^{13}CO 86
3.2. Large Scale Distribution of HCO^+ 90
3.3. Large Scale Distribution of HCN 90
3.4. Large Scale Velocity Structure 90
4. Discussion 93
4.1. Massive Star Formation in W49A 93
4.2. Large Scale Star Formation in the Galaxy 95
4.3. Arc Structure and Star Formation in W49S 96
5. Conclusions 98

Chapter 7. Massive Star Formation and Molecular Cloud Cores 100
1. Molecular Line Analysis and Spatial Distribution 100
1.1. Spatial Dsitribution of Gas and Dust 100
1.2. Molecular Line Analysis and Radial Distribution 100
1.2.1. Molecular Line Analysis 100
1.2.2. Radial Distribution of Molecular Lines 105
1.3. Interpretation of Spectra and the Structure of W49A 106
2. The Structure of Massive and Unstable Core 106
2.1. CS Observations 106
2.2. SiO Observations 106
2.3. Cloud-Cloud Collision 108
3. Star Formation in W49A 109
4. Concluding Remarks 111

Appendixes

ABSTRACT

I have observed the W49A molecular cloud complex, which is one of the most luminous star forming regions in our Galaxy, using the 45-m telescope and Nobeyama Millimeter Array of Nobeyama Radio Observatory, and the JCMT 15-m submillimeter telescope. I present high-resolution images of various molecular line emissions.

I explain various molecular line features in terms of coexistence of self-absorption and two velocity components located inside the massive core of W49A. I show evidence that at least two fragmented clouds exist within the W49A core. "Shallow dip line" profiles demonstrate that the dip velocity varies as a result of the relative strength of the blue- and redshifted peaks. We can naturally understand this fact when the two velocity components exist in the W49A cloud core with their corresponding line intensities different from one to the other reflecting the difference in their physical and chemical conditions. In the W49A core, a huge amount of mass, $\sim 10^5$ $M_\odot$ estimated from molecular and dust emissions, is closely packed in a small region, which is collapseing toward its center where the star formation rate suddenly increased 10^4-10^5 *yr* ago.

Interferometric observations revealed internal structure of the massive core with high angular resolution. Images of CS ($J = 1 - 0$) emission show that the 4 km s^{-1} component is surrounded by the 12 km s^{-1} component. A shell structure was seen in the CS map, which structure might be formed by cloud-cloud collision. Thermal SiO emissions show infalling gas which is focusing toward the center of W49A. A simple model of an accreting and rotating massive core was presented with the rotational velocity of 2 ± 1 km s^{-1}/pc and the infall velocity of 5 ± 2 km s^{-1}.

Star formation in W49A might have occured not by a simgle trigger but by two stages of star formation, *i.e.*, formation of the massive dense cores during the collision event and subsequent massive star formation. Cloud-cloud collision might form the massive core, which is contracting to form several fragments. These fragments with strong magnetic field are rotating and collapsing.

Cloud-cloud collision may be a necessary process for massive to make a supercritical cloud, in which massive stars form. Large mass accretion rate of in such a supercritical cloud is also important to form massive stars inside it. Cluster of massive stars are formed by collapse of a massive core, which may be in turn formed by a cloud-cloud collision. This scenario reasonably accounts for localized starburst of massive stars in the Galactic molecular clouds.

Chapter 1

STAR FORMATION

1. FORMATION OF LOW MASS STARS AND MASSIVE STARS

Star formation is one of the major topics of astronomical research in the recent decades, and observations at various wavelengths ranging from radio, infrared, optical, ultraviolet to X rays have revealed new pictures of star forming regions in our Galaxy as well as in external galaxies.

Stars form in dense regions of molecular clouds. Their structure and kinematics are observed through molecular emission lines at radio wavelengths especially in the millimeter region. Emission from dust observed in the millimeter and submillimeter wavelengths reveals the structure of the densest part of molecular clouds. The youngest stars emerge as far infrared sources embedded in molecular clouds, and become visible as T Tauri stars, Herbig Ae/Be stars, or ultracompact H II regions, for low, intermediate, and high mass stars, respectively.

IRAS (Infrared Astronomical Satellite) gave us a great deal of far- to mid-infrared data, and many statistical works on star formation in the Galaxy and external galaxies are being carried out based on them. The *IRAS Point Source Catalog* provides us with important information on the 12, 25, 60, and 100 μm fluxes of young stars embedded in molecular cloud cores.

T Tauri stars and Herbig Ae/Be stars are visible and are observed as highly variable X-ray stars. On the other hand, ultracompact H II regions embedded in dense molecular cloud cores are generally invisible and are observed through infrared emission from hot dust in and peripheries of the H II regions and the free-free radio emission from warm plasma.

Energetic mass outflows are observed in star forming regions with high velocity line emission from molecular, atomic, and ionized gas. Herbig-Haro objects and radio maser lines are observed from shocked clumps in such outflow regions as well as from the interface between the outflows and quiescent gas.

1.1. A Scenario of Star Formation

From the observations at various wavelengths, a scenario of star formation is being unveiled (Shu, Adams, and Lizano 1987; Hayashi *et al.* 1991). As the timescale of protostellar formation and subsequent pre-main sequence evolution is longer in the case of less massive stars, our current view on the star formation is based mainly on observations of low mass stars. In the following, we review observational studies of star formation processes and their difference between low-mass to high-mass cases.

1.1.1. Low Mass Stars

In low mass star forming regions such as Taurus or Ophiucus molecular cloud, we can find a number of dense molecular cloud cores, which are small (D $\sim$ 0.1 pc), dense (3×10^4 cm^{-3}), and cold ($\sim$ 12K) (Myers, Linke, and Benson 1983; Myers and Benson 1983).

High resolution observations of such dense cores show flattened, slowly rotating structures around young stellar objects (e.g., L1551 IRS5; Kaifu *et al.* 1984, Sargent *et al.* 1988; HL-Tau; Hayashi, Ohashi, and Miyama 1993). These outer structures with (r$\sim 10^{3-4}$AU) serve as envelopes for even smaller inner structures (r $\leq 10^2$ AU), which are directly connected to the formation and evolution of the young stellar objects.

When the innermost part of a cloud core becomes gravitationally unstable, the gas and dust begin to infall to form a small protostar (of $\sim 10^{-2}$M$_\odot$). A *protostar* is defined as an object deriving most of its energy from accretion of dynamically infalling material, rather than from either hydrogen (or deuterium) burning or the release of gravitational energy by quasi-hydrostatic contraction as a pre-main-sequence star (PMSS) (Beichman *et al.* 1986). The gas accreting toward the central protostar naturally forms a disk, which grows as the central star gains mass. The envelope is dissipated at a certain stage and the mass supply to the inner protostar/accretion disk system stops.

Beichman *et al.* (1986) investigated the relation among T Tauri stars, young visible stars and molecular cloud cores using the *IRAS Point Source Catalog* data. Half of the newly forming stars are associated with molecular cloud cores, while the other half in the infrared sample has no visible counterparts. The sources with optical counterparts are identified as known T Tauri stars. In unit of free-fall time scale these invisible sources are among the youngest stars yet observed.

Ohashi *et al.* (1991) observed CS ($J = 2 - 1$) line and 98 GHz continuum emission of 11 protostellar *IRAS* sources, five T Tauri stars and six invisible sources, with high angular resolutions. Most of the invisible *IRAS* sources still embedded in dense envelopes detected in CS are not accompanied by massive circumstellar dust disks, while the optically visible sources are not detectable in CS and are accompanied by massive ($M_d \sim 10^{-1}$M$_\odot$) dust disks whose sizes are smaller than $\sim$ 1000 AU. This simultaneous progress of the growth of the inner disk-protostar system and the dispersal of the outer envelope is also demonstrated by the observed anticorrelation between the *IRAS* 12 μm/25 μm color and the C^{18}O column density observed with the 45-m telescope (Hayashi *et al.* 1994). Many of the invisible objects with no optical counterparts are associated with outflowing molecular gas, which is thought to be an indicator of protostars (Myers *et al.* 1987). The outflowing gas are highly collimated as a bipolar flow. It is suggested that the flow disturbs the outer envelope of the cloud and stops the mass supply from the envelope to the inner star-disk system, thereby determining the final mass of the forming star (Nakano, Hasegawa, and Norman 1994).

Structural link may be seen between the outer part of the core and its inner region more closely connected to the accreting disk-star system. For example, the IRAS source 04016+2610 (L1489) is located at the peak of the interferometric CS ($J = 2 - 1$) map (Ohashi *et al.* 1991). The highest resolution CS ($J = 2 - 1$) map shows a strong central peak elongated in the east-west direction with weak extensions toward north and south. Although the strong peak is probably not resolved, the weak extensions toward north and south represents real structures around the *IRAS* source. The weak extended structure in the north-south direction is perpendicular to the alignment of the bipolar outflow (Myers *et al.* 1988) and a velocity gradient of $\sim$2 km s^{-1} was observed along the elongation from north to south (Ohashi *et al.* 1991). This situation is naturally expected when a rotating gaseous disk exists around a protostar. The weak extended emission might correspond to the inner part of a gaseous disk around the protostellar source IRAS 04016+2610. The elongation observed in the larger scale ($\sim$0.4 pc) is aligned with the elongation observed in the small scale ($\sim$0.01 pc) in the case of the L1489 dark cloud, although it is not known whether the same physical mechanism such as the magnetic field has formed both of the observed structures (Miyawaki and Hayashi 1992).

1.1.2. High Mass Stars

In comparison with the case of low mass star formation described above, formation and initial evolution of massive (> 20 M$_\odot$) stars proceed with much shorter timescales. Mass accretion from the outer envelope, evolution of the central star, and disruption of the inner part of molecular cloud cores occur almost simultaneously.

As the effective temperature of the central star becomes high enough, an ionized region begins to be formed around it. It is observed by thermal radio continuum emission. Ultracompact H II regions of diameter D$\lesssim$ 0.1pc, electron densities $> 10^4$ cm^{-3}, and emission measures $\gtrsim 10^7$ pc cm^{-6} are such objects produced by massive stars deeply embedded in molecular clouds. The ultraviolet radiation from stars is absorbed by dust in the H II regions and in the molecular gas surrounding them, and luminous mid- to far-infrared radiation is emitted from the warm dust.

Because massive stars are close to the galactic plane, observations with single dish radio telescopes are often confused by various sources such as extended or compact H II regions with different ages and supernova remnants. Interferometric observations, *e.g.*, with the Very Large Array (VLA), are less sensitive to the large scale structure of extended H II regions, while it can reveal detailed structures of ultracompact H II regions within them. Wood and Churchwell (1989b) observed radio images of a sample of ultracompact H II regions with VLA and made a statistic analysis. They present a morphological classification into five types; spherical or unresolved, cometary, core-haro, shell, and irregular or multiply peaked structures.

Strong H_2O and OH masers associated with ultracompact H II regions are frequently observed. Maser emission are observed also in other molecules in some of these regions; SiO masers (*e.g.*, Ori KL, Sgr B2 MD5, W51A IRS2; Snyder and Buhl 1974; Hasegawa *et al.* 1986; Morita *et al.* 1992), CH_3OH masers (*e.g.*, Sgr B2; Morimoto, Ohishi, and Kanzawa 1985), H_2CO masers (*e.g.*, NGC7538; Forster *et al.* 1980), and NH_3 masers (*e.g.*, W51, NGC7538, W49A, and DR21(OH); Madden *et al.* 1986).

Warm dust reradiates nearly all stellar luminosity in the far-infrared (FIR), and ultracompact H II regions are found as strong *IRAS* point sources. From the *IRAS Point Source Catalog* we can also determine massive star formation rates in molecular clouds. The 60 μm and100 μm emission from H II region complexes is luminous enough so that *IRAS* detected O stars embedded in molecular clouds anywhere in the Galactic disk. Wood and Churchwell (1989a) reported distribution of massive stars in galactic disk and the current rate of massive star formation in the Galaxy.

In some regions, we observe molecular envelopes still accreting to the center. One of such examples is G10.6-0.4. VLA observations of the NH_3 lines suggest that the molecular cloud surrounding the H II region is the original condensation from which the massive stars currently powering the H II region have formed. Part of this molecular cloud undisturbed by the small central H II region is still in a state of gravitational collapse (Ho and Haschick 1986; Ho, Klein, and Hashick 1986; Keto, Ho, and Haschick 1987; Keto and Ho 1988). The velocity field in the molecular cloud core is characterized by differential rotation and accelerating infall (Keto and Ho 1988; Omodaka *et al.* 1992).

1.2. Cloud Properties and Star Formation

It appears that massive stars form only in giant molecular clouds, while formation of less massive stars is found to occur in both giant clouds and smaller dark clouds. Solomon *et al.* (1985) reported that molecular clouds found in their Galactic plane survey are divided into cold and warm ones. Cold clouds ($T_k \lesssim$10 K) do not contain massive stars and seem to be distributed throughout the galactic disk, while warm clouds ($T_k \gtrsim$20 K) are associated with H II regions and distributed in spiral arms. This difference in star-forming activities may reflect the difference in the properties of densest portions of star forming clouds, *i.e.*, molecular cloud cores.

Molecular cloud cores associated with massive star formation have significantly more mass than the cores in dark clouds (*e.g.*, Myers 1985). Answers to the following two important questions should connect this difference: Why are massive cores formed only in giant molecular clouds and why are massive stars formed only in massive cores? We do not have good ideas to answer to the first question. For the second question, we may have caught a theoretical crew for a solution (Nakano, Hasegawa, Norman 1994; see the next section).

1.3. The Initial Mass Function

One of the goals of studies of star formation is to understand the mass spectrum with which stars are formed. Theoretical and observational approaches have been made to understand the initial mass function (IMF) in relation with the places and conditions of star formation.

Salpeter (1955) estimated the IMF from the observations of stellar luminosity function in the solar neighborhood. When we define the IMF as the number of stars formed per unit logarithmic mass interval, it is expressed approximately in a power laws for the stellar mass above one solar mass;

$$\frac{dN}{d\log m} \propto m^{\Gamma}, \tag{1.1.}$$

where m is the stellar mass. The power index Γ estimated by Salpeter (1955) is -1.35, while Scalo (1986) obtained the value of -1.7 $\pm$ 0.5. Actually, observed IMF does not extend indefinitely with the same slope toward smaller and larger masses.

The inferred IMF does not decline monotonically with mass near 1 $M_{\odot}$ but has a second peak just above 1 $M_{\odot}$. This behavior is called as the "bimodality" of IMF (Miller and Scalo 1979 and Scalo 1986). It might mean that there are two modes of star formation, *i.e.*, bimodal star formation, in which the birth of low mass and massive stars involve separate mechanisms as has been suggested by Herbig (1962) and Mezger and Smith (1977).

What is the condition for massive star formation? Nakano, Hasegawa, and Norman (1994) developed a way to relate the mass of a star and the properties of a core in which it forms. They applied the theory to the statistics of the cloud cores in the Orion A giant molecular cloud observed by Tatematsu *et al.* (1993), and found that the estimated IMF is similar to the field star IMF for intermediate and high mass stars (Scalo 1986). However, a question that why massive cores are formed only in warm giant molecular clouds remains to be solved.

What is the condition for massive core formation? Elmegreen and Lada (1977) suggested that star formation occurs quite naturally as an I(ionization)-S(shock) front moves through a cloud. The formed protostellar masses depend on the details of the fragmentation of a cold, postshock (CPS) layer, which is the region between I and S fronts, and on the final stages of gravitational collapse. There are three reasons as follows why star formation between I and S fronts may lead to more massive stars than in the case of fragmenting clouds. First it is the fact that the temperature in CPS gas will be higher than that far ahead of shock due to the heat input by warm, radiating dust in the nearby H II regions. Because the mass of a fragment depends sensitively on its temperature, protostellar masses will be larger in the warm CPS layer than they will be in the distant, cooler parts of the molecular cloud. Secondly the mild Rayleigh-Taylor instability in the CPS layer may increase the protostellar mass by making the gas subsonically turbulent,

thereby increasing the rms velocity of the CPS gas and simulating a large temperature. Third reason is that larger mass in the CPS gas may promote the coalescence of the optically thick fragments. These collisions may be more frequent in a plane-parallel geometry than in a sphere.

From the above reasons, the molecular gas that is accumulated between I and S fronts becomes unstable to gravitational collapse when it reaches a threshold column density, and massive stars form. This scenario of sequential star formation model requires an initial OB star formation possibly triggered by some other mechanisms. For such triggers, cloud-cloud collisions (see section 3), supernova shocks, and density wave shocks have been proposed. The relation between the formation of massive cloud cores and these triggering mechanisms needs to be investigated.

2. STAR FORMATION IN EXTERNAL GALAXIES

A *starburst* can be defined as a star-forming event in a galaxy during which the star formation rate is much higher than normal (*e.g.*, Larson 1987) . Starbursts seen in external galaxies are regions of greatly enhanced star formation rate (SFR), often (but not always) in the central regions of a galaxy. There are a number of evidence that starbursts selectively form massive stars (Rieke *et al.* 1985, 1988; Scalo 1986).

Larson and Tinsley (1978) compared in the UBV two-color diagrams a sample of interacting galaxies with a control sample of isolated galaxies, concluding that tidal force in interacting galaxies triggers burst of star formation. The *IRAS* survey gave us a great deal of information on starburst galaxies. "*IRAS* luminous galaxies," discovered by Soifer *et al.* (1984), lead us to discussion whether they are starburst galaxies or active galactic nuclei (AGN). Observations of their 10 μm fluxes showed that the emission come from the surroundings of massive stars (Joseph and Wright 1985). Moreover it was found from observations of high resolution optical imagings that these "*IRAS* luminous galaxies" are interacting galaxies and starburst activities are concentrated in their centers. These results suggest that "*IRAS* luminous galaxies" are starburst galaxies formed through galaxy-galaxy interaction.

What is the mechanism that links tidal interaction and a starburst? Comparison between the *IRAS* luminosities and molecular gas mass have shown that interacting galaxies exhibit elevated star formation efficiency (SFE), i.e., the yield of massive stars per unit mass of molecular gas, relative to isolated galaxies (Young *et al.* 1986; Sanders *et al.* 1986; Solomon and Sage 1988; Tinney *et al.* 1990).

The luminosity-to-H_2 mass ratio as a function of the central gas surface density ($M_{\odot}pc^{-2}$) for these galaxies show a trend for incleasing luminosity-to-mass ratio with increasing central gas surface densities (Scoville 1991). This means that the high efficiency of energy generation (L_{IR}/M_{H_2}) seen in nuclei of infrared luminous galaxies must be

linked to the high central gas concentration. Conversion of molecular gas into massive stars must be at a greater rate than in normal galaxies (Sanders, Scoville, and Soifer 1990; Scoville 1991). Detailed processes of mass conversion may depend on the concentration of molecular gas, not merely on the total H_2 mass.

Numerical simulations of interaction between galaxies including gas clouds suggest a scenario for the triggering of nuclear burst of star formation (Noguchi 1987;1988). Tidal force to a perturbing galaxy induces a bar structure in the self gravitating stellar disk. Afterward this bar in turn induces an infall of interstellar gas into the nuclear region, forming concentration of molecular clouds in the center of the galaxy. Frequent cloud-cloud collisions may trigger a burst of star formation by the time when bridges and tails develop as observable signs of the galaxy-galaxy encounter. If cloud-cloud collisions cause formation of massive stars, the enhanced cloud-cloud collision rate should result in an increase of massive star formation rate per unit mass of H_2.

5mm

3. LOCALIZED REGIONS OF STAR BURST IN THE GALAXY

If we extend the meaning of *starburst* as a phenomenon that the SFR becomes higher in a certain period of time than in the other period, we can see several regions of localized *starburst* in the Galaxy or in nearby galaxies. Molecular clouds in the Galaxy such as W49A (Miyawaki, Hayashi, and Hasegawa 1986, *hereafter* MHH), W51A (Rengarajan *et al.* 1984; Rudolph *et al.* 1990), and Sgr B2 (Hasegawa *et al.* 1994; Miyawaki *et al.* 1994; Sato *et al.* 1994) are examples which show evidence for such short-lived, extremely active star formation.

MHH argued that star formation in the W49A complex is *a burst of star formation* of OB stars. In the W49A core, a huge amount of mass, $(0.5\text{-}2.5)\times10^5$ $M_\odot$, is closely packed in a small region 3.4 pc in diameter. MHH discussed that the star formation rate in this core region has suddenly increased 10^4-10^5 *yr* ago, and that the massive core should collapse to cease the current star forming activity within 10^5 *yr* unless there is some supporting mechanism. The presence of such a burst-like star formation in the W51A has also been suggested by Rengarajan *et al.* (1984) based on their far-infrared observations.

Sgr B2 is another example of locarized starbursts. Recently Hasegawa *et al.* (1994) found clear evidence of a cloud-cloud collision event in the large scale structure and velocity field of the molecular gas near Sgr B2. In their model, a cloud of $\sim$15 pc in size and 10^6 $M_\odot$ in mass, which was most clearly observed at $V_{LSR}\sim$75 km s^{-1}, is colliding with more extended molecular gas, which was most clearly observed at $V_{LSR}\sim$45 km s^{-1}. The 75 km s^{-1} cloud is moving toward northeast and that cloud is interacting with the 45 km s^{-1} cloud by its side, making a large velocity shear at the interface, where aligned H II regions are found. Formation of massive stars were most probably triggered in the highly turbulent and shocked interface, although the detailed process of the trigger remains unclear.

Detailed studies of the regions such as W49A, W51A, and Sgr B2 can significantly contribute to the understanding of starburst mechanisms because these localized regions have similar characteristics in common with starburst penomena, which were observed in many starburst galaxies in the present epoch and are supposed to be a key process in the era of galaxy formation.

Spatial scales of the burst of star formation in these local regions are, however, extremely smaller than that in starburst galaxies. Size of star forming regions in starburst galaxies *e.g.*, M82, Arp 220 (500-1000 pc; Wynn-Williams 1987) is much larger than the size of W49A. Luminosities of starburst galaxies ($3\times10^9 - 3\times10^{10}$ $L_\odot$) and the decay time of their star formation rate ($\sim 10^9$ *yr*) are extremely larger than those of W49A ($\sim 10^7$ $L_\odot$ and 10^5 *yr*, respectively; MHH). However, hundreds of star forming regions like W49A are formed at the same time in the Galaxy with their duration time scale of 10^9 *yr*, our Galaxy would appear as a starburst galaxy. Investigation of such localized regions of starburst in the Galaxy can lead us to understand the microscopic process of starbursts.

Localized starburst regions are found also in nearby galaxies. In particular, 30 Doradus, an enormous H II region with no equivalent in our Galaxy, in the Large Magelanic Cloud is an extensive massive star formation region. Similar starburst regions are seen in M33 H II regions and 3 to 20 times more luminous H II regions than those in M33 are found in NGC 5471 and M101.

5mm

4. MASSIVE STAR FORMATION IN W49A

A large number of research works have been made on the W49A molecular cloud complex. Each of them deals with the H II regions, the molecular cloud, or both. The radio continuum source of W49 was catalogued by Westerhout (1958) in his pioneering galactic survey. It consists of two radio sources, W49A (G43.2+0.0) and W49B (G43.3–0.2). The separation of the two is 12′. W49A has a radio spectrum of thermal plasma, while W49B is a supernova remnant exhibiting a nonthermal spectrum (Mezger, Scraml, and Terzian 1967). Those two sources are not associated with each other. The distances of W49A and W49B have been determined from HI absorption line measurements by Akabane and Kerr (1965), Sato, Akabane, and Kerr (1967) and Sato (1968). The LSR velocity of W49A is $\sim$12 km s^{-1} and that of W49B is $\sim$63 km s^{-1}(Kazes, and Nguyen-Quang-Rieu 1970). These velocities correspond to different spiral arm components.

W49A is a complex of ultracompact H II regions and massive molecular cloud cores. It is the most luminous star forming regions in our Galaxy. Interferometric observations have resolved the structure of W49A into W49(a) and W49(b) (Wynn-Williams 1969; Schraml

and Mezger 1969). Among them the compact H II region C, denoted by Wink, Altenhoff, and Webster (1975), is the brightest at frequencies higher than 5 GHz and appears to be the site of the most recent star formation (Wink, Altenhoff, and Webster 1975; Dieter, Welch, and Wright 1979). VLA observations of this component have resolved it into a cluster of ultracompact H II regions excited by several O4-O9 stars (ZAMS) (Dreher *et al.* 1984). Observations of hydrogen recombination lines revealed a velocity gradient in the cluster of ultracompact H II regions, which lead Welch *et al.* (1987) to describe the cluster as a rotating necklace of 2 pc in diameter (Figure 1-1). Dreher *et al.* (1984) further resolved the component C denoted by Wink, Altenhoff, and Webster (1975) and named the newly resolved components as A to G. In this paper we mainly use the notation by Wink, Altenhoff, and Webster (1975) and show them in capital letters such as the component C. When we use notations of Dreher *et al.* (1984), we use small characters, *e.g.*, the component g in W49N.

W49A contains the most luminous H_2O maser source in the Galaxy (Raimond and Eliason 1969; Walker, Matsakis, and Garcia-Barreto 1982; Johnston and Hansen 1982; Genzel, and Downes 1977). Two clusters of H_2O and OH masers are found to be associated with the two radio continuum peaks W49(a) (or component B-G) and W49(b) (or component L and K), respectively. These maser sources are called W49N and W49S, respectively, and are separate 2.'5 away from wach other (Downes and Wilson 1974).

The strongest H_2O and OH maser sources are associated with the compact H II region component C (Walker *et al.* 1977; Walker, Matsakis, and Garcia-Barreto 1982; Kent and Mutel 1982; Johnston and Hansen 1982). From higher resolution data, Dreher *et al.* (1984) reported that these H_2O masers are associated with one of the ultracompact H II regions in the "necklace". High-resolution observations at 8 μm and 20 μm have shown that the 5-20 μm source is associated with the masers within $\pm 1''$ (Genzel and Downes 1982). The H_2O maser has the luminosity of $\sim 1\ L_\odot$ if the maser emission is isotropic. It is 10^4 times more luminous than the Orion KL masers (Genzel and Downes 1977). It shows very high-velocity maser features over more than 500 km s^{-1} (*e.g.*, Morris 1976), which indicates the vigorous kinematic motion of molecular gas associated with the star formation. The H_2O masers of W49S are also active with their total luminosity 300 times larger than that of Orion KL (Genzel and Downes 1977).

W49A is also a complex of far infrared sources. They positionally coincides with the compact H II region component C in W49N. Two 20 μm infrared sources were first reported by Becklin, Neugebuer, and Wynn-Williams (1973). The 53 μm map by Harvey, Campbell, and Hoffmann (1977) showed several condensations of warm dust corresponding to the compact H II regions around W49A. The total infrared luminosity from the area 2′ in diameter centered on W49N is $6 \times 10^6\ L_\odot$ (Harvey, Campbell, and Hoffmann 1977); this is the most luminous object in our Galaxy. Another far infrared cluster is denoted as

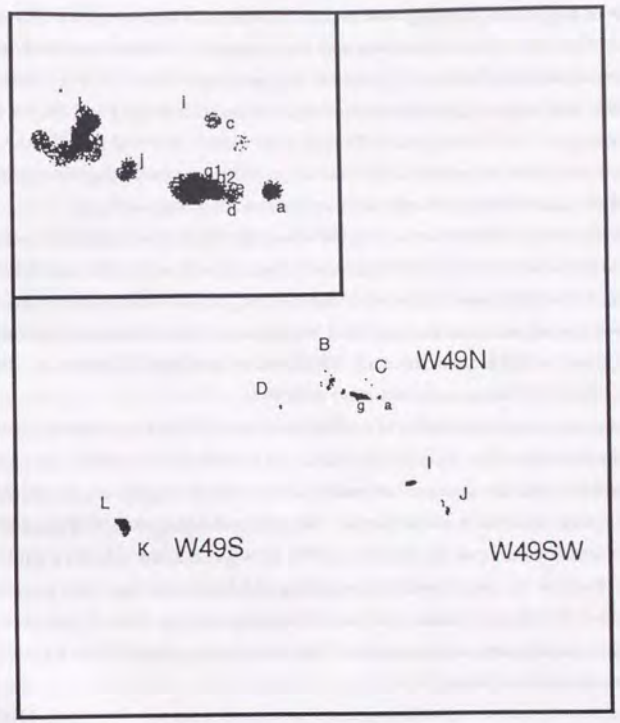

Figure 1-1: Schematic Continuum Images of W49A. Schematic images of the core of W49A traced on the VLA image at 6 cm wavelength (Welch *et al.* 1987), which show emission from ionized gas surrounding one or more hot massive stars. There are three clusters; W49N, which is the most active region in W49A including H_2O and OH masers, W49S, which consist of a single O4 star and also include H_2O and OH masers, and W49SW. These clusters are associated with hot gas and dust emission. Upper left corner panel present close up image of W49N. Capital characters are denoted by Wink, Altenhoff, and Webster (1975) and small characters are denoted by Dreher *et al.* (1984).

W49SW (Harvey, Campbell, and Hoffmann 1977), which is associated with the component I and J. These correspond to compact H II regions and are warm dust surrounding them.

The giant molecular cloud associated with the W49A complex was first observed by Scoville and Solomon (1973). In spite of this early identification, there are a very limited number of single dish mapping observations of molecular emission lines. One of them is a map of ^{12}CO ($J = 1 - 0$) emission with a resolution of 1′ by Mufson and Liszt (1977). They found two giant molecular clouds at V_{LSR}= 4 km s^{-1} and 12 km s^{-1} both centered on W49A, and suggested that the interaction of the two clouds triggered the star formation in this complex. On the other hand, Phillips *et al.* (1981) observed the ^{12}CO ($J = 2 - 1$) emission along two strips with a 26″ resolution. They suggested that the double-peaked profiles are caused by the absorption by optically thick foreground gas.

Interferometric observations of H_2CO absorption have been made (Goss and Tilanus 1985, Martin-Pintado *et al.* 1985a), which covered both of W49N and W49S. Dickel and Goss (1990) presented higher resolution (∼1–2″) H_2CO observations using VLA and discussed the structure and kinematics of W49N. Recent interferometric millimeter wave observations at OVRO (Scoville *et al.* 1986) and at Hat Creek (Welch *et al.* 1987) have revealed details of the complex structure of W49A.

The structure and kinematics of the W49A molecular cloud core remain controversial. The identification of the dip at V_{LSR}= 8 km s^{-1} by Phillips *et al.* (1981) does not rule out the possibility that the intrinsic lineprofile without the absorption is still double-peaked. This is indeed what MHH and Miyawaki, Hayashi, and Hasegawa (1990) argued based on their observations of optically thin lines; C^{34}S ($J = 1 - 0$) line exhibits a double peaked profile. There is no doubt about the exsistence of a foreground gas, which is possibly an envelope of W49A, that makes a self-absorption dip at V_{LSR}= 8 km s^{-1} in optically thick lines. It is the structure and kinematics of the core inside or behind this 8 km s^{-1} gas that has been the issue of debate.

Based on the observed double-peaked profiles of optically thin lines, MHH argued that there are two cloud components inside the massive core of W49A. They speculated that burst of star formation occured in a massive unstable core formed by a cloud-cloud collision.

This idea was opposed by Welch *et al.* (1987) who argued that W49A is a single massive core undergoing dynamical collapse. In their model, the central region of the collapsing cloud fragmented into a rotating ring of dense cores, and the cores formed massive stars now observed as a "necklace" of ultracompact H II regions. Jaffe, Harris, and Genzel (1987) reported that the submillimeter ^{12}CO($J = 7 - 6$) line toward W49A do not possess sharp central reversal that is clearly seen in the $J = 1 - 0$ and $J = 2 - 1$ lines (Mufson and Liszt 1977; Phillips *et al.* 1981; MHH). They proposed that the core has only one velocity component with extremely large velocity dispersion of 14 km s^{-1}

and the dip at 8 km s^{-1} is only due to self-absorption of foreground cold gas. Recently Dickel *et al.* (1994) present interpretation of the two velocity peaks by radiative transfer of inside-out collapse model.

However, both the colliding cloud model and the collapsing single cloud model lack clear and decisive observational evidence. One of the difficulties is the presence of the absorbing envelope. Another difficulty comes from the bright continuum emssion, which distort the map of the millimeter emission lines. To sort out the problems, we need observations of lines with various optical depths, especially of optically thin lines, at high spatial resolution.

In this thesis, I present new observations of W49A in millimeter wave molecular lines having various optical depths and excitation conditions. The observations were made using the 45 m telescope and five element Nobeyama Millimeter Array (NMA), with high resolution. I also report submillimeter continuum observations with high resolution using James Clark Maxwell Telescope (JCMT). In the next chapter, I present that spectra of W49A have dips due to the presence of both two velocity components and self-absorption. Radial distributions of various molecules are fiitted by power laws. Density and temperature distribution will be discussed. In Chapter 3, maps of ^{12}CO, ^{13}CO, HCO$^+$, H^{13}CO$^+$, and HCN around W49N will be presented. Mass of the massive core is estmated and its structure and kinematics will be discussed. I will present submillimeter continuum maps at 450 μm and 1100 μm and discuss the relation between gas and dust in Chapter 4. In Chapter 5, I will present high angular resolution maps of C^{32}S ($J = 1 - 0$), SiO ($J = 2 - 1$) and H^{13}CO$^+$ ($J = 1 - 0$) obtained with NMA, and discuss the structure in the massive core including the "necklace." Larger scale mapping observations of ^{13}CO, HCO$^+$, and HCN line emissions will be presented in Chapter 6, where I discuss star formation of W49A in larger scales. In chapter 7, I will discuss the structure, kinematics, and massive star formation of the W49A core including the entire W49N and W49S as a summary.

Chapter 2

MOLECULAR LINE ANALYSES OF W49A

1. MOLECULAR LINES AND MOLECULAR CLOUD

The giant molecular cloud associated with W49A was first identified by Scoville and Solomon (1973). The first mapping result by Mufson and Liszt (1977) with ^{12}CO ($J = 1 - 0$) revealed two velocity components at V_{LSR}= 4 km s^{-1} and 12 km s^{-1}, implying the presence of two corresponding giant molecular clouds both centered on W49A. They accordingly suggested the interaction of the two clouds that might have triggered the active star formation in this complex. Phillips *et al.* (1981) then observed it in the ^{12}CO ($J = 2 - 1$) emission along two strips with the 26″ resolution, and claimed that the apparent two velocity components were produced merely by the self-reversal at V_{LSR}= 8 km s^{-1} due to absorption by foreground gas.

Detailed observational studies have been made in various molecular lines since then (Goss and Tilanus 1985; Martin-Pintado *et al.* 1985a; Dickel and Goss 1990; Scoville *et al.* 1986; MHH; Welch *et al.* 1987), yet the basic structure and kinematics of the W49A complex are still under discussion. MHH presented a detailed study of W49A in the CS ($J = 1 - 0$) emission at an angular resolution of 34″. They found that even the optically thin C^{34}S line shows two velocity components with different spatial distribution noticeable in its main isotope, supporting the two cloud interpretation by Mufson and Liszt although CO does show self-reversal due to the foreground gas absorption. Welch *et al.* (1987) proposed, on the other hand, from their interferometric HCO$^+$ observations that the massive molecular envelope is freely infalling toward the "necklace" at the center.

The above two interpretations, two clouds and infall, about the kinematical structure of the W49A molecular cloud complex are often taken as two contradicting interpretations with each other. These two interpretations are, however, not necessarily exclusive each other, and there are increasing number of evidence that supports that both occur in W49A. As many theoretical calculations have already shown, we naturally expect the presence of rotating cloudlets at the center of an infalling molecular cloud and that collisions of cloudlets eventually trigger gravitational instability to produce massive stars.

Studies of the W49A molecular cloud complex are difficult not only because it is compact as a result of its large distance but because different molecular lines exhibit different shapes of line profiles. For example some sets of molecular lines show a sharp and deep dip at V_{LSR}~8 km s^{-1} while another show only a shallow dip. Other molecular lines, such as ^{12}CO($J = 7 - 6$) (Jaffe, Harris, and Genzel 1987), even have a single peak at V_{LSR}~8 km s^{-1}. Considering these varieties of molecular line profiles with only a small number of them having been used for observations of W49A, we may have been observing

only a limited portion of the complicated structure and kinematics of the W49A molecular cloud complex. It is hence worth analyzing line profiles of various molecular lines in detail.

In this paper I report observations of W49A with various molecular lines and analyze their radial distribution. I will discuss density and temperature distribution of the W49A massive molecular cloud core.

2. OBSERVATIONS WITH THE 45 M TELESCOPE

Observations were made on 1987 and 1989 using the 45 m telescope of the Nobeyama Radio Observatory (NRO). The telescope parameters and observed lines are listed in Table 2-1 and Table 2-2, respectively. I used the following three single-sideband receivers. The receiver MIL100 had a frequency coverage from 85 to 115 GHz with an instantaneous bandwidth of 500 MHz. The receiver AIL80 covered from 70 to 90 GHz with an instantaneous bandwidth of 2 GHz. I used it to observe molecular lines at the 80 GHz band simultaneously with the MIL100 receiver for 110 GHz lines. The receiver AIL40 covered from 36 to 49 GHz with an instantaneous bandwidth of 2 GHz. I used it for the $C^{34}S$ ($J = 1 - 0$),SiO ($v = 0$; $v = 1$; $v = 2$; $J = 1 - 0$) and H51α observations as well as for pointing calibration. The receiver SIS40 had a coverage from 33 to 49 GHz.

TABLE 2-1

Receivers, and Apeature and Beam Efficencies

Receiver(year)	Frequency [GHz]	Apeature Efficiency [%]	Beam Efficeicy [%]	HPBW [arcsec]	Tsys [K] (SSB)
MIL100(1986)	115	0.25	0.3	15±1	400-600
MIL100(1987-89)	115	0.26±0.03	0.45±0.05	17±1	400-600
MIL100(1987)	86	0.31±0.03	0.48±0.05	21±1	400-600
MIL100(1988-89)	86	0.40±0.03	0.58±0.05	21±1	400-600
AIL80(1987-89)	86	0.37±0.03	0.68±0.05	24±1	600-900
AIL40(1987-88)	43	0.57±0.03	0.75±0.05	39±1	500-900
SIS40(1989)	43	0.48	0.67±0.05	40±1	400-500

TABLE 2-2

Observed Lines and HPBWs

Line	Transition	Frequency [MHz]
^{12}CO	$J = 1 - 0$	115,271.204
^{13}CO	$J = 1 - 0$	110,201.353
$C^{18}O$	$J = 1 - 0$	109,782.182
HCO^+	$J = 1 - 0$	89,188.523
$H^{13}CO^+$	$J = 1 - 0$	86,754.294
HCN	$J = 1 - 0; F = 1 - 1$	88,630.416
HCN	$J = 1 - 0; F = 2 - 1$	88,631.847
HCN	$J = 1 - 0; F = 0 - 1$	88,633.936
$H^{13}CN$	$J = 1 - 0; F = 1 - 1$	86,338.767
$H^{13}CN$	$J = 1 - 0; F = 2 - 1$	86,340.184
$H^{13}CN$	$J = 1 - 0; F = 0 - 1$	86,342.274
$HC^{15}N$	$J = 1 - 0$	86,054.961
SiO	$v = 0; J = 2 - 1$	86,846.998
SiO	$v = 0; J = 1 - 0$	43,423.858
SO	$J = 2_1 - 1_1$	86,093.550
SO_2	$J = 8_{3,5} - 9_{2,8}$	86,639.108
SO_2	$J = 18_{4,14} - 17_{5,3}$	109,757.577
SO_2	$J = 21_{2,20} - 20_{3,17}$	48,120.440
HNCO	$J = 5_{0,5} - 4_{0,4}$	109,905.753
$C^{34}S$	$J = 2 - 1$	96,412.982
$C^{34}S$	$J = 1 - 0$	48,206.956
H51α		48,153.664

The spectral data were taken with 16 banks of acousto-optical spectrometers (AOS) with 32,000 channels in total. Eight of them were high-resolution AOS with a frequency coverage of 40 MHz each and a resolution of 37 kHz, which corresponds to the velocity resolution of 0.10–0.13 km s^{-1} at 86–110 GHz and 0.23 km s^{-1} at 48 GHz. The other eight banks were wide-band AOS with a frequency coverage of 250 MHz each and a resolution of 250 kHz, which corresponds to the velocity resolution of 0.68–0.87 km s^{-1} at 86–110 GHz and 1.56 km s^{-1} at 48 GHz.

The pointing of the antenna was carefully checked during the observations by monitoring the SiO maser emission ($v=1$; $J = 1 - 0$) from R Aql at α(1950)

=$19^h03^m57^s.68$, δ(1950) = 8°09′7″.7 about every 2 hours. The change in antenna pointing was within 5″ in most cases. I did not use the data when subsequent pointing varied more than 10 ″ under strong wind conditions.

All the data were taken under the position switching mode with the OFF position +17′ away in declination. Calibration was achieved by the standard chopper wheel method. The intensity scale is the antenna temperature, T_A^* corrected for atmospheric and ohmic losses (Ulich and Haas 1976). The spectra at the reference center was observed recurrently so that the variation of antenna gain was checked.

I use the distance of 11.7 kpc to W49A throughout this paper. This is the corrected value of the originally measured distance of 13.8 kpc (Akabane and Kerr 1967; Reifenstein *et al.* 1970) according to the revised distance to the Galactic center of 8.5 kpc (Kerr and Lynden-Bell 1986). The corrected distance is consistent with the newly measured value of 11.4±1.2 kpc that Gwinn *et al.* (1992) determined through proper motion measurements of H_2O maser emissions.

The reference center for all the observations was taken to be α(1950) =$19^h07^m49^s.8$, δ(1950) = 9°01′15″.5, which is the position of the component *g* of the thermal continuum emission observed by Dreher *et al.* (1984). The strongest infrared sources (Becklin, Neugebouer, and Wynn-Williams 1973; Genzel and Downes 1982), H_2O/OH masers (*e.g.*, Walker *et al.* 1977), and the component C of the compact H II regions are located within the beam size of the center position. Cross scan observations were made for the lines listed in Table 2-2 with a grid spacing of 15″ in both right ascension and declination. Four other positions, (+15″, +15″), (+15″, -15″), (-15″, +15″), and (-15″, -15″) with respect to the reference center, were also observed for most of these lines.

3. RESULTS OF MOLECULAR LINE ANALYSES OF W49A

3.1. Classification of Molecular Lines

We first examine each observed molecular line profile toward W49A in detail here. Figure 2-1a–d show line profiles of various molecular species and transitions obtained toward the reference center position.

The top panel of Figure 2-1a shows the line profile of ^{12}CO ($J = 1 - 0$), which has prominent double peaks at V_{LSR}∼2 and ∼10 km s^{-1}with a deep dip between them at V_{LSR}∼7 km s^{-1}. It also exhibits a secondary dip at V_{LSR}∼17 km s^{-1} with broad line wing emissions in both red- and blueshifted velocities corresponding to molecular outflows (Welch *et al.* 1987); the total velocity coverage is from −20 to 35 km s^{-1}. The weak emission feature seen around V_{LSR}∼39 km s^{-1} has been attributed to the nearside Sagittarius arm, and has no relation to W49A (Nyman and Miller 1989). The mid and bottom panels of Figure 2-1a show line profiles of HCO$^+$ ($J = 1 - 0$) and HCN

($J = 1 - 0$). These lines share common feature with the ^{12}CO ($J = 1 - 0$) line except that the intensities are weaker. The 39 km s^{-1} feature is observed in absorption for HCO$^+$ (Miyawaki, Hasegawa, and Hayashi 1988).

Figure 2-1b shows the line profiles of ^{13}CO ($J = 1 - 0$), C^{18}O ($J = 1 - 0$), H^{13}CO$^+$ ($J = 1 - 0$). The ^{13}CO and C^{18}O profiles are similar to each other; they have two peaks at V_{LSR}∼4 and 11 km s^{-1} with almost equal intensities. A shallow dip is seen between the two peaks at V_{LSR}∼9 km s^{-1}. The ^{13}CO intensity is stronger than the C^{18}O by a factor of 5, which is close to the ordinary abundance ratio of these two isotopes, suggesting that both these lines are optically thin. The HCO$^+$ profile at the bottom also has peaks at V_{LSR}∼4 and 11 km s^{-1} with a shallow dip at V_{LSR}∼9 km s^{-1}. The blueshifted peak is stronger than the redshifted peak in this case.

The line profiles of C^{34}S ($J = 2 - 1$) and C^{34}S ($J = 1 - 0$) are presented in Figure 2-1c. The ^{13}CO ($J = 2 - 1$) has double peaks at V_{LSR}∼4 and 11 km s^{-1} with a shallow dip at ∼9 km s^{-1}. It resembles the line profiles of ^{13}CO ($J = 1 - 0$), C^{18}O ($J = 1 - 0$), H^{13}CO$^+$ ($J = 1 - 0$), although its redshifted peak is significantly stronger than the blueshifted peak. The C^{34}S ($J = 1 - 0$) line shows a single peak at V_{LSR}∼11 km s^{-1} with an indication of a secondary feature at ∼4 km s^{-1}. Considering from the ^{13}CO ($J = 2 - 1$) case, we may conclude that C^{34}S ($J = 1 - 0$) also has a double peak characteristic with its blueshifted peak much weaker than the red one, so that the blueshifted peak was not clearly identified. The main isotope of CS ($J = 1 - 0$) also shows the similar line profile to ^{13}CO ($J = 2 - 1$) (MHH).

I show the line profiles of SiO SO, and SO_2 in Figure 2-1d. SiO and SO have a single peak at ∼ 6 km s^{-1}. The SO profile would show an indication of double peaks at V_{LSR}= 5.0 km s^{-1} and 7 km s^{-1}. However I do not believe it significant because the dip depth is smaller than the noise level. SO_2 also shows a single peak, while its velocity V_{LSR}= 3.3 km s^{-1}is different from those of the SiO and SO lines. Because other transitions of SO_2 have double peaks (Serabyn et al 1993), we regard SO_2 as a similar case to CS ($J = 1 - 0$) rather than as a simple single peak case.

From the above consideration, we notice that there are generally three types in line shapes: spectra showing double peaks with deep dips inbetween, spectra with shallow dips, and spectra with single peaks. we tentatively call them as "deep dip lines", "shallow dip lines," and "single peak lines," respectively. ^{12}CO ($J = 1 - 0$), HCO$^+$ ($J = 1 - 0$), and HCN ($J = 1 - 0$) are classified into deep dip lines. ^{13}CO ($J = 1 - 0$), C^{18}O ($J = 1 - 0$), HCO$^+$ ($J = 1 - 0$), and C^{34}S ($J = 2 - 1$) are shallow dip lines. We also classify C^{34}S ($J = 1 - 0$) and SO_2 into the shallow dip lines because they can be regarded as a shallow dip case with much weaker blueshifted peaks. C^{32}S($J = 2 - 1$) (Nyman 1984) and HNC (Nyman and Miller 1989) are also classified into this type. SiO and SO are single peak lines. Tbale 2-3 summarizes the parameters for these lines.

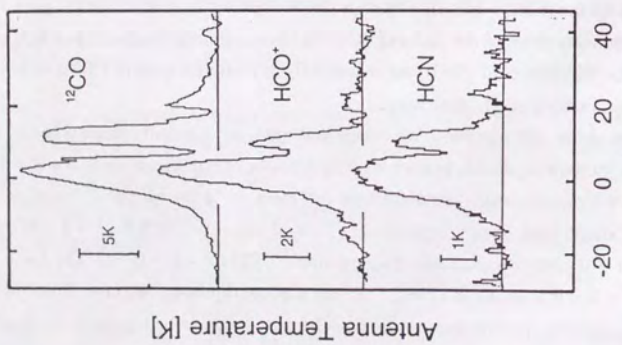

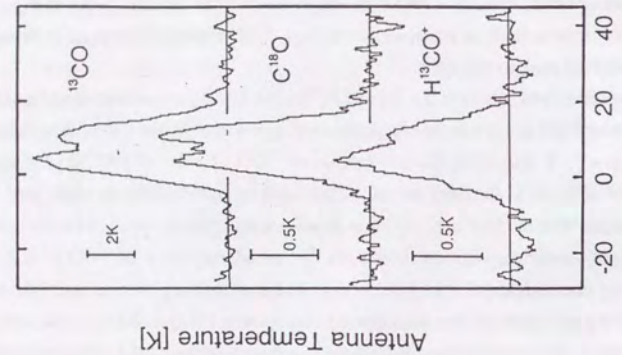

Figure 2-1a-b: Spectra of "deep dip line", "shallow dip line", and "single peak line". (left) (a) ^{12}CO, HCO$^+$, and HCN with deep dip at the LSR velocity of 8 km s^{-1} due to self-absorption, (right) (b) ^{13}CO, C^{18}O, and H^{13}CO$^+$spectra with shallow dip.

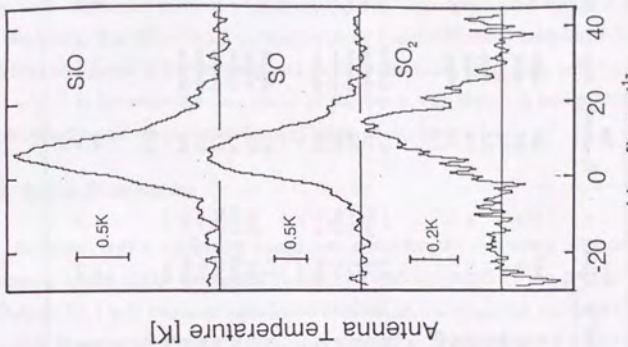

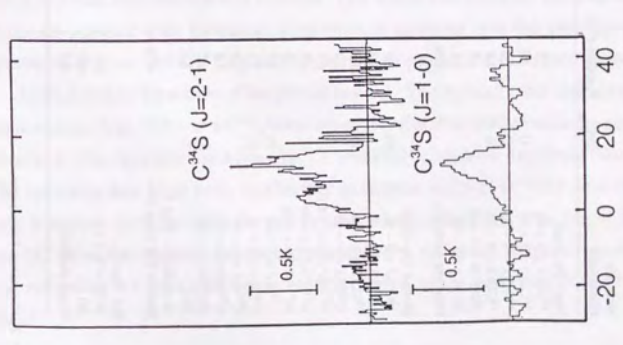

Figure 2-1c-d:(left) (c) C^{34}S(J = 1 – 0 and J = 2 – 1) lines. (right) (d) (c) hot core line, SiO, SO, and SO$_2$spectra.

TABLE 2-3

Deep Dip Lines, Shallow Dip Lines, and Hot Core Lines

Molecule (Transition)	Ref	Peak 1			Peak 2			Dip		
		V_{LSR}[km s^{-1}]	T_A^*[K]	τ	V_{LSR}[km s^{-1}]	T_A^*[K]	τ	V_{LSR}[kms]	shape	Power
Deep Dip Lines										
^{12}CO(J = 1 – 0)		2.3	17.0	–	11.7	15.0	–	6.3	sharp	–
^{12}CO(J = 1 – 0)	1)	3.2	24	–	12.3	24	–	8.0	sharp	–
^{12}CO(J = 1 – 0)	2)	2.0	13.9	–	10.3	16.4	–	7.1	sharp	–
^{12}CO(J = 2 – 1)	3)	3.2	32	–	11.6	41		7.5	sharp	–
HCO$^+$(J = 1 – 0)		1.7	8.2	15	9.4	4.3	21	6.6	sharp	-1.00
HCN(J = 1 – 0)		2.1	4.2	19	10.3	3.1	–	7.3	sharp	-0.80
Deep Dip Lines Av.		2.42			10.93			7.13		
Shallow Dip Lines										
^{12}CO(J = 9 – 8)	4)	3.0	5.0	–	12.4	5.2	–	6.9	shallow	–
^{13}CO(J = 1 – 0)		4.5	8.0	0.1	10.5	7.2	0.34	7.5	shallow	-0.91
^{13}CO(J = 1 – 0)	2)	3.3	3.4	–	11.6	4.5	–	7.6	shallow	–
C^{18}O(J = 1 – 0)		3.9	1.4	0.02	10.7	1.5	0.06	7.9	shallow	-0.88
H^{13}CO$^+$(J = 1 – 0)		4.3	1.3	0.17	10.9	0.9	0.23	8.8	shallow	-1.52
H^{13}CN(J = 1 – 0)		4.5	0.8	0.21	–	–	–	–	–	-1.16
HC^{15}N(J = 1 – 0)		~4	0.3	–	–	–	–	–	–	-0.73
C^{32}S(J = 1 – 0)	5)	4.9	2.8	1.14	11.8	3.7		8.1	shallow	–
C^{32}S(J = 2 – 1)	6)	5.1	4.5*	6.15	11.7	5.2*	9.01	8.2	shallow	–
C^{34}S(J = 1 – 0)		3.9	0.14	0.05	13.0	0.52	0.15	6.5	shallow	-0.56
C^{34}S(J = 2 – 1)		3.9	0.53	0.27	14.0	0.80	0.40	8.2	shallow	-0.99
$C_2H(N = 1 – 0)$	6)	6.2	0.8*	–	13.8	1.3*	–	8.9	shallow	–
HNC	7)	5.0	3.2*	–	11.5	2.7*	–	8.4	shallow	–
SO($18_{14} – 17_{13}$)		–	–	–	13.2	0.4	–	–	–	-1.65
Shallow Dip Lines Av.		4.35			12.09			8.10		
Hot Core										
SiO(v = 0; J = 2 – 1)		6.2	2.0	–	–	–	–	–	– –	-1.81
SO		6.0	2.2	–	7.0	2.2	–	–	– –	-2.25
Single peak Av.		6.1			7.0			–		

*: T_B:Brightness Temperature

Reference: 1) Mufson and Liszt 1977; 2) Langer and Penzias 1990; 3)Phillips *et al.* 1980; 4) Boreiko and Betz 1991; 5) Miyawaki *et al.* 1986; 6) Nyman 1984; 7) Nyman and Millar 1989

The deep dip lines are optically thick, so that one may as well consider that the dips at V_{LSR}~7 km s^{-1} are due to self-absorption by cold foreground gas. The present situation is, however, not so straightforward because optically thin shallow dip lines also have dips at the similar velocity. We discussed about this in the previous paper (MHH) and will give more detailed discussion in section 4.1 on the basis of presently availbale data.

Thermal emissions of SiO and SO have so far been detected in highly excited regions such as in the Orion hot core or in interacting regions of molecular clouds with outflows (Downes *et al.* 1982; Wright *et al.* 1983). There is an increasing number of evidence that such molecules come out from dust grains when grains are exposed to shocks. It is interesting that these shock indicators show much different characteristics in their line profiles compared to the deep dip and shallow dip lines; their peak velocities are ~6 km s^{-1} which is between the two peaks of the lines with dips. A comprehensive idea of understanding all these molecules will be given in section 4.1.

3.2. Radial Distributions

Because W49A molecular cloud has considerable symmetry with respect to the mapping center under the spatial resolutions and coverages of the present observations (Chapter 3), I will examine radial distributions of the observed molecules by assuming circular symmetry. Figure 2-2a shows the radial distributions of ^{13}CO ($J = 1 - 0$), C^{18}O ($J = 1 - 0$), HCO$^+$ ($J = 1 - 0$), H^{13}CO$^+$ ($J = 1 - 0$), HCN ($J = 1 - 0$), H^{13}CN ($J = 1 - 0$), HC^{15}N ($J = 1 - 0$), C^{34}S ($J = 2 - 1$), C^{34}S ($J = 1 - 0$), H51α, SiO ($v = 0$, $J = 2 - 1$), SO ($J = 2_1 - 1_1$), SO$_2$ ($J = 8_{3,5} - 9_{2,8}$), and SO$_2$ ($J = 18_{4,14} - 17_{5,3}$). Radially averaged integrated intensities, with arrows for their dispersions, are plotted against the radial distance from the reference center. The intensities decrease monotonically from the center to outward with moderate dispersion, suggesting that the assumption of circular symmetry was not so bad. This enables to make a power law fit to each radial distribution.

Table 2-2 lists the results of the power law fits. The optically thin lines with thermalized excitation such as ^{13}CO, and C^{18}O have relatively flat distribution with the power law index close to 1. The optically thick lines HCO$^+$ and HCN also show the similar flat radial profile. The optically thin lines with subthermal excitation such as H^{13}CO$^+$ and H^{13}CN tend to have a steeper decrease with the power law index close to 1.5. The single peak lines SiO and SO show the steepest decrease comparable to the beam shape, suggesting that these line emissions are localized to a compact region at the center of the W49A molecular cloud.

4. DISCUSSION

4.1. Interpretation of Line Profiles

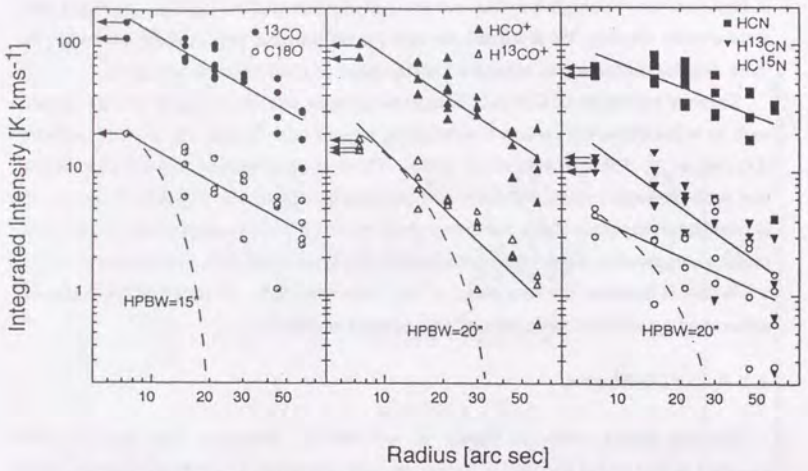

Figure 2-2a: Radial Distribution of the Integrated Intensity. ^{13}CO ($J = 1 - 0$), $C^{18}O$ ($J = 1 - 0$), HCO^+ ($J = 1 - 0$), $H^{13}CO^+$ ($J = 1 - 0$), HCN ($J = 1 - 0$), $H^{13}CN$ ($J = 1 - 0$), $HC^{15}N$ ($J = 1 - 0$). Radially averaged integrated intensities, with arrows for their dispersions, are plotted against the radial distance from the reference center.

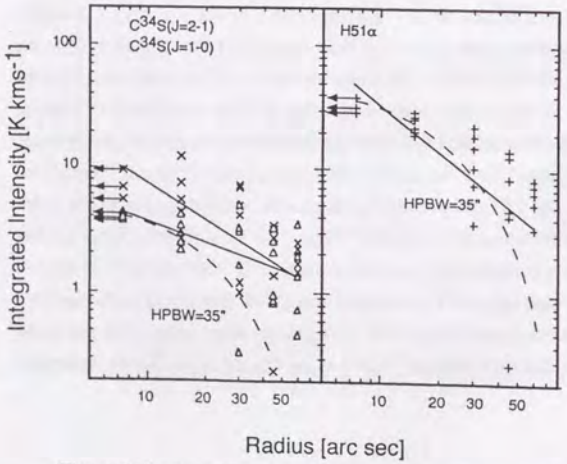

Figure 2-2b: Radial Distribution of the Integrated Intensity. $C^{34}S$ ($J = 2 - 1$), $C^{34}S$ ($J = 1 - 0$), H51α.

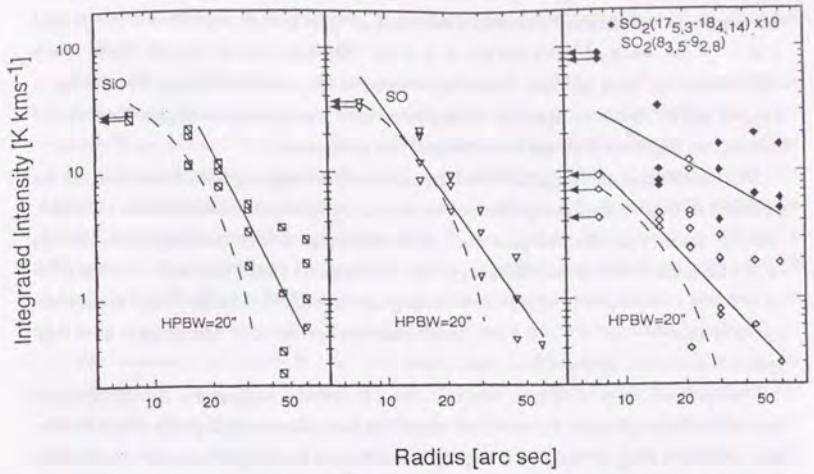

Figure 2-2c: Radial Distribution of the Integrated Intensity. SiO ($v = 0$, $J = 2 - 1$), SO ($J = 2_1 - 1_1$), SO_2 ($J = 8_{3,5} - 9_{2,8}$), and SO_2 ($J = 18_{4,14} - 17_{5,3}$).

4.1.1. The 8 km s^{-1} Dip

There have been much discussion about the true nature of the 8 km s^{-1} dip observed in molecular lines toward W49A. Unfortunately most of the previous studies gave interpretations of the 8 km s^{-1} dip only to explain their own observed line profiles, according to which the discussions were concentrated on too simple arguments such as whether the dip was due to self-absorption or two components or whether the cloud had an infalling envelope or colliding cores. Having examined various line shapes and their radial distributions, we have come to a point that these exclusive arguments to their alternatives could not satisfactory explain the true nature of the W49A molecular cloud core any more. In this subsection we review and discuss arguments so far made on the 8 km s^{-1} dip in literature in comparison with the present study, concluding that both foreground absorbing gas and two clouds exist toward W49A as was pointed out by MHH.

It is already evident that there is cold, foreground absorbing gas at 8 km s^{-1} toward W49A as has been detected as the 8 km s^{-1} dips seen in the optically thick, deep dip lines such as in ^{12}CO ($J = 1 - 0$), HCO^+ ($J = 1 - 0$), and HCN ($J = 1 - 0$). The following arguments strengthen this conclusion.

Mufson and Liszt (1977) discussed that the similarity in the ^{12}CO and the ^{13}CO profiles implies the existence of two clouds and that an H II region lies between them based on the

argument that the velocity of the recombination lines is in the middle of the velocities of the two peaks seen in the ^{12}CO line. Phillips *et al.* (1981) compared the $J = 1 - 0$ and $J = 2 - 1$ emission of ^{12}CO and found that the ^{12}CO emission is optically thick. They claimed that the lines of ^{13}CO do not have the same shape and concluded that the dip at V_{LSR}=8 km s^{-1} is due to optically thick absorption by cold foreground gas. Most of the studies that observed deep dip lines reached this conclusion.

An important point is that the above arguments about deep dip lines do not rule out the existence of two velocity components at 4 and 11 km s^{-1} inside the massive core of W49A. There is actually an increasing number of evidence that at least two fragmented clouds exist within the W49A core. MHH suggested this based on their CS ($J = 1 - 0$) and C^{34}S ($J = 1 - 0$) observations. They showed that, although ^{12}CO does have self-absorption, optically thin C^{34}S ($J = 1 - 0$) line profile contains two velocity components with their spatial distribution different from each other.

The present study of various line profiles confirmed this suggestion. All the observed optically thin line profiles, except for the shock indicators, have double peaks with a shallow dip. On the contrary to the case of deep dip lines, the dips are shallow enough such that they can naturally be understood as a result of overlapping two velocity components. Examining the three shallow dip lines ^{13}CO ($J = 1 - 0$), C^{18}O ($J = 1 - 0$), HCO$^+$ ($J = 1 - 0$) with high signal to noise ratio, we notice that their peak velocities are remarkably coincident with each other at 4.2±0.3 and 10.6±0.2, whereas the dip velocities have a larger dispersion. Comparison of these three line profiles in Figure 2-1b demonstrates that the dip velocity varies as the relative strength of the blue- and redshifted peaks changes; the dip is located just at the center of the two peaks for ^{13}CO ($J = 1 - 0$) and C^{18}O ($J = 1 - 0$) that have comparable blue- and redshifted peak intensities, while the dip is located relatively at redshifted velocity in the case of HCO$^+$ ($J = 1 - 0$) that has much stronger blueshifted peak intensity. The C^{34}S lines in Figure 2-1c show an opposite tendency to HCO$^+$ that the redshifted peak feature is stronger. We can naturally understand these facts when the two velocity components exist in the W49A cloud core with their corresponding line intensities different from one another reflecting the difference in their physical and chemical conditions.

Boreiko and Betz (1991) presented the line profile of the $J = 9 - 8$ transition of ^{12}CO, which traces regions of both high temperature and density without being affected by cold less excited foreground gas. Finding that the ^{12}CO ($J = 9 - 8$) line has two peaks at V_{LSR}=3.0 km s^{-1} and 12.4 km s^{-1}, they suggested that it would be difficult to envision physical conditions if its dip were due to self-absorption. They maintained a combination of both alternatives, self-absorption and two clouds, as suggested by MHH.

Serabyn *et al.* (1993) mapped W49A with rotational transitions of C^{32}S and C^{34}S in a wide range of excitation from $J = 3-2$ to $J = 10-9$. They found three CS clumps located in the massive core. The clump velocities are at 4 and 12 km s^{-1}, which are consistent

with what were suggested by the above line profile analyses. Serabyn *et al.* (1993) also suggested that the kinematics of the CS clumps support the hypothesis of cloud-cloud collision as was pointed out by MHH.

Jaffe, Harris, and Genzel (1987) discussed that, because the $J = 7 - 6$ transition of ^{12}CO emission have a single peak, W49A consists of one velocity component with a large velocity dispersion of 14 km s^{-1}. This result apparently contradicts with the result of the $J = 9 - 8$ observation (Boreiko and Bets 1991), which shows a clear, shallow dip at the line center. I speculate that the low signal-to-noise ratio together with a low velocity dispersion for the $J = 7 - 6$ data made it impossible to identify the shallow dip which might otherwise detectable at the line center. For example, I convolved a shallow dip line profile of C^{34}S ($J = 1 - 0$) obtained by MHH so that the spectrum had the same velocity resolution of 1.2 km s^{-1} as the $J = 7 - 6$ data, finding that the central dip became unidentifiable.

For summary we conclude that, although optically thick lines with low excitation are affected by the 8 km s^{-1} absorption gas, many of the other line profiles that are not significantly affected by it suggest the presence of at least two velocity components within the massive core of W49A. Lower transition levels of optically thick lines are significantly affected by the cold, foreground absorbing gas, so that they are not suitable for the detailed study of the massive core itself. On the other hand optically thin lines or optically thick lines with high excitation are free from foreground gas absorption, with which we can probe into detailed structure of the W49A. Some of the lines such as SiO or SO do not show evidence of shallow dips, although they are not very optically thick. We argued in the previous section that these are molecular transitions which are known to need special excitation conditions such as shocks. I will discuss the characteristics of these lines later.

4.1.2. The 17 km s^{-1} Dip

Nyman and Miller (1989) suggested that a feature at V_{LSR}=17 km s^{-1}, which is best seen toward W49N, is caused by either the outer part of the Aqula Rift local molecular cloud (Dame and Thaddeus 1985) or infalling gas in the center of W49N (Welch *et al.* 1987). The 17 km s^{-1} feature is, however, not due to Aqula Rift because the 17 km s^{-1} component around W49N and W49S are apparently associated with them (Chapter 6). OH masers have velocities around V_{LSR}~17 km s^{-1}(*e.g.*, Gaume and Mutel 1987). So the absorption at 17 km s^{-1} may exist around the W49A core. Indeed the ^{12}CO distribution at 17 km s^{-1} shows absorption feature around the W49A core in Chapter 3.

4.1.3. Comparison with Interferometric Line Profiles

Welch *et al.* (1987) claimed the collapse of the core by interpreting the absorption of HCO$^+$ due to infall. Both emission and absorption over the velocity range from -10 to 30 km s^{-1} arise from the W49A complex and line profile show dips at ~8 km

s^{-1} and ~17 km s^{-1}. There is difference between spectra obtained with a single dish telescope and an interferometer. The single dish spectra have two peaks at 4km s^{-1} and 12km s^{-1} as suggested by MHH, while those with interferometer show absorption over the range from 11 km s^{-1} to 21km s^{-1}. The difference of emission and absorption are related to the brightness temperature between line and continuum emissions, because the line brightness temperature by averaged over a smaller beam may become less than the continuum brightness temperature. The continuum brightness temperature obtained with the interferometer was much high because of smaller beam dilution. We will discuss in Chapter 3 and Chapter 5 about the collapse of the core. Jackson and Kraemer (1994) also suggested from their NH_3 observations that the infall velocity of ~10 km $s^{-1}$is consistent with parsec-scale gravitational collapse toward the massive molecular cloud core.

4.2. Density and Temperature Distribution

There are many works which studied the density distribution of molecular clouds. Snell, Langer, and Frerking (1982) determined the density structure in several dark clouds from CS observations. Arquilla and Goldsmith (1985) investigated the density distribution of seven dark clouds using ^{12}CO and ^{13}CO molecules. Frerking, Langer, and Wilson (1987) studied the structure, dynamically properties, density, mass, and temperature of the globule B335. The gas kinetic temperature is usually determined from ^{12}CO ($J = 1 - 0$) line transitions. The $J = 1 - 0$ transition of ^{12}CO is optically thick and thermalized, so that the observed intensity, which corresponds to the excitation temperature of the transition, is equal to the gas kinetic temperature of the cloud.

Other method to estimate the kinetic temperature is the use of NH_3 lines. The rotational temperature of NH_3 hyperfine transitions is measured (Martin and Barrett 1978). For example Bachiller, Guilloteau, and Kahane (1987) determined the density and temperature of clumps in IC348 using NH_3. On the other hand, some of the massive star forming regions such as Sgr B2 (Lis and Goldsmith 1990) and G10.6-0.4 (Keto and Ho 1989) were investigated both in CO and NH_3.

4.2.1. Density Distribution

If the cloud radius R is estimated from the total extent of the ^{13}CO map (Chapter 3), then a density law can be integrated along each line of sight through the cloud envelope, giving theoretically predicted column densities $N(p)$,

$$N(p) = (2\rho_0 r^{\gamma}) m_{H_2}{}^{-1} \int_0^{ZR} (z^2 + p^2)^{-1/2} dz \qquad (cm^{-2}) \qquad (2.1.)$$

where $ZR = (r^2 - p^2)^{-1/2}$ Z is distance along wach line of sight from the cloud mid plane, p is the impact parameter with respect to the clou center, and ρ_0 and r_0 are the mass density and radius, respectively.

As shown in Table 2-3 the radial density distribution of the massive core has $I \propto r^{-1}$ for ^{13}CO. The column density is then proportional to the integrated intensity $N \propto I$. These results of optically thin, sufficiently excited lines give the radial distribution of column density for these molecules proportional to r^{-1}, $N(^{13}CO) \propto r^{-1}$, so that the column density of hydrogen molecule is also proportional to r^{-1}, $N(H_2) \propto r^{-1}$. The radial distribution of the hydrogen molecule number density is proportional to r^{-2}, $n(H_2) \propto r^{-2}$, from the relation between the column density and the number density.

The SiO column density was derived from the following equation for the transition J+1→ J:

$$N(SiO) = \frac{3k \times 10^5 T_{rot} \int T_R dv}{8\pi^3 \mu_0^2 \nu B_0 (J+1) exp(-\Delta E / kT_{rot})}, \qquad (2.2.)$$

where B_0 is the molecule's rotational constant, ΔE is the energy of the J-th level above ground state, μ_0 is the permanent dipole moment of SiO (μ_0=3.098 Dbye), ν is frequencies of the $J = 1 - 0$ and $J = 2 - 1$ transition, T_{rot} is the rotational temperature, and $\int T_R dv$ is the integrated intensity of the SiO lines corrected for beam efficiencies. As shown in Table 2-4 the beam dilution is dominant for SiO, so that smaller beam observations with the NRO 45m telescope give larger brightness temperature than with larger beams. The integrated intensity of the SiO $J = 1 - 0$ and $J = 2 - 1$ transitions are 53.3 and 68.0, respectively.

TABLE 2-4

Line Intensity of SiO($J = 1 - 0$ and $J = 2 - 1$), $H^{13}CO^+$, and SO_2

Telescope	HPBW [arcsec]	Temperature Scale	$H^{13}CO^+$	SiO($J = 1 - 0$)	SiO($J = 2 - 1$)	SO_2
NRO(45m)[a]	19″	$T_A^*(T_B)$	1.3	—	2.00(4.17)	0.4
NRO(45m)[a]	35″	$T_A^*(T_B)$	—	0.74(1.09)	—	—
Onsala(20m)[b]	43″	T_B	0.8	—	1.4	—
NRAO(12m)[c]	72″	T_R^*	0.42	—	—	~0.07
Haystack(43m)[d]	45″	T_B	—	0.74	—	—

[a] This work; Source coordinate is $\alpha(1950) = 19^h07^m49^s.8$, $\delta(1950) = 9^o01'15''.5$. Value is the antenna temperature and ( ) is the brightness temperature. [b] Downes *et al.* (1982); Source coordinate is $\alpha(1950) = 19^h07^m50^s.0$, $\delta(1950) = 9^o01'17''$. Value is the brightness temperature. [c] Scheneverk *et al.* (1988); Source coordinate is $\alpha(1950) = 19^h07^m50^s.0$, $\delta(1950) = 9^o01'17''$. Value is the brightness temperature. [d] Hashick and Ho (1990); Source coordinate is $\alpha(1950) = 19^h07^m49^s.8$, $\delta(1950) = 9^o01'17''$. Value is the brightness temperature.

In equation (2.2.) we assumed that T_R is equal to the brightness temperature deduced from the antenna temperature. We obtained the rotational temperature, T_{rot} under the optically thin condition as,

$$T_{rot} = \frac{-4hB_0}{kln[T_B(2-1)/4T_B(2-1)]}. \quad (2.3.)$$

We then obtain the rotational temperature of 3.6 K, which is lower than expected. Since SiO emission arises from high temperature region like Orion KL, it is likely that either the gas is not optically thin or the excitation of gas is not in thermal equilibrium (Haschick and Ho 1990). Near equality of observed line intensity ratio of SiO means a modest optical depth. Haschick and Ho (1990) suggested that the SiO emission is likely to originate all from small optically thick and hot sources, which is supported by the redults in Figure2-2c.

I hence set the rotational temperature of the $J = 2 - 1$ transition to be 100 K or more (Wright *et al.* 1983), which is consistent with interferometric results (Chapter 5). The column density N(SiO) is calculated to be $7.2 \times 10^{17}\ cm^{-2}$. The abundance of SiO molecule is calculated to be N(SiO)/N(H_2)=2.0×10^{-9}. This value is higher than those in dark clouds. The radial distribution of SiO is steeper than of ^{13}CO. This implies that the gas temperature increases toward the core and the abundance of SiO also increases.

4.2.2. Temperature Distribution

Observing molecular clouds with various temperature, Ziurys, Freberg, and Irvine (1989) suggested that the SiO molecule may be an ambiguous indicator of high-temperature chemistry. HCN and H^{13}CN has a dipole moment of2.98 Debye, which is similar to that of SiO. It implies that both molecules should have similar excitation requirements. Because the abundance of HCN is supposed to be unaffected by high temperature (Iglesias and Silk 1978), HCN was chosen as a comparison molecular species of SiO. From our works correlation between SiO and HCN are derived as follows.

$$[SiO/HCN] \propto r^{-(0.3\sim0.5)} \quad (2.4.)$$

On the other hand, Ziurys, Freberg, and Irvine (1989) induced that

$$ln[SiO/HCN] \propto 1/T_K \quad (2.5.)$$

If abundance of HCN do not change with temperature, then

$$[SiO] \propto exp(-E_{act}/T_K) \quad (2.6.)$$

where E_{act} is activation energy as Ziurys, Freberg, and Irvine (1989) suggested. They concluded that E_{act}=86 K is required for SiO to be to formed. Herbst *et al.* (1989) reported that the activation energy might reflect a barrier against thermal disruption of silicon from an icy mantle and such disruption could occur in warm or shock regions near photodissociation zones.

In the case of W49A, warm and/or shock regions exist near the component g. Welch *et al.* (1987) suggested that the velocity of accreting gas toward the "necklace" reaches and exceeds both the isothermal sound speed and the Alfvén velocity in magnetic field, when it passes through standing shocks. In these shock regions the abundance of SiO is enhanced as in IC443 (Ziurys, Snell, and Dickman 1989), where SO and SO_2 becomes also unusually abundant. These 'hot core' molecules in W49A may be excited in high temperature regions where there are shocks due to bipolar flows, accretion, cloud-cloud collisions or other mechanisms.

It may not be true to assume that SiO and HCN emissions come from the same region as suggested by Martin-Pintado *et al.* (1992). As shown in Figure 1b and 1c, the two spectra are different from each other. HCN spectra would have two peaks as discussed in the previous section even if there was no self-absorption like optically thin lines, while SiO has a simple peak with broad wing. The emiitting regions of these lines may be spatially difference from each other.

4.3 Collapse of the Surrounding Envelope

Welch *et al.* (1987) observed inverse P-Cygni profiles of HCO^+ toward strong continuum sources at the center of W49A, suggesting that W49A has an infalling envelope as is the case observed for other massive star forming regions. Presence of infalling gas is consistent with the presence of many cloudlets in the W49A core. Keto and Monaghan (1989) made numerical simulations of the collapse of an unstable massive core. Their results showed that fragmentation leads to the formation of many cloudlets toward which surrounding gas keeps infalling. Those cloudlets are naturally regarded as different velocity components observed in line profiles or observed as the rotating necklace of H II regions with surrounding gas. As was pointed out by MHH, the problem is why such an unstable core has formed. MHH speculated the formation of massive unstable core under the influence of magnetic field, the collapse of which might be triggered by a cloud collision. Theoretical consideration shows that such supercritical clouds may need no special trigger for the collapse (Shu, Adams, and Lizano 1987). We will consider the collapse of the cloud in Chapter 3 and Chapter 5.

5. CONCLUSIONS

I have obtained spectra of various molecules, and classify them into three types by their line shapes: spectra showing double peaks with a deep dip, spectra with a shallow dip, and spectra with a single peak. These are called as "deep dip lines", "shallow dip lines," and "single peak lines," respectively. ^{12}CO ($J = 1 - 0$), HCO$^+$ ($J = 1 - 0$), and HCN ($J = 1 - 0$) are classified into deep dip lines. ^{13}CO ($J = 1 - 0$), C^{18}O ($J = 1 - 0$), HCO$^+$ ($J = 1 - 0$), and C^{34}S ($J = 2 - 1$) are shallow dip lines. I also classify C^{34}S ($J = 1 - 0$) and SO_2 into the shallow dip lines because they can be regarded as a shallow dip case with much weaker blueshifted peaks. C^{32}S($J = 2 - 1$) (Nyman 1984) and HNC (Nyman and Miller 1989) are also classified into this type. SiO and SO are single peak lines.

Assuming that the W49A molecular cloud core has circular symmetry, radial distributions of molecules are presented. The intensities decrease monotonically from the center to outward with moderate dispersion, suggesting that the assumption of circular symmetry was not so bad. This enables us to make a power law fit to each radial distribution. The optically thin lines with thermalized excitation such as ^{13}CO, and C^{18}O have relatively flat distribution with the power law index close to 1. The optically thick lines HCO$^+$ and HCN also show the similar flat radial profile. The optically thin lines with subthermal excitation such as H^{13}CO$^+$ and H^{13}CN tend to have a steeper decrease with the power law index close to 1.5. The single peak lines SiO and SO show the steepest decrease comparable to the beam shape, suggesting that these line emissions are localized to a compact region at the center of the W49A molecular cloud.

Radial distributions of column density of the observed molecule are estimated from the integrated intensity. From the results of sufficiently excited optically thin lines, the radial distributions of the column density is derived to have the depoendence of r^{-1}, which means that the column density of hydrogen molecule is also proportional to r^{-1}. Assuming spherical symmetry, the radial distribution of the hydrogen molecule number density is then proportional to r^{-2}. Results of the SiO emission show that temperature is very high in the "necklace" region.

Chapter 3

STRUCTURE AND KINEMATICS IN MASSIVE CORE

1. STRUCTURE AROUND MASSIVE CORE

I have reported the structure of the W49 A massive core (MHH) and its density distribution in Chapter 2. The existence of two peaks at V_{LSR}= 4 and 12 km s^{-1} for optically thin lines means that the W49A complex has two velocity components. MHH presented the distribution of the integrated emission of CS, which resembles that of the 1 mm continuum emission (Westbrook *et al.* 1976). This suggests that the CS emission well traces the column density of dense molecular gas core of W49A complex with its size of 50″ or 3.0 pc. The mass of the core is estimated to be (0.5-2.5) $\times 10^5$ M$_\odot$, which is comparable to that of a typical giant molecular cloud. Such large mass is closely packed in a small region of 3.0 pc in diameter. Since the mass is an order of magnitude larger than the virial mass, the massive core should collapse unless there is some supporting mechanism such as the magnetic field.

Active star formation in W49A is assumed to be caused by a trigger. The star formation rate in the W49A core region has suddenly increased $10^4 - 10^5$ *yr* ago, indicating a triggered burst of star formation. MHH supposed that collision of the two clouds might have triggered the star formation in the massive core, producing clusters of new O stars. Recently Serabyn, Güsten, and Schulz (1993) presented multi-transition observations of C^{32}S and C^{34}S molecules, and suggested that their observations support our scenario.

In this chapter, I present maps of various molecules, ^{12}CO, ^{13}CO, HCO$^+$, H^{13}CO$^+$, and HCN, for several mapping areas. On the basis of this information I will discuss the relationship between the structure of the molecular cloud core and its star forming activities.

2. OBSERVATIONS WITH THE 45 M TELESCOPE

Observations were made from 1986 to 1988 using the 45 *m* telescope of NRO. In 1986 I made small scale mapping observations with ^{12}CO line to study overall structure of the W49A core and to search for available off positions because high resolution observations had not been carried out before. In 1987 small scale mapping with ^{13}CO, HCO$^+$, and HCN were made. In 1988 I carried out small scale 60″×60″ mapping with H^{13}CO$^+$ to resolve the structure and kinematics around the rotating necklace in the W49A core.

The parameters of observation were the same one as those mentioned in chapter 2. Spectral data were taken with 16 banks of acousto-optical spectrometers (AOS) with

32,000 channels in total. Eight of them were high-resolution AOSs with a frequency coverage of 40 MHz each and a resolution of 37 kHz, which corresponds to the velocity resolution of 0.10–0.13 km s^{-1} at 86–110 GHz. The other eight banks were wide-band AOSs with a frequency coverage of 250 MHz each and a resolution of 250 kHz, which corresponds to the velocity resolution of 0.68–0.87 km s^{-1} at 86–110 GHz.

The pointing of the antenna was carefully checked during the observations by monitoring the SiO maser emission (v=1; $J = 1 - 0$) from R Aql at α(1950) =$19^h03^m57\overset{s}{.}68$, δ(1950) = $8°09'7\overset{''}{.}7$ every 2 hours. The change in antenna pointing was within 5″ in most cases. I did not use the data when subsequent pointing varied more than 10 ″, which sometimes occured under strong wind conditions. The central position of all the observations was taken to be α(1950) = $19^h07^m49\overset{s}{.}8$, δ(1950) = $9°01'15\overset{''}{.}5$ as was the same for the observations presented in Chapter 2.

Because there are several extended components toward W49A at 4 km s^{-1}, 12 km s^{-1}, 40 km s^{-1} (Chapter 2), and 60 km s^{-1} I needed observations to search off positions that were free from ^{12}CO emission in order to use a position switching mode. The off position search was made with declination scans by 1′ step, and I selected a reference position +17′ away in declination where the ^{12}CO emission was not detected above the 1 K level. Calibration was achieved by the standard chopper wheel method. The reference spectrum at the mapping center was observed recurrently so that the variation of antenna gain was checked. The intensity scale is the antenna temperature, T_A^*, which was corrected for atmospheric and ohmic losses (Ulich and Haas 1976).

I carried out three kinds of observations, mapping observations of ^{12}CO in an area of 200″ × 200″ ($\alpha \times \delta$) with a grid spacing of 30″ or1.70 pc, mapping with ^{13}CO, HCO$^+$, and HCN lines in an area of 2′ × 2′ ($\alpha \times \delta$) with a grid spacing of 20″ or 1.13 pc, and mapping with H^{13}CO$^+$in an area of 60″ × 60″ ($\alpha \times \delta$) with a grid spacing of 10″ or 0.57 pc toward center of W49A. Scanning effect was minimized by adding maps taken with right ascension and declination scans.

3. RESULTS OF SMALL SCALE MAPPING

3.1. Results of ^{12}CO Observations

3.1.1. Velocity Components of ^{12}CO toward W49A Core

^{12}CO, HCO$^+$, and HCN spectra toward the center position are shown in Figure 3-1. The velocity cpverage of each spectrum is from -60 km s^{-1} to 100 km s^{-1}. The ^{12}CO emission has several peaks at 4 km s^{-1}, 12 km s^{-1}, 20 km s^{-1}, 40 km s^{-1}, and 60 km s^{-1}. Spectra of ^{12}CO, HCO$^+$, and HCN consist of three components, the main component, the halo component, and the high velocity component. The high velocity component is seen

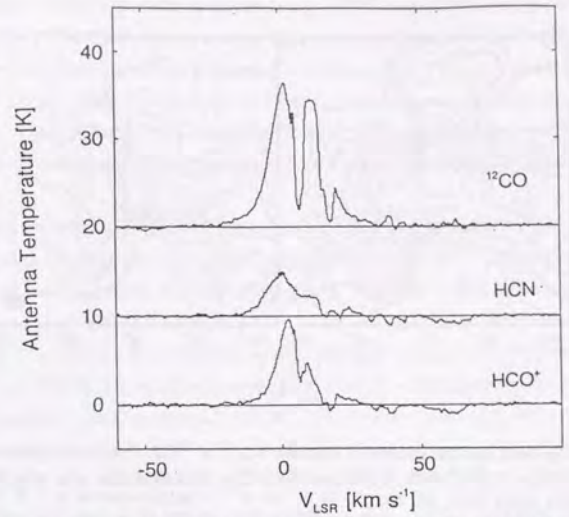

Figure 3-1: Spectra of ^{12}CO, HCO$^+$, and HCN. Obtained ^{12}CO, HCO$^+$, and HCN spectra toward central position has velocity range from -60 km s^{-1} to 100 km s^{-1}.

in the wing emission (ΔV_{zp}> 55 km s^{-1}) in the ^{12}CO line as well as in HCO$^+$, and HCN lines. The red wing has a sharp absorption feature at 17 km s^{-1}. The center velocity of the wing emission is about 8 km s^{-1}.

^{12}CO, HCO$^+$, and HCN have absorption features at V_{LSR}= 8km s^{-1} and 17-19 km s^{-1}. Other absorption features (*e.g.*, HCO$^+$, C^{32}S ($J = 2 - 1$ and $J = 1 - 0$), and C_3H_2) at V_{LSR}= 40 km s^{-1} and 60 km s^{-1} (Nyman 1983, 1984; Miyawaki, Hasegawa, and Hayashi 1988; Nyman and Miller 1989; Matthews and Irvine 1985; Cox, Güsten, and Henkel 1988) are formed by foreground diffuse molecular gas in the Sagittarius arm. I do not discuss those absorption features from because those are not associated with the W49A molecular cloud complex.

Intensity of the continuum emission was estimated from the depths of absorption features at 30–60 km s^{-1} of HCO$^+$ and HCN. Nyman (1983; 1984) and Nyman and Miller (1989) suggested that absorption features of various molecular lines went down to the cosmic background radiation levels because they are optically thick and not excited. On this assumption, I get the continuum brightness of T_A^*=0.50 K or T_B=1.04 K.

3.1.2. Distribution of ^{12}CO around W49A Core

Our ^{12}CO maps shows higher resolution views of W49A than other ^{12}CO results of

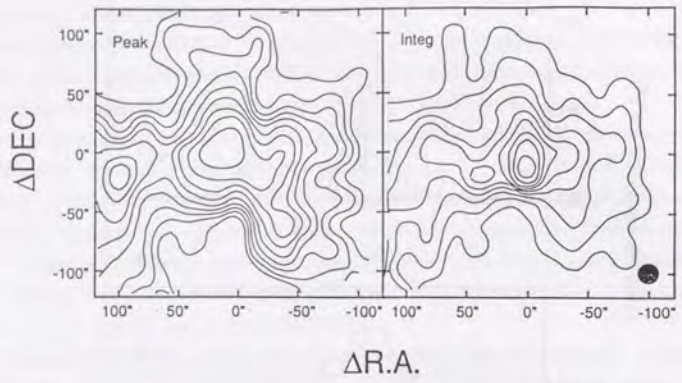

Figure 3-2: The Peak and the Integrated Intensity Maps of ^{12}CO. Positional offsets are taken from $\alpha(1950) = 19^h07^m49\overset{s}{.}8$, $\delta(1950) = 9°01'15\overset{''}{.}5$. (left) Peak intensity map of ^{12}CO at the velocity range from -30 km s^{-1} to 30 km s^{-1}. Contour interval is 1 K from 5 K. (right) the integrated intensity map of ^{12}CO at the velocity range from -30 km s^{-1} to 30 km s^{-1}. Contour interval is 20 Kkm s^{-1} from 50 Kkm s^{-1}.

moderate resolutions (65″) (Mufson and Liszt 1977). Figure 3-2 shows the peak and the integrated intensity maps of ^{12}CO. The peak intensity map of Figure 3-2a has two peaks toward W49N and toward (100″, 20″). The ^{12}CO peak intensity map is similar to that of the 53 μm emission that is elongated toward the southwest (Harvey *et al.* 1977). The 23 GHz continuum emission also show similar elongation (Wink *et al.* 1975). There are other elongated structures to the north that are divided into two at (0″, 75″). These are similar to a previous $C^{32}S(J = 1 - 0)$ peak intensity map (MHH). The similarity between the ^{12}CO line and 53 μm continuum emission maps is a natural consequence if the ^{12}CO intensity reflects the gas temperature distribution. The 53 μm emission arises from hot (several hundreds of kelvins) dust grains in the H II region. The hot dust is surround by molecular gas with lower temperature. The different distribution between the ^{12}CO line and $C^{32}S$ line (MHH), that is similar to the 1 mm continuum emission (Westbrook *et al.* 1976), is the difference of the distribution between the gas temperature and column density of molecular gas. The elongation of ^{12}CO toward the southeast is consistent with the $C^{32}S$ results. The distribution of ^{12}CO partially resembles that of $^{12}CO(J = 2 - 1)$ (Schloerb, Snell and Schwarz 1987) in its east, west, north, and south-west elongations.

The integrated intensity map has elongations toward three directions; to the north, which is similar to the integrated intensity of ^{12}CO taken at the Owens Valley Radio Observatory (OVRO) (Scoville *et al.* 1986), east, and west.

Figure 3-3 shows the velocity channel maps of ^{12}CO emission averaged over a 2 km s^{-1} and a 1 km s^{-1} interval. On the basis of the results in Chapter 2, the distribution of ^{12}CO emission is divided into two components; one is from -1 to 5 km s^{-1}, and the other is from 10 to 14 km s^{-1}. Distribution around 8 km s^{-1} is not important because the line profile at 8 km s^{-1} is self-absorbed as discussed in Chapter 2. Figure 3-4 shows ^{12}CO spectra along the right ascension and declination strips. The 8 km s^{-1} absorption is apparent toward all positions.

The maps at 4 km s^{-1} and 12 km s^{-1} show different distribution although their peaks are almost at the same position of the component C. The 4 km s^{-1} component is elongated to the east, west and north, as is the case for the $C^{32}S(J = 1 - 0)$ emission (MHH). At the southern edge of W49N, the intensity of the 4 km s^{-1} component falls down. A fain peak is at (75″,0″). The 12 km s^{-1} component is elongated toward the southwest, northwest, north from W49N. The southwest elongation seems to correspond to the distribution of the 53 μm map. Another peak is at (100″,-25″), which is also seen in the peak intensity map.

Distribution of the high velocity wing was very compact so that it was not much resolved out. Maps of the velocities at -5 km s^{-1} and 21 km s^{-1}, where line profiles are free absorption features, reveal that peaks at different from each other. The peak at -5 km s^{-1} is located at (0″, -15″) and that of 21 km s^{-1} is at (15″,-20″). This difference is similar to single dish results of the high velocity flow (Scoville *et al.* 1986).

The 17 km s^{-1} absorption feature is detected against the emission wing of the 12 km s^{-1} emission. Figure 3-5 shows the distribution of the detected 17 km s^{-1} absorption feature. The 17 km s^{-1} absorption feature is distributed around (0″,0″) with dominant features seen in the west of W49A. It is not, however, clear whether there is the 17 km s^{-1} component only around (0″,0″) or all over the field of W49A because I could not detect the 17 km s^{-1} absorption feature to the positions where there is no 12 km s^{-1} emission detected. The 17 km s^{-1} component is assumed to surround the W49A core, especially for southeast of W49N, because of the similarity between continuum image and 17 km s^{-1} absorption distribution.

3.2. Results of ^{13}CO Observations

3.2.1. ^{13}CO Small Scale Distribution

Figure 3-6 shows the distribution of the integrated intensity of ^{13}CO, HCO^+, and HCN emission compared with Dieter *et al.* (1979). The integrated intensity, I(^{13}CO), is strong at the component g. The peak of ^{13}CO is at (0″,0″) and its distribution have elongations to the north, southeast and southwest from the peak. The peak is not resolved out. The peak of ^{13}CO coincides with the infrared emission and radio continuum emission (Dieter

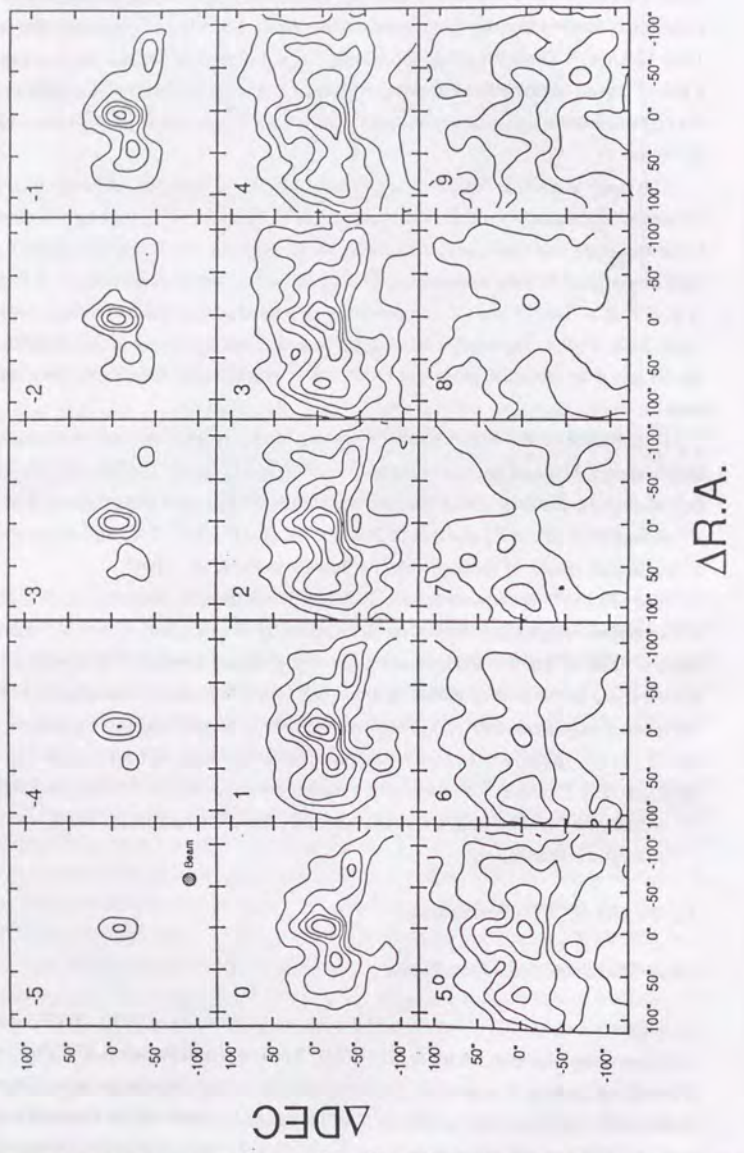

Figure 3-3a: The Equivelocity Maps of ^{12}CO. The equivelocity maps of antenna temperature averaged over 2 km s^{-1} centered on the velocities from -5 km s^{-1} to 21 km s^{-1}. The Positional offsets are taken from $\alpha(1950) = 19^h07^m49^s.8$, $\delta(1950) = 9°01'15''.5$. Contour interval is 2 K from 2 K.

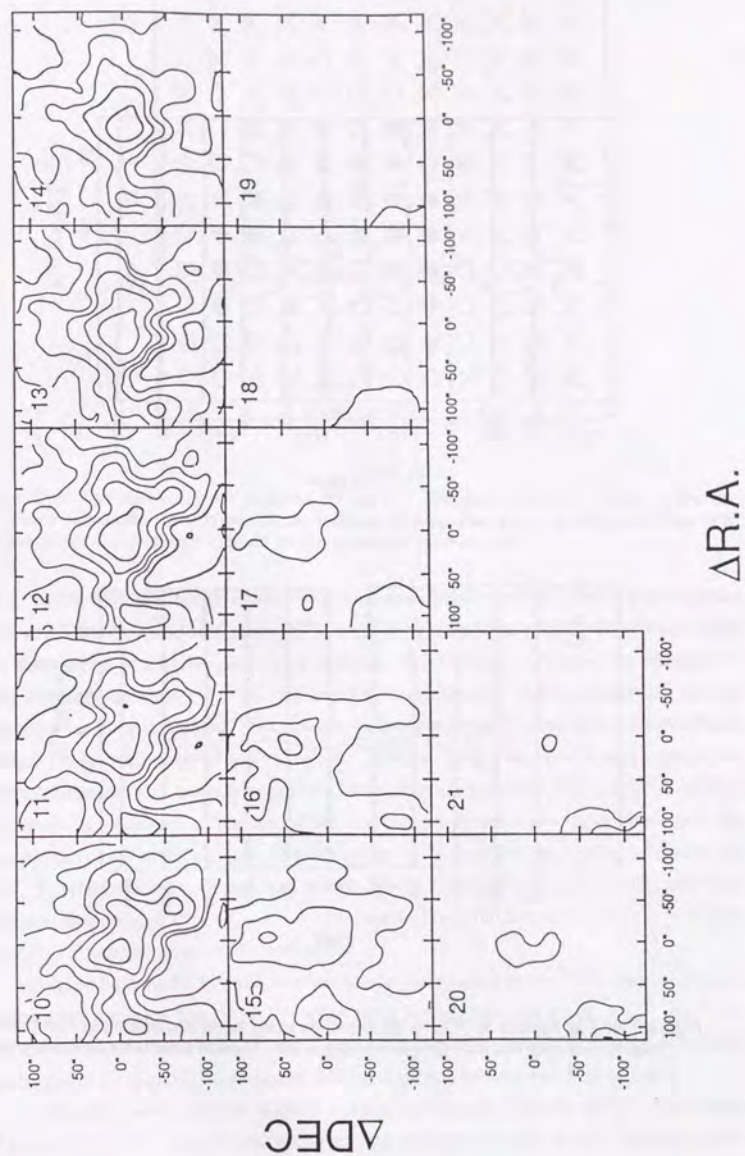

Figure 3-3b: The Equivelocity Maps of ^{12}CO.

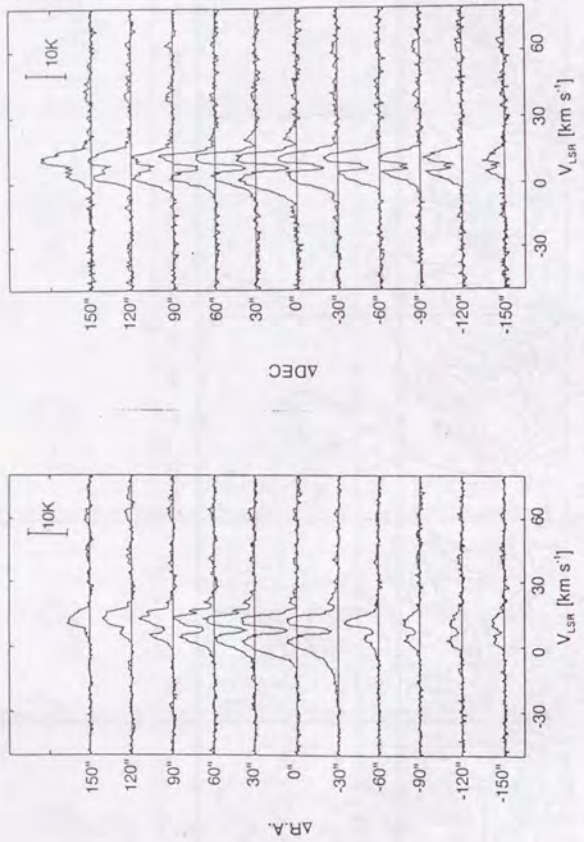

Figure 3-4: The Spectra of ^{12}CO in the Direction along Right Ascension (left) and Declination (right). For each direction the grid spacing is 30″. Vertical scale is the antenna temperature.

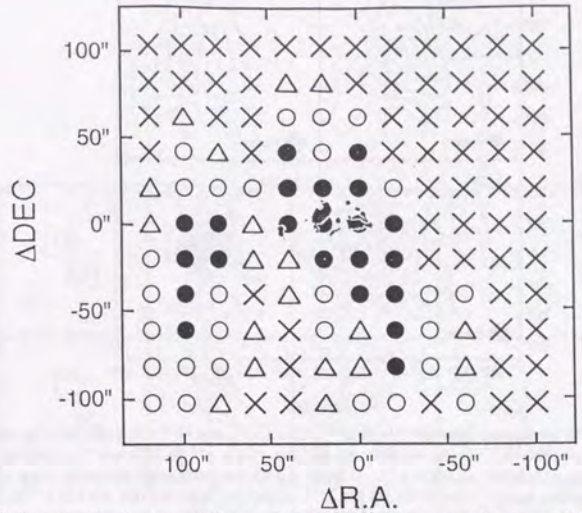

Figure 3-5: The distribution of Detected 17 km s^{-1} Absorption Feature. Filled circles indicate remarkable absorption, circles indicate slightly absorption, triangles indicate less remarkable, and crosses indicate no absorption or baseline level.

et al. 1979). The distribution of the ^{13}CO emission is similar to that of the 53 μm emission (Harvey, Campbell, and Hoffmann 1977) with elongation to the southwest, toward which the distribution of 23 GHz continuum emission (Wink *et al.* 1975) also has elongation. The similarity between the ^{13}CO line and 53 μm continuum emission maps is a natural consequence if the integrated ^{13}CO intensity is not absorbed by foreground gas and reflects the gas temperature distribution as well as ^{12}CO, suggesting that hot dust is surrounded by molecular gas with lower temperature. The difference between ^{13}CO and C^{32}S (MHH) distributions means the difference of the distribution between gas temperature and the column density of molecular gas. The elongation of ^{13}CO toward the southeast is common in C^{32}S (MHH; Serabyn, Güsten, and Schulz 1993). The distribution of ^{13}CO is, however, different from that of C^{18}O($J = 2 - 1$) (Schloerb, Snell and Schwarz 1987) with a peak at (20″,-20″) and south-west elongation.

In Figure 3-6b the HCO$^+$ emission has similar distribution as the ^{13}CO 'core' emission. Because the emission line of HCO$^+$ arises from high density region of $> 10^5\ cm^{-3}$, its emission is concentrated in the 'core'. Large mass is packed in the core as suggested from the results of C^{32}S and C^{34}S emission (MHH; Serabyn, Güsten, and Schulz 1993).

On the other hand, the peak of HCN is different from the ^{13}CO and HCO$^+$. The center of peak is (-15″,0″). The peak at (40″,-25″) and a southwest elongation is, however, have

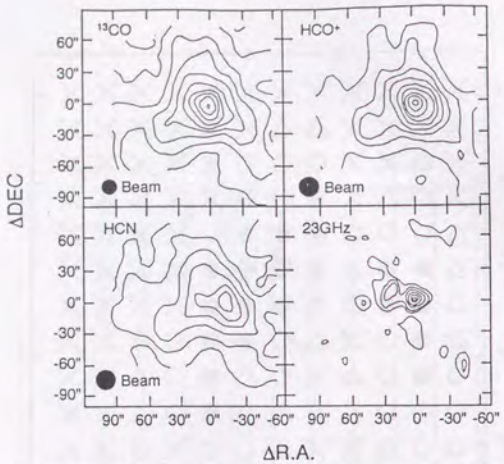

Figure 3-6: The Integrated Intensity Maps of ^{13}CO, HCO$^+$, and HCN. (Upper left) the integrated intensity map of ^{13}CO at the velocity range from -5 km s^{-1} to 20 km s^{-1}. Contour interval is 10 Kkm s^{-1} from 10 Kkm s^{-1}. (Upper right) the integrated intensity map of HCO$^+$ at the velocity range from -5 to 20 km s^{-1}. Contour intervals are 10 km s^{-1}K from 10 km s^{-1}K. (Lower left) the integrated intensity map of HCN at the velocity range from -5 to 20 km s^{-1}. Contour intervals are 10 K km s^{-1} from 10 Kkm s^{-1}. (Lower right) the continuum image at 23 GHz (Dieter *et al.* 1979). The contours are at levels 0.2, 0.5, 1.3, 2.0, 2.7, and 3.5 Jy per beam. The brightest compact source correspond to component C.

the same tendency as ^{13}CO and HCO$^+$. HCN is the molecule whose abundance is not supposed to be affected by temperature (Iglesias and Silk 1978). It means that image of HCN present neither temperature distribution as ^{13}CO nor density distribution as HCO$^+$, but column density of molecular gas as well as CS (MHH; Serabyn, Güsten, and Schulz 1993).

3.2.2. Velocity Structure

Figure 3-7 shows the equivelocity maps of the ^{13}CO emission averaged over 2 km s^{-1} interval. At the velocity of 5–7 km s^{-1} the 'core' is elongated toward the west, while it is elongated toward the southwest at the velocity of 8–14 km s^{-1}. The southeastern part of the 'envelope' is associated with the compact H II regions I and J (Wink *et al.* 1975) at the velocity of 11–12 km s^{-1}, while the envelope has another extension at 15″ west at 0–6 km s^{-1}, at the north at 3–15 km s^{-1}, and at (40″,-25″).

Figure 3-8 shows the equivelocity maps of the HCO$^+$ emission averaged over 2 km s^{-1} interval. The HCO$^+$ emission has concentration like ^{13}CO in the 'core' at -6–5 km s^{-1} and has another peak at (40″,-25″) at -6–2 km s^{-1}. The ^{13}CO 'envelope' is also elongated toward the north and southwest.

Figure 3-9a and 3-9b show position-velocity maps of the C^{18}O and the H^{13}CO$^+$ line

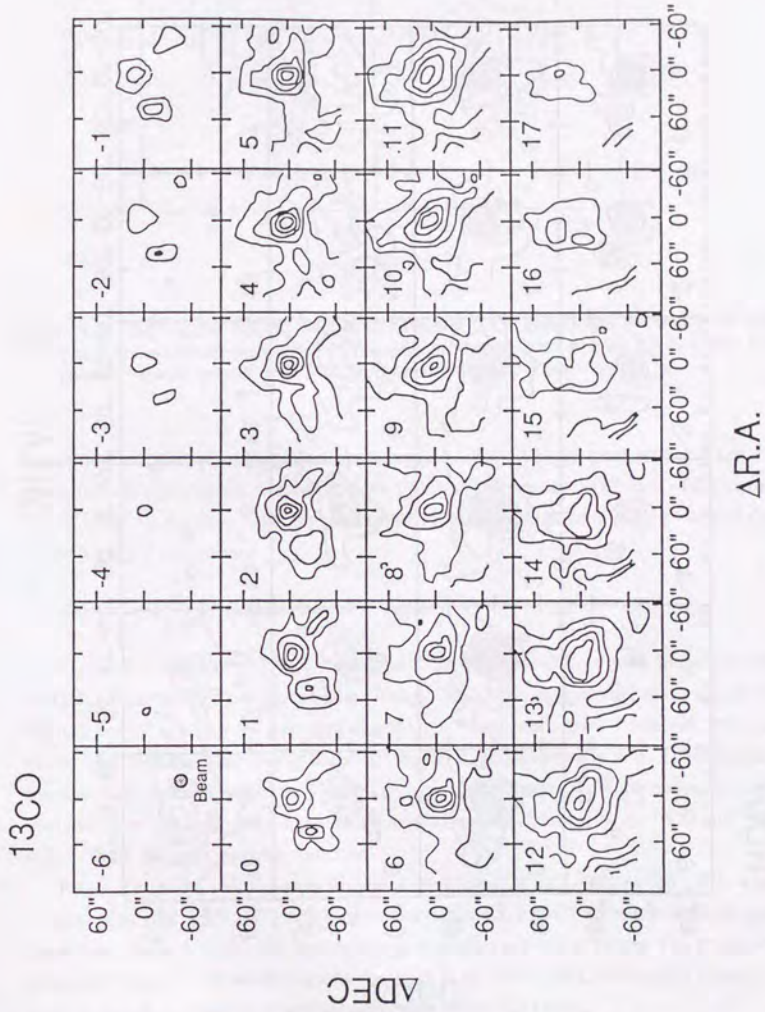

Figure 3-7: The Equivelocity Maps of ^{13}CO. The equivelocity maps of ^{13}CO averaged over 2 km s^{-1} centered on the velocities from -6 km s^{-1} to 17 km s^{-1} shown in the upper left corner of the panels. The contour interval is 1 K.

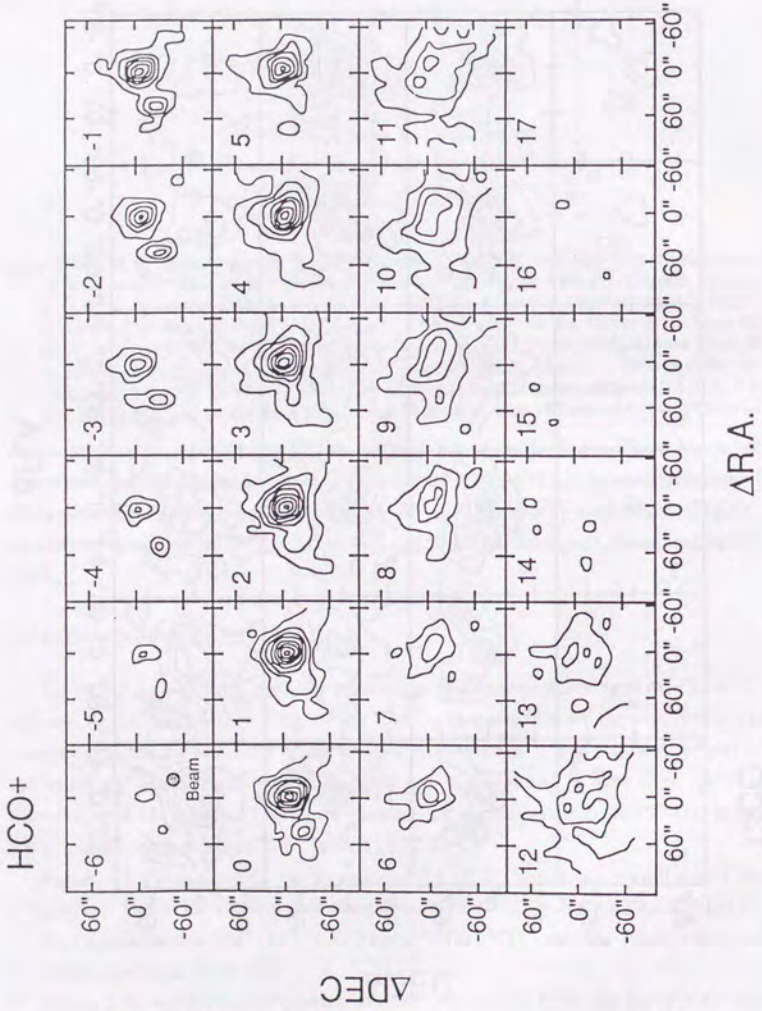

Figure 3-8: The Equivelocity Maps of HCO^+. The equivelocity maps of HCO^+ averaged over 2 km s^{-1} centered on the velocities from -6 km s^{-1} to 17 km s^{-1} shown in the upper left corner of the panels. The contour interval is 1 K.

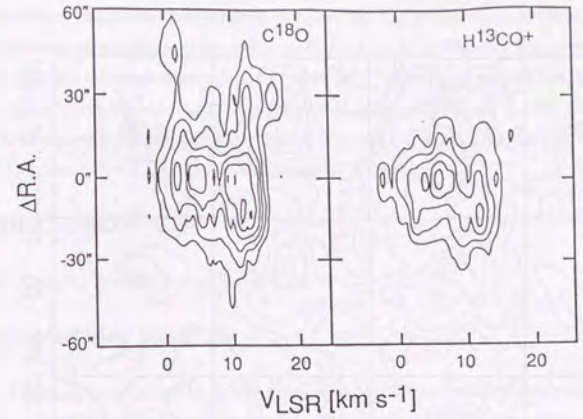

Figure 3-9: The Position Velocity Map of $C^{18}O$ and $H^{13}CO^+$ along Right Ascension. (Right) The position velocity map of $C^{18}O$. The contour interval is 0.2 K from 0.4 K. (Left) The position velocity map of $H^{13}CO^+$. The contour interval is 0.2 K from 0.4 K.

emissions, respectively, along the right ascension. For $C^{18}O$ the peak of the 4 km s^{-1} component is at the center, while that of the 12 km s^{-1} component is 8″ west of the center. For $H^{13}CO^+$, on the other hand, the peak of the 12 km s^{-1} component is at 12″ west of that of the 4 km s^{-1} component.

3.3. Results of $H^{13}CO^+$ Small Scale Observations

Figure 3-10 shows the $H^{13}CO^+$ integrated intensity and equivelocity maps with the 86 GHz interferometer continuum map (Welch 1990). The equivelocity maps are shown from -2 km s^{-1} to 15 km s^{-1} averaged over 2 km s^{-1} each and 1 km s^{-1} interval. This line is classified into the "shallow dip lines" in Chapter 2, and is optically thin. The integrated intensity map is concentrated on W49N. The elongations toward the north and east, which is not so clear due to the poor signal to noise ratio, are consistent with the ^{12}CO and ^{13}CO maps. These are seen as an arc structure.

From -2 to 6 km s^{-1} the emission peaks are located at (0″, -10″) or (15″, 0″), while another peak is at (-10″, 10″) which is seen at 0 and 4–6 km s^{-1}. There is a single peak from 7 to 8 km s^{-1} at (0″, 0″), and that peak is shifted to (-10″,0″) from 9 to 15 km s^{-1} except at 12 km s^{-1} at which velocity the peak is at (-10″, -10″). From 6 to 10 km s^{-1} there is a northern elongation which is also seen in the ^{12}CO maps.

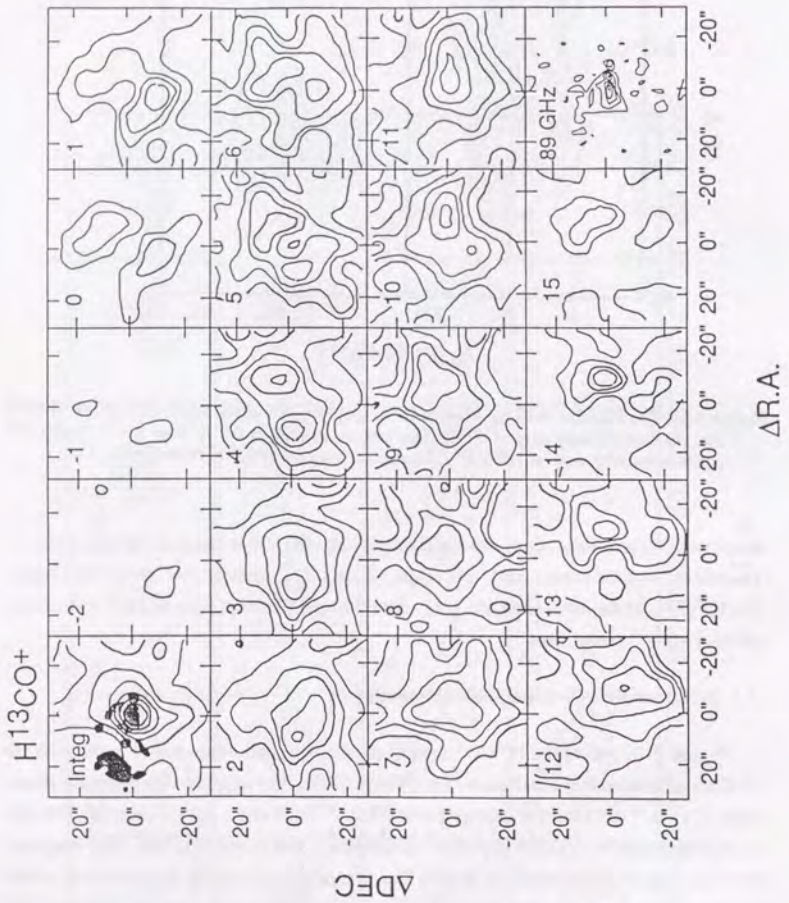

Figure 3-10: The Integrated Intensity and Equi-velocity Maps of $H^{13}CO^+$ (Upper Right) The integrated intensity map at the velocities from -10 km s^{-1} to 25 km s^{-1} superposed on 5 GHz continuum images (Dickel *et al.* 1990). The contour interval is 2 Kkm s^{-1}. The equivelocity maps of HCO^+ averaged over 2 km s^{-1} centered on the velocities from -2 km s^{-1} to 15 km s^{-1} shown in the upper left corner of the panels. The contour interval is 0.1 K from 0.1 K. (Lower left) the 89 GHz continuum image (Welch 1990) with interferometer.

There is a donut structure at 5 km s^{-1}. The donut apparently seems to be affected by the continuum emission. The line excitation temperature must be higher than the continuum brightness temperature in order for the emission to present. The continuum brightness temperature estimated to be $T_B \sim 1.04$ K in Chapter 2 is, however, lower than line excitation temperature of ~ 2 K of $H^{13}CO^+$ estimated around the continuum sources in Figure 3-10. Molecular gas does not exist at the component g. The H_2CO observations of Dickel and Goss (1990) show similar distribution to $H^{13}CO^+$ for the west and ($\sim$12km s^{-1}) and east ($\sim$4 km s^{-1}) condensations of W49N.

4. DISCUSSION

4.1. Rotating Necklace and W49A Core

4.1.1. Mass of the W49A Core

I derived the mass of the W49A core. The core was consists of two molecular clouda and has an interface region between the two. The column density of each cloud is derived from equation (A1.7.) in Appendix 1 with the kinetic temperature of 40 K, which is estimated from the peak temperature of the ^{12}CO emission. As well as this, Harvey, Campbell, and Hoffmann (1977) reported that the dust temperature is 45 K. The column densities of ^{13}CO for both components have the same values of $N(^{13}CO) = 3.6 \times 10^{17}$ cm^{-2}. The column density of ^{13}CO over the velocity range of 4 km s^{-1} an 12 km s^{-1} is $N(^{13}CO) = 7.1 \times 10^{17}$ cm^{-2}. When I use the abundance ratio of H_2 relative to ^{13}CO, $[H_2/^{13}CO] = 5 \times 10^5$ (Dickman 1978), the column density of hydrogen molecules is $N(H_2) = 3.5 \times 10^{23}$ cm^{-2}. Aassuming the abundance ratio of ^{12}C to ^{13}C to be the terrestrial ratio of 89, I may overestimate the mass by a factor of two because Langer and Penzias (1990) determined $^{12}C/^{13}C$ isotopic ratio of 49$\pm$6 toward W49A.

The mass of the core estimated from its size of 50″ (3.0 pc) is 3.4×10^4 $M_\odot$. This mass is comparable to that of (0.5-2.5) $\times 10^5$ $M_\odot$ derived from the $C^{32}S$ emission (MHH), that (4×10^4 $M_\odot$) of Schloerb, Snell and Schwarz (1987), and that (5×10^4 $M_\odot$) of Westbrook *et al.* (1976).

The simplest expression of the virial theorem ignoring such as magnetic fields and internal energy source leads to an expression for the total mass of a simple spherical system. Solomon *et al.* (1987) calculated the virial theorem masses of molecular clouds assuming only the self-gravity without external pressure, rotation, and gas thermal energy. The virial mass is estimated (Mac Laren, Richardson, and Wolendale 1988) as,

$$M_{vir} = k_1 \frac{\sigma_v^2 R}{G} M_\odot \qquad (3.1.)$$

or

$$M_{vir} = k_1 \frac{S\sigma_v^2}{G} M_\odot, \qquad (3.2.)$$

where σ_v is the full three-dimensional velocity dispersion averaged over the whole system, R and S are the cloud radius and size, respectively, and k_1 is a constant whose exact value depends on the form of the density distribution as a function of distance from the cloud center $\rho(r)$. For $\rho(r) \propto r^{-\alpha}$, where $\alpha<3$,

$$k_1 = \frac{5-2\alpha}{3-\alpha} \tag{3.3.}$$

Scoville *et al.* (1987) investigated 255 hot cloud cores associated with H II regions. Those cores show density index not very steep but is relatively flat as α=-1. The gravitational virial mass is defined as follows from a correlation between line-of-sight velocity dispersion and cloud size $\sigma_v = S^{0.5}$ km s^{-1}

$$M_{VT} = 2000\sigma_v^4 M_\odot \tag{3.4.}$$

Equation (3.4.) is derived from observational data with correlation between line width and size for molecular clouds; both dark clouds and giant molecular clouds (*e.g.*, Leung, Kutner, and Mead 1982; Myers 1983; Dame *et al.* 1986). This relation was first suggested by Larson (1981). W49A is consistent with this relation. If the velocity dispersion of each molecular cloud is σ_v ~3 km s^{-1}, then viral mass of each velocity component is $M_{VT} \sim 1.6 \times 10^4 M_\odot$. On the other hand, one component model, which contradicts to the correlation between the size and velocity, has $M_{VT} \sim 8 \times 10^6 M_\odot$. Equation (3.4.) is not adopted to the core of burst star formation.

The core of burst star formation has similar density index of α=-2 in W49A (Chapter 2) and α=-2 or -2.5 for Sgr B2 (Lis and Goldsmith 1989). If I assume a simple cloud for W49A the value of k_1 is 1, then r=1.5 pc and ΔV=8 km s^{-1}. The virial mass is derived $M = 1.2 \times 10^4 M_\odot$. This value is consistent with the previously estimated values (MHH, Chapter 4 and other researches) and the calculated values from equation (3.4.) when I assume that W49A consists of two clouds. Large velocity dispersion of the clouds in W49A and Sgr B2 cores may not be influenced by nongravitational force such as energy injection from OB stars as Maloney (1990) suggested.

4.1.2. Supporting Mechanism

I obtained the mass of 3.4×10^4 $M_\odot$. The mass is so large that the core is dynamically unstable if there is no supporting mechanism, as many authors suggested. The cloud core will hence collapse in the free fall time scale of 10^5 *yr* unless some supporting mechanism such as the magnetic field (MHH), rotation (Welch *et al.* 1987), turbulencem or stellar wind (Turner 1984) works.

The magnetic field is an attractive mechanism of supporting molecular cloud cores. Myers and Goodman (1988) discussed magnetic support and ambipolar diffusion of

molecular cloud cores. MHH suggested that the core of W49A could be supportd if there is the magnetic field of order 200 μG. The field strength of ~3–5 mG was estimated from Zeeman splitting measurements of OH maser lines toward W49N (Johnston and Hansen 1982; Gaume and Mutel 1987). From H_2O masers the field strength of ~30–50 mG was also derived (Fiebig and Güsten 1989). The magnetic field strength is proportional to the square of gas density if gas is frozen in the field. OH maser emitting regions have a typical density of ~ 10^8 cm^{-3} and H_2O maser regions have ~ 10^{10} cm^{-3}, while the density of molecular clouds is ~ 10^{3-4} cm^{-3}. Myers and Goodman (1988) suggested that massive cores are more diverse than low-mass cores in their size, density, velocity dispersion and temperature and need much more magnetic support than thermal one. The magnetic field of a massive core is under equilibrium if the field strength is ~10 times greater than a low-mass core or an extended cloud. Magnetic field direction was studied using polarization of far-infrared (100 μm) radiation (Novak *et al.* 1989) with negative detection toward W49A with an upper limit of 1.1%. On the other hand, Tamura *et al.* (1994) recently detected the polarization of ~3% with a 19″ beam.

Welch *et al.* (1987) suggested that the "necklace" is supported by rotation as well as magnetic field. The diameter and inclination of the "necklace" are 2 pc and 65°, respectively. The direction and shape of the norteast elongation in ^{13}CO and HCO$^+$ maps are consistent with those of "necklace."

In Figure 3-9, a velocity gradient exists from 0″ to 30″ in both line emission. The direction of velocity gradient is consistent with the "necklace." The velocity gradients of those molecules are different; 21.3 km s^{-1}pc^{-1} in the C^{18}O line and 16.5 km s^{-1}pc^{-1} in the H^{13}CO$^+$ line, respectively. These values are larger than that of "necklace" (13 km s^{-1}pc^{-1}) (Welch *et al.* 1987), and the two velocity components seem to be gravitationally bound.

Another possible supporting mechanism is supersonic turbulence. Supersonic turbulence observed in molecular clouds is, however, not capable of sustaining the cloud against gravitational collapse. In the absence of input of turbulent energy, supersonic turbulence can not support a cloud against gravitational collapse over a time scale equal to that of the free fall time within a factor of order unity. Scalo and Pumphrey (1982), however, simulated the dispersion of supersonic turbulent motions of N-body systems of interacting gas fragments, suggesting that unreplenished supersonic turbulence might support a cloud up to five times longer than the free fall time.

Stellar Winds and high-velocity molecular outflows have a possibility of supporting molecular clouds. Estimating the energy of high velocity outflows, Turner (1984) suggested that their energies are not sufficient to support a whole giant molecular cloud or a massive core.

4.2. Collapse of Massive Core

In the previous subsection, I discussed various possibilities of sustaining the W49A core stable, and found it very difficult, as was mentioned by MHH. On the other hand, Welch *et al.* (1987) suggested evidence for collapse of W49A by interpreting the $HCO^+(J = 1 - 0)$ spectra obtained by a single dish and an interferometer. The spectra toward W49A showed emission and absorption over the velocity range from -10 to 30 km s^{-1} associated with the W49A with the dips at ~8 km s^{-1} and ~17km s^{-1}. The spectrum obtained with the single dish telescope have two peaks at 4 km s^{-1} and 12km s^{-1} as suggested by MHH, while those with the interferometer have absorption over the range from 11 km s^{-1} to 21km s^{-1}. The difference between the emission and absorption occurs due to the difference in brightness temperature between line and continuum, as the line brightness temperature averaged over a small beam often becomes less than the continuum brightness temperature. The continuum brightness temperature measured with the interferometer is much higher because of the smaller beam dilution. Welch *et al.* (1987) also discussed that the redshifted part is located in front of the the continuum source and the blueshifted part is located on the far side of it. Furthermore Welch *et al.* (1987) suggested that the absorption is not just in a small localized cloud in front of the continuum source but extends over the entire "necklace."

Welch *et al.* (1987) did not, however, discuss about the 8 km s^{-1} dip. Snell and Loren (1977) calculated self-reversed line profiles from collapsing clouds, comparing ^{12}CO and ^{13}CO line spectra. Recently Dickel and Auer (1994) made radiative transfer calculations based on the large velocity gradient approximation with a velocity law of $v \propto r^{-0.5}$. While their calculated spectra seemed to be consistent with observational results, they assumed a single cloud.

They assumed the absorption at 8 km s^{-1} as caused by envelope gas from comparison between temperature of the core and the envelope. Because the collapsing velocity of the envelope is ~ 1 km s^{-1}, the 17 km s^{-1} absorption feature is caused by the gas near massive core. As mentioned in the previous subsection, the massive core is under dynamical collapse if there is no supporting mechanism. Inside-out collapse is also assumed to be taking place so that the infall velocity of the core is faster than the envelope. The envelope has the collapsing velocity of 0-1 km s^{-1} and the core is assumed to have the collapsing velocity of ~10km s^{-1}, which are consistent with discussion of Jackson and Kraemer (1994).

4.3. Massive Star Formation in W49A Core

Observations of ultracompact H II regions in W49N as well as in other giant moelcular clouds such as in Sgr B2(*e.g.*, Benson and Johnson 1984), W51A(*e.g.*, Jaffe *et al.* 1989), W31A (*e.g.*, Woodward *et al.* 1984), and G10.4-0.3 (*e.g.*, Ho and Haschick 1981) have revealed multiple structures, which correspond to OB stars in these regions, with size

scales and separation distances of $\lesssim$ 0.1 pc and differences in formation time scales of only $\lesssim$ a few tens of thousands of years. It is not clear how these OB star formations are so synchronized unless there were some triggers to cause such burst of star formation. MHH suggested that two velocity components collided with each other so that the entire molecular cloud complex was compressed and the unstable massive molecular cloud core was formed in W49A.

There were several numerical simulations of cloud collisions. The calculations by Lattanzio *et al.* (1985) and Lattanzio and Henriksen (1988) were three-dimensional numerical simulation of isothermal interstellar clouds in the absence of magnetic fields. Some of head-on and off-center collisions showed necessary conditions for the gravitational instability to take place in the substantial fraction of molecular clouds that had the initial conditions either marginally stable or unstable. Habe and Ohta (1992) presented axisymmetric hydrodynamic calculation of supersonic head-on collisions between non-identical cloud, finding that even if a cloud has a mass well below the Jeans mass it becomes gravitationall unstable through collisions with non-identical partners.

Keto and Lattanzio (1989) reported that collisions among clouds with uniform density and temperature make high density and high temperature regions by both head-on and off-center collisions. Through head-on collisions spherical cores are formed with their velocity having the mean value of colliding clouds. When off-center collisions take place, S-shaped dense regions are formed and two dense peaks seemed to appear. Keto and Lattanzio (1989) suggested that cloud collisions can induce fragmentation with collapse and that in some cases fragments grow up to be proto-stellar cores .

Klein *et al.* (1983) proposed aother triggering mechanism of star formation called radiation-driven implosions of embedded clumps, in which previously existing multiple sources (OB stars) cause next generation stars to be formed. In this mechanism low-mass cut off can be explained by verture of the failure of smaller cores to survive against evaporation. Two-dimensional radiation-hydrodynamical numerical calculations (Klein *et al.* 1983; 1986) improved upon the analytic solutions of Elmegreen and Lada (1977), which showed that the radiation-driven shock waves formed from first generation OB stars can efficiently compress molecular clouds to form cores and second generation stars on a time scale of $\sim 10^6$ *yr*.

Ho, Klein, and Haschick (1986) applied this idea to G10.6-0.4 and W33 to explain a burst of star formation. Coexistence of objects with first and second generations made the situation complicated, which was different from the case of the "necklace" of W49A. Where are first generation OB stars? Those may have already been supernovae, which Dieter, Welch, and Wright (1979) suggested the possibilities of their existence in W49A, while there is no evidence. This radiation-driven model has some difficulties to explain star formation in W49A. Turner (1984) suggested that bright rimmed clouds contain no

massive stars. Wooten *et al.* (1983) showed that there is no evidence for compression-induced massive star formation in bright rimmed clouds although their column densities typically have peaks within 1 pc or less from the rims. For example Hayashi *et al.* (1987) observed bipolar flow in the S140 cloud, which is located at ~0.3 pc from the bright-rim. While the S140 cloud includes several intermediate mass protostars, there is no massive protostars.

On the other hand, Sugitani *et al.* (1989) showed that in several bright-rimed globules continued radiation-driven implosions may have caused the formation of stars with more massive than in isolate dark globules. It seems, however, difficult to form a number of massive stars, especially OB stars. A large amount of originally contained mass in a globule can be lost through this proces, because the gas is ionized by first generation OB stars. Ionized, ablated gas will recombine at the region long distance from W49A.

Trigger by radiation driven implosions will induce formation of low and intermediate mass stars but no massive stars. Low and intermediate mass stars formed in W49A may be partially affected by this mechanism. There is, however, no evidence because it is difficult to detect low luminosity stars due to the presence of many massive stars.

Is it true that the clusters of ultracompact H II regions in W49A formed synchrously by some mechanism? Age of ultracompact H II regions are derived from radius of the Strömgen sphere. In Appendix 2, I determined the age of ultracompact H II regions based on the calculations by Wood and Churchwell (1989b). For an ultracompact H II region it takes $\sim 1.6 \times 10^6 yr$ to reach pressure equilibrium with $\sim$ 1.3 pc in diameter within the lifetime of a O6 star. If the inside-out collapse takes place the age may be underestimated. The component g is surrounded by a massive dust cocoon. If outer layers of the dusty cocoon surrounding an embedded O star are collapsing (a remnant of the star formation or another star formation), as Reid *et al.* (1980) and Garay, Reid, and Moran (1985) have advanced to explain their observations of OH maser radial velocities seen in some ultracompact H II regions, then infalling gas would slow the expansion of ionized gas. Welch and Marr (1987) have suggested that the observed velocity shift between the ionized and molecular gas may be an optical depth effect. Recombination line observations should be made at higher frequency (where the H II region is more optically thin) to obtain a better estimate of the velocity of ionized gas. There is, however, no velocity change of recombination line velocities of various quantum numbers (Mufson and Liszt 1977; MHH).

Numerical simulation presented the probability of formation of massive cores with several fragments, from which stars will be formed. Theoretical arguments suggested the probability of infall gas toward each fragment (Keto, Lattanzio, and Monaghan 1991). Keto, Lattanzio, and Monaghan (1991) assumed that each fragment has the mass of $\sim 10^3 M_\odot$ and the radius of 0.6-0.8 pc. In this region the density is assumed to be $\sim 10^5 cm^{-3}$ and the mass of this fragment is $5 \times 10^3 M_\odot$. Accretion for $10^5 yr$ would form this fragment

with $5 \times 10^3 M_\odot$. These massive fragments may form massive stars as discussed in Chapter 5.

5. CONCLUSIONS

I have reported two-dimensional observations in the ^{12}CO, ^{13}CO, HCO^+, and $H^{13}CO^+$ lines of W49A, which revealed the structure of the massive core. Similarity between the ^{12}CO line and 53 μm continuum emission maps is a natural consequence if the integrated ^{12}CO peak intensity reflects the gas temperature distribution. Distribution of the ^{13}CO emission is also similar to that of the 53 μm emission. The emission of HCO^+ line is assumed to be arisen from high density region, and is concentrated in the 'core.' Large mass is packed in the core as suggested from the results of $C^{32}S$ emission (MHH). On the other hand, the peak of HCN is slightly different from the ^{13}CO and HCO^+.

The mass of this massive core of 50″ in diameter is 3.4×10^4 $M_\odot$. For the direction of the "necklace" (Dreher *et al.* 1984) with a diameter of 2 pc and inclination of 65°, there is a northeast elongation in ^{13}CO and HCO^+ maps.

Both ^{13}CO and HCO^+ profiles have emission and absorption over the range from -10 to 30 km s^{-1} coming from the W49A complex and have dips at ~8 km s^{-1} and ~17 km s^{-1}. If there is no supporting mechanism such as magnetic field, the massive core will collapse with its velocity being $\sim$ 1 km s^{-1} in the envelope reaching to be ~10 km s^{-1} near the center.

Chapter 4

DUST EMISSION FROM W49A

1. DUST EMISSION AND MASSIVE CORE

In the previous chapters, we have argued that W49A is a region of a localized burst of star formation containing many ultracompact H II regions in a massive molecular cloud core. In this chapter, I present submillimeter continuum observation of the W49A cloud core with high angular resolution, and discuss distribution of dust and neutral gas in the region of very active massive star formation. Submillimeter continuum emission from dust is a very effective probe of dense condensations of interstellar matter.

Westbrook *et al.* (1976) first presented a map of 1 mm thermal emission from dust grains with 1′ resolution. Their results suggested that the 1 mm flux density peak coincides with the position of masers and infrared sources of W49N, while W49S does not have a dominant 1 mm peak. They concluded the intense emission seen at 1 mm from W49N suffers higher visual extinction than W49S, and W49N must be embedded in an unusually thick dust cloud. They estimated the mass of W49A molecular cloud core as 5×10^4 $M_\odot$, which is comparable to the mass derived by MHH and in this thesis.

Here I present observations of 450 μm and 1,100 μm continuum emission with high resolution. Spectral indices are also derived using shorter wavelength data. I show morphology of dust cloud of W49N, deriving its mass, and discussing dust properties in the massive core.

Because of the presence of luminous compact H II region in the core of W49N, continuum flux even at submillimeter or millimeter wavelengths is cintaminated by the free-free emission, so that we need to separate the dust emission away from the free- free emission. Sievers *et al.* (1991) corrected for the free-free emission from their 3,300 μm and 870 μm maps, and decomposed the dust emission spectrum from 2,000 μm to 10 μm into contributions from cold, warm, and hot dust. Schloerb, Snell and Schwarz (1987) presented the 1,300 μm continuum emission and the $C^{18}O$ ($J = 2 - 1$) spectral line emission with 25 ″ beam. They found a correlation between dust and gas distribution assuming that free-free emission should contaminate uniformly. On the other hand, Gordon and Jewell (1987) presented maps at the 1,300 μm with 30″ beam with narrow-band receiver to subtract effects of submillimeter emission lines.

II. Observation

2. SUBMILLIMETER CONTINUUM OBSERVATIONS

Observations were made on 1988 July 9–13 using the James Creak Maxwell Telescope (JCMT). We used a bolometer system UKT 14. The beam patterns were checked by

observations of Uranus and Saturn. The aperture was set to 47.3 mm and 65 mm at 450 μm and 1,100 μm, respectively, which corresponded to a beamwidth (HPBW) of 17″ and 19″. The map at 450 μm was made by making a raster scan along the azimuth with a 7″.5 grid spacing in an area of 90″ × 90″. The 1,100 μmmap was made with a raster scan along the elevation with a 12 ″ grid spacing in an area of 120″ × 120″.

The center position of all the observations was taken to be $\alpha(1950) = 19^h07^m49^s.8$, $\delta(1950) = 9°01'15''.5$, which corresponds to the component g of the thermal continuum emission by Dreher *et al.* (1984). The signal for each position was the difference obtained by chopping between the source and a reference position offset by 2′ east and west. Similar raster maps of 3C 273 and Uranus for pointing and flux calibration were interspersed with observations of the source. The maximum pointing shift between two sets of observations was a half of the beamwidths. The flux density scale was established by using the standard JCMT calibration program that assumes the brightness temperatures of Uranus to be 71K and 92K for the 450 μm and 1,100 μm bands, respectively. These corresponded to 45.9 Jy/beam and 209.2 Jy/beam, respectively, and are consistent with the measurement by Ulich, Dickel, and de Pater (1984) and Lowenstein *et al.* (1977). Since the entire system response was calibrated by the Uranus measurements, we have no independent determination of the antenna efficiency.

3. RESULTS OF SUBMILLIMETER CONTINUUM EMISSION

3.1. 450 μm and 1,100 μm Distribution

Figure 4-1 shows the 450 μm and 1,100 μm maps. Gordon *et al.* (1986) and Gordon and Jewell (1987) mapped W49A at 3,300 μm and 1,300 μm. Ward-Thompson and Robson (1990) obtained infrared maps from *IRAS* calibrated raw data with low resolution. Sievers *et al.* (1991) mapped W49N with a beamwidth of 30″ at 870 μm and 1,300 μm. Our results were consistent with these observations but more fine structures of dust cloud was obtained with our higher resolution. The 450 μm and 1,100 μm maps includes the entire "necklace" region. The peak flux density was found toward the component g and are 510 Jy/beam and 30.8 Jy/beam at 450μm and 1,100 μm, respectively, which have uncertainties of 50 % and 11 %, respectively.

The 450 μm map resembles the ^{13}CO map presented in Chapter 3. The source extent is 30″ × 30″ ($\alpha \times \delta$) at the half maximum level. The 450 μm map has two elongations; one is toward southeast from the component g, and the other is from northeast to southwest. The southeast elongation seems to be connected with another gas condensation (MHH and Chapter 3). The northeast-to-southwest elongation through the component g seems to be related with the "necklace."

The 1,100 μm map resembles the $C^{32}S$ map (MHH) and the 1 mm continuum emission (Westbrook *et al.* 1976) rather than the ^{13}CO map. The source extent is 40″ × 30″

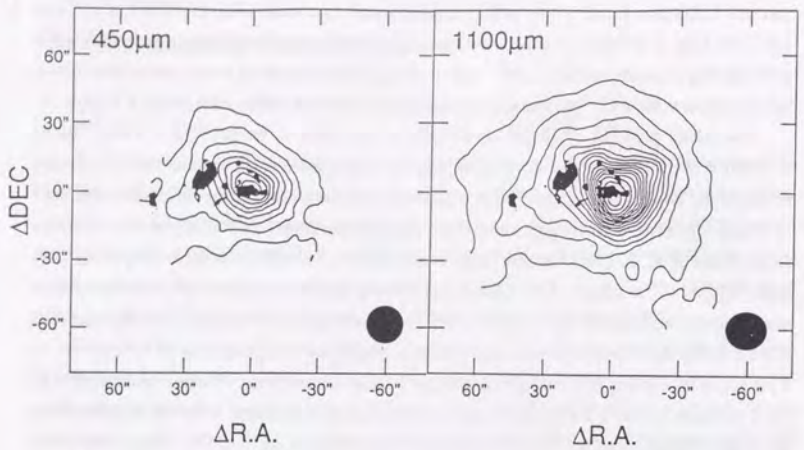

Figure 4-1: The 450 μm and 1,100 μm Continuum Maps. (left) Contour map of the 450 μm emission from W49A superposed on 5 GHz continuum images (Dickel *et al.* 1990). Contour interval is 50 Jy/beam. (right) Contour map of the 1,100 μm emission from W49A superposed on 5 GHz continuum images (Dickel *et al.* 1990). Contour interval is 2 Jy/beam. Beamwidthes are indicated at lower right corner of the panel, respectively.

($\alpha\times\ \delta$) at the half maximum level. The 1,100 μm map have three elongations; one is toward southeast as like the 450 μm map, another is to the northwest from the component g, the other is from northeast to southwest as in the 450 μm. Another faint elongation toward north from the component g is seen. The north elongation seems to be the same feature as was seen in the integrated intensity maps of ^{12}CO, ^{13}CO, HCO$^+$. The southeast and northeast-to-southwest elongation over the component g seems to be related with the corresponding feature of the 450 μm map.

Figure 4-2 shows a flux ratio map of the two wavelengths. The ratio shows a similar value of ~10–15 around W49N. Theis value is a factor of 2 lower than the ratio of 4,700 Jy at 400 μm (Gordon 1987) and 185 Jy at 1,100 μm (Ward-Thompson and Robson 1990). The map center has maximum ratio. The northeast part shows higher values of ratio than the southwest part does.

We can calculate the spectral index α based on its usual definition,

$$\alpha(450/1,100) = log\left(\frac{S_{450\mu m}}{S_{1,100\mu m}}\right)/log\left(\frac{1,100}{450}\right), \qquad (4.1.)$$

where $S_{450\mu m}$ and $S_{1,100\mu m}$ are the flux density at 450μm and 1,100μm, respectively. The spectral index at the continuum peak is α=3.14.

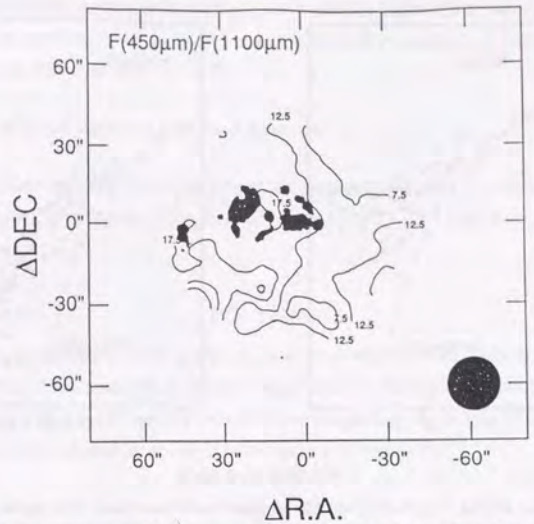

Figure 4-2: The Flux Ratio Map between 450 μm and 1,100 μm. The flux ratio map between 450 μm and 1,100 μm superposed on 5 GHz continuum images (Dickel *et al.* 1990).

3.2. Radial Distribution of 450 μm and 1,100 μm

The radial distributions of the 450 μm and 1,100 μm continuum emissions are compared with the gas distribution shown in Chapter 2. Figure 4-3 shows the radial distributions. For $\lesssim$30″, the fitted powers are -1.12 and -1.12 for the 450μm and 1,100μm, respectively. It is difficult to determine the power law index of 450 μm for $\gtrsim$30″ because of the large scattering of data points. On the ohter hand, the power law index of 1,100 μm is easily determined to be -2.04. The diffrence in the power law index between $\lesssim$30″ and $\gtrsim$30″ corespond to the presence of the massive core (MHH; Chapter 3) and its envelope. The total flux from W49N is estimated as,

$$F_\nu = F_\nu(center) + \int F_\nu(r)dr. \qquad (4.2.)$$

The fluxes toward the center are 510 Jy/beam and 30.8 Jy at 450 μm and 1,100 μm, respectively. The total flux at 450 μm is 1360 Jy within the beam toward the center and is 2260 Jy in the area $\lesssim$30″ and $\gtrsim$30″. The corresponding total fluxes at 1,100μm are 134 Jy and 239 Jy, respectively. These values at 450 μm are lower than 4,700 Jy measured at 400 μm (Gordon 1987) but are consistent with 185 Jy measured at 1,100 μm (Ward-Thompson and Robson 1990).

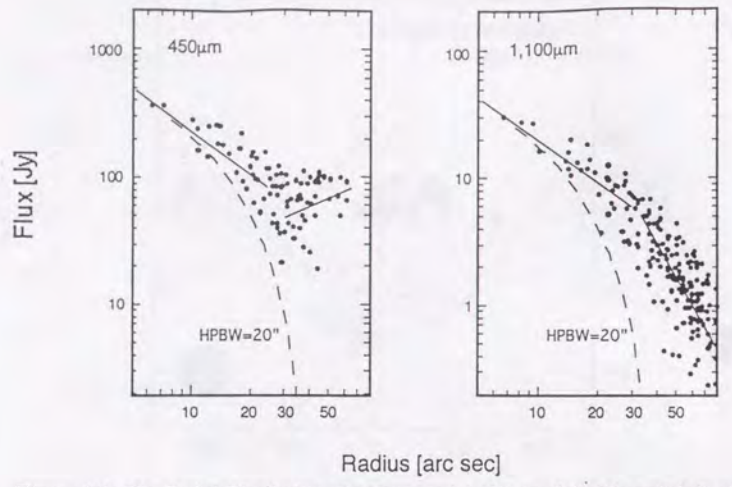

Figure 4-3: The Radial Distribution of 450 μm and 1,100 μm (left) The radial distribution of 450 μm. (right) The radial distribution of 1,100 μm. Filled circles indicate observed points.

4. DISCUSSION

4.1. Morphology of Dust Cloud and Dust Emission

Both the 450 μm and 1,100 μm maps present dust distribution. The 1,100 μm map presents the column density of dust emission because that resemble the CS integrated intensity map (MHH), while the 450 μm map rather traces warmer dust, so that the "necklace" is seen in this wavelength. The density distribution is calculated in Chapter 2. If the cloud radius R is estimated as 60″, then local densities can be integrated along lines of sight through the cloud envelope to give the column densities N(p) as below,

$$N(p) = (2\rho_0 r^{\gamma}) m_{H_2}{}^{-1} \int_0^{ZR} (z^2 + p^2)^{-\frac{1}{2}} dz \qquad (cm^{-2}) \tag{4.3.}$$

where $ZR = (r^2 - p^2)^{-\frac{1}{2}}$, Z is the distance along the line of sight measured from the cloud center, p is the impact parameter from the cloud center and ρ_0 and r_0 are the mass density and radius, respectively.

The dust distribution in the region within 30″ follows a power law with index 1, i.e., $F_\nu \propto r^{-1}$, and the outer envelope follows a power law with index 2. The radial distribution of the flux density is proportional to r^{-1}, $F_\nu \propto r^{-1}$, within 30″. The column density of hydrogen molecule is estimated $N(H_2) \propto r^{-1}$, and the radial distribution of the number density is proportional to r^{-2}, $n(H_2) \propto r^{-2}$. The outer envelope, however, has steeper index than the inside of 30″.

4.2. Mass of W49A Deduced from Dust Emission

To estimate the mass of the core from the dust emission, the flux density F_ν is fitted with the Planck function $B_\nu(T) = 2h\nu^3/c^2[exp(h\nu/kT) - 1]^{-1}$ only at its the blue side as follows,

$$F_\nu = \Omega B_\nu(T), \tag{4.4.}$$

where Ω is an effective solid angle of the dust cloud, T is the dust temperature, ν is the frequency. We assumed in these fittings that the emission is optically thick at all frequencies. Red sides of spectra are not, however, abided. To fit the red side as well, the optical depth is included in equation (4.4.) as (*e.g.*, Gordon 1987),

$$F_\nu = \Omega B_\nu(T)(1 - e^{-\tau}), \tag{4.5.}$$

where the optical depth τ depended on frequency, which is modeled by

$$\tau = (\nu/\nu_c)^{\beta}, \tag{4.6.}$$

where τ_c is the frequency at which τ=1. This parameter of the W49A massive core is estimated as 150 μm (*e.g.*, Gordon 1987; Ward-Thompson and Robson 1990; Sievers *et al.* 1991).

The mass of the dust measured at the submillimeter range can be calculated by the following equation (Hildebrand 1983).

$$M_d = \frac{4a\rho D^2 F_\nu}{3B_\nu(T)Q_{125}} (\lambda/125)^{\beta}, \tag{4.7.}$$

where a is the mean grain radius, ρ is the density of dust grain material, D is the distance to the cloud and Q_{125} is the grain emissivity at 125 μm, λ is the observing wavelength in micron. The frequency dependence of the emissivity is expressed by β=α–2∼ 1.8 ± 0.2 (Gordon 1987; Ward-Thompson and Robson 1990). We, however, obtained a smaller value of β=1.1 than that of Gordon (1987). Using typical values for ρ=3 g cm^{-3}, a=0.1 μm, Q_{125} is estimated as 3/4000 (Hildebrand 1983) and T_d =50 K (Westbrook *et al.* 1976; Ericskson and Tokunaga 1980; Gordon 1987). From these parameters the dust mass of W49N is calculated and listed in Table 4-1.

The slight difference between the 450 μm and 1,100 μm map is assumed to be due to variation of free-free emission from place to place or due to difference in dust

temperature, because the millimeter-wave and infrared spectra are both affected by the free-free emission. Sievers *et al.* (1991) indicated that ~20 % of the continuum is contaminated by the free-free emission at 1,100μm, while the contamination is negligible at 450 μm. The slight difference between the 450 μm and 1,100 μm maps is assumed to be caused by contamination by the free-free emission. Schlorb, Snell and Schwarz (1987) also suggested that their 1,300 μm continuum map has contaminated by the free-free emission by one-forth of the flux density and the free-free emission was spread over the region comparable in size to the dust emission. As the flux density ratio is almost constant in Figure 4-2, the free-free emission may distribute rather uniformly. If 20% of the flux density at 1,100μm is free-free emission, the spectral index increases as α=3.4 and the dust emissivity becomes β=1.4. The total mass is estimated $5\times10^4 - 1.7\times10^5 M_\odot$ for $\lesssim$30″ in Table 4-1. These masses are consistent with those estimated from molecular lines (*e.g.*, MHH and Chapter 3) and other results (*e.g.*, Westbrook *et al.* 1977; Gordon 1987; Schloerb, Snell, and Schwartz 1987).

4.3. Dust Properties in Massive Core

The spectral index map between 450 μm and 1,100 μm is shown in Figure 4-4. It has a maximum at the center position.

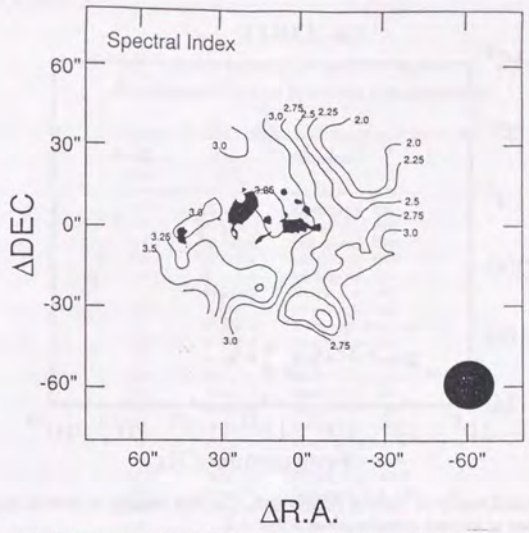

Figure 4-4: The Spectral Index Map between 450 μm and 1,100 μm. The spectral index map between 450 μm and 1,100 μm superposed on 5 GHz continuum images (Dickel *et al.* 1990). Averaged beamwidth is indicated at lower right corner of the panel.

TABLE IV-1

TABLE 4-1

Calculated Dust and Total Mass

Region	wave length [μm]	Flux [Jy]	β	Dust Mass [$M_\odot$]	Total Mass [$M_\odot$]
<30″	450	1360	1.1	3.2×10^2	3.2×10^4
			1.4	4.8×10^2	4.8×10^4
	1,100	134	1.1	8.7×10^2	8.7×10^4
			1.4	1.7×10^3	1.7×10^5
<60″	450	2560	1.1	5.5×10^2	5.5×10^4
			1.4	8.0×10^2	8.0×10^4
	1,100	239	1.1	1.5×10^3	1.5×10^5
			1.4	3.0×10^3	3.0×10^5

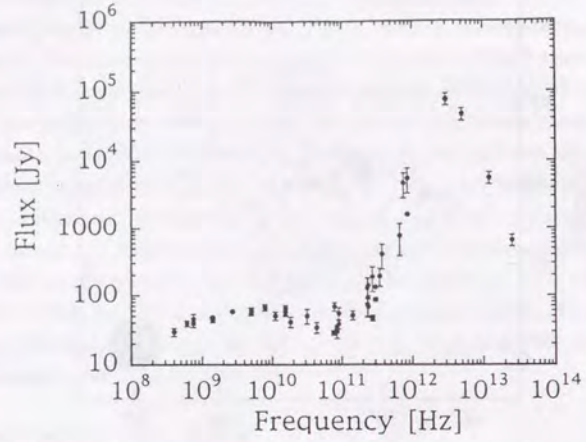

Figure 4-5: The Flux Density of Various Wavelength. The flux density of W49A is plotted by many researches at various wavelength in Table 4-2.

The flux densities at various frequencies are listed in Table 4-2, and are plotted in Figure 4-5. The free-free emission is dominated at the frequencies from 2 GHz to 100 GHz, where the spectrum is flat. The dust emission becomes dominated above 100 GHz. Erickson and Tokunaga (1980) investigated the spectrum of W49N in the wavelength range of 30μm to 150 μm. The spectrum of W49N within a 25″ beam is fitted by the Planck function of 52 K. Other researches also derived a single temperature spectral component (Gordon 1987; 1988; Ward-Thompson and Robson 1990). They presented that the dust emission is fitted by a greybody with a temperature of 50 K with the submillimeter spectral index of $\beta = 1.8 \pm 0.2$. Sievers *et al.* (1991), however, concluded that the spectrum in the range from 12μm to 3,300μm has three components; the cold dust component with its temperature of 20 K with a diameter of 8.2 pc, the warm component with its temperature of 50 K with a diameter of 2.2 pc, and the hot component with its temperature of 140 K with a diameter of 0.3 pc.

TABLE IV-2

TABLE 4-2

Continuum Flux of Previous Observations

Frequency [GHz]	Flux [Jy]	Refferences
0.4	29.4±4.0	Mezger *et al.* 1967
0.6	39.0±4.0	Mezger *et al.* 1967
0.8	45.0±8.0	Pauliny *et al.* 1966
0.8	40.0±6.0	Mezger *et al.* 1967
1.4	47.2±1.8	Pauliny *et al.* 1966
1.4	44.0±4.0	Mezger *et al.* 1967
2.7	58.0	Mezger *et al.* 1967
5.0	57.5±7.0	Mezger and Henderson 1967
5.0	59.8±6.0	Mezger *et al.* 1967
7.8	66.0±7.0	Burk and Wilson 1967
11	50.0±7.0	Hobbs and Johnston 1971
15	56.0±7.0	Mezger *et al.* 1967
15	64.0±7.0	Mezger *et al.* 1967
15	58.0±7.0	Mezger *et al.* 1967
18	41.0±7.0	Hobbs and Johnston 1971
32	50.0±12.0	Hobbs and Johnston 1971
43	34.1±6.0	Akabane *et al.* 1989
76	28.4±2.5	Malkamäki *et al.* 1979
78	68.0±10	Efanov *et al.* 1975
84	33	Gordon *et al.* 1986
85	30.0±6.5	Brown and Broderick 1973
90	54±11	Riegel and Epstein 1968
90	38±5.7	Salter *et al.* 1989
142	51±7.7	Salter *et al.* 1989
230	127±50.8	Schloerb *et al.* 1989
232	70±21	Gordon 1987
236	67±20	Sievers *et al.* 1991
236	138±41	Sievers *et al.* 1991
273	185±74	Mezger *et al.* 1990
273	46.1±4.6	Chapter 4
300	131	Chini *et al.* 1984
300	86.0±5.0	Westbrook *et al.* 1976
347	190±57.0	Sievers *et al.* 1991
375	403±161	Ward-Thompson and Robson 1990
667	764±382	chapter IV
750	4,700±1,880	Gordon 1987
857	5,500±2,200	Ward-Thompson and Robson 1990
857	1,600	Rieke *et al.* 1973
3,000	76,000	Hoffmann *et al.* 1971
3,000	77,400±15,480	Sievers *et al.* 1991
5,000	46,840±9,370	Sievers *et al.* 1991
12,000	5,624±1,125	Sievers *et al.* 1991
25,000	656±131	Sievers *et al.* 1991

Hot dust with temperature of140 K is located toward the compact sources in W49N (Sievers *et al.* 1991). Gas-grain collisions (*e.g.*, Burke and Hollenbach 1983) are dominant in the dense massive core. Dust grains absorb starlight and thereby heated up to the temperature of $\sim 30 - 100$ K. Cooler gas particles collide with warm grains to be heated conductively. The dust temperature is not, however, always, higher than the gas

temperature. When gas is directly heated by gravitational collapse as Schwarz (1982) suggested, gas temperature may become higher than the dust temperature, and the dust is heated by gas. When collapse takes place in a free fall time, the dust temperature, T_D, is calculated as below (Goodrich and Kwan 1974),

$$T_D = T_g \left[1 + t_r \left(\frac{dlnE}{dt} - \frac{2V}{R} \right) \right] = T_g \left[1 + \frac{t_r}{t_{ff}} \left(\frac{t_{ff}}{t_c} - 2 \right) \right], \qquad (4.8.)$$

where t_r is the gas-dust relaxation time, t_{ff} is the free fall time, and t_c is the molecular line cooling time. When t_{ff}/t_c approximately scales as R/V and cooling by the CO line is dominant, the dust temperature, T_D, is assumed to be $T_D \sim 2T_g - 10$ K for the hydrogen density of $n_{H_2} \sim 4 \times 10^4$ cm^{-3} and 10 K$< T_g <$ 30 K. The dust temperature is calculated to be 40 K (Linke and Goldsmith 1977), which is not sufficient to explain the warm dust. On the other hand, the gas temperature 40 K is estimated from ^{12}CO line emission in Chapter 2.

There is another suggestion about the hot dust emission. Hot dust emission may not arise from normal grains but rather from very small grains heated to temperatures of several hundred degrees by absorption of energetic photons of the interstellar radiation field. Small grains is in need to explain the 12 μm and 25 μm excess observed with *IRAS* toward galactic objects and external galaxies (Pajot *et al.* 1986; Cox and Mezger 1989).

Dust grains are assumed to be composite grains (Mathis and Whiffen 1989) in silicate, graphite, and amorphous carbon. These are coagulated each other with ice or icy mantle and is observed at 3.08, 4.67, 6.0, 6.58 and 10 μm features toward molecular cloud as in W33A (*e.g.*, Tielens 1989). Greenberg (1989) suggested that all remaining molecules may have accreted onto dust, and the very small (<0.01 μm) particles may have been collected and trapped within the outer volatile icy mantle, or the very small particles may accrete icy mantles in dense cloud after ultraviolet has turned off. Some grains may accrete as small protuberances on the outer parts of large grains enclosed in their own small mantles. On the other hand, Wright *et al.* (1989) proposed that dust has fractal structure. Dust consists of small grains glued together in large, open conglomerates by an all enveloping carbonaceous mantle (Tielens 1989). For any structure the dust near compact sources gets warm and icy mantle being melted by radiation or shock as discussed in Chapter 5. Under such condition, the abundance of SiO may increase.

The warm dust is associated with compact sources deeply embedded in the extended envelope of cold dust, which becomes optically thick at <100 μm. The warm dust emission may be heated by luminous compact sources, while the cold dust emission may be heated by both the interstellar radiation field and luminous compact sources (Sievers *et al.* 1991). Cold and warm components may contribute to the flux at 450 μm and 1,100 μm. The extent of the cold component is consistent with that of CS (MHH) and CO gas (Chapter 3). The extent of the warm component corresponds to the massive core.

4.4. Interpretation of the Spectral Index Map

Sievers *et al.* (1991) derived the spectral index map from 1,300 μm and 870 μm around W49N. The spectral index has a value of 3.0 around W49N. The index falls off steeply toward the northwest, south and southwest steeply fall off, while slightly toward other directions except toward southeast where it slightly increases. Sievers *et al.* (1991) interpreted the spectral index variation as follows. Optically thin warm dust spectra favor β=2 (*e.g.*, Gordon 1988) and their spectral index map supports this conclusion. The maximum value of the spectral index in their map occurs at the center of W49N, indicating that the compact sources consist of warm dust. The fact that this maximum attains the value β≈2 further shows that $T_d \geq$50 K, which is derived from the spectral fit. The index decreases toward the edge of the sources, which indicate that the dust in the extended envelope is colder (Sievers *et al.* 1991).

Our results show a similar tendency. The interpretation for our results is that the compact sources become optically thick and the spectral index approaches α=3. In the outer envelope, the spectral index approaching to α≈2 in Figure 4-4 means that the dust in the extended envelope is cooler.

Chini *et al.* (1986a; 1986b) and Chini, Krügel, and Kreysa (1986) have measured a number of compact H II regions selected from the *IRAS* survey with 90″ beam at 1,300 μm and deduced the average temperature of 26 K or 65 K according to the emissivity law of β=2 or β=1, respectively. On the other hand, many millimeter and submillimeter-wave and far infrared observations gave us various spectral indices of 0.5 to 4 for galactic and extragalactic sources (Helou 1989). These is no systematic differences in β between galactic and extragalactic dust. It should, however, be noted that β may vary systematically with wavelength as suggested by Whittet (1988). Gear, Robson, and Griffin (1988), who observed 11 compact H II regions and estimated dust emissivity at 350 μm to 3,300 μm. They estimated β values of β ≃1 for wavelength from 350 μm to 800 μm and β ≃1.8 for wavelength from 800 μm to 1,100 μm. The difference between this work and Sievers *et al.* (1991) is due to the effect of difference of observational wavelength.

The interplay between β and T is also assumed to be related with our results. Helou (1989) suggested that the interplay between β and T at submillimeter wave emissivity is indicated. When dust temperature becomes ~60 K, then the emissivity reach ~1. If we then sample warm dust, the estimated β approches ~1.

On the other hand, laboratory measurements in the far infrared yield values ranging from β=0.8 to β=3 (*e.g.*, Koike, Hasegawa, and Hattori 1987). Wright (1987) pointed out that β could not be more affected by its compositions but by the shape of conducting grains. Many researchers of grain emissivities at infrared and submillimeter wavelengths concluded that β=2 is due to silicate minerals such as olivine (*e.g.*, Aannestad 1975). The β=1 dependence is assumed to be concerned with special minerals such as amorphous

silicates (*e.g.*, Day 1976), surface effect (*e.g.*, Koike, Hasegawa, and Hattori 1984), and fractal effect (*e.g.*, Rouleau and Martin 1991). The emission efficiency at >100 μm is different between the ice mantle and core. Silicate grains follow β=2 dependence, while silicate ice mantle has β=3 (Aannstad 1975). Schwarz (1982) suggested that high dust emissivity of NGC 2264 had dust with thicker mantle. The difference of β values depends on the dust properties, temperature, and other factors.

5. CONCLUSIONS

We have obtained 450 μm and 1,100 μm maps of W49N. The peak flux densities at the component g are 510 Jy/beam and 30.8 Jy/beam at 450 μm and 1,100 μm with uncertainties of 50 % and 11 %, respectively. The 450μm map, resembling the ^{13}CO map, has the extent of $30'' \times 30''$ ($\alpha \times \delta$) at the half maximum levelwith two elongations from the component g; one is toward the southeast direction and, the other from northeast to southwest. The 1,100 μm map, resembling the $C^{32}S$ map of MHH and the 1 mm continuum emission (Westbrook *et al.* 1976), has the extent of $40'' \times 30''$ ($\alpha \times \delta$) at the half maximum level. The 1,100 μm map has three elongations; one is toward the southeast direction as like the 450 μm map, second is toward the northwest direction from the component g, third is from northeast to southwest like 450 μm. Another weak elongation toward the north from the component g is seen. The northern elongation seems to be the same feature as was seen in the integrated intensity maps of ^{12}CO, ^{13}CO, HCO^+. The southeast and northeast-to-southwest elongations seems to be related with the same feature of the 450 μm map. W49N has 20% of the flux density at 1,100 μm as free-free emission. The mass is estimated to be $5 \times 10^4 - 1.7 \times 10^5 M_\odot$ for $\lesssim 30''$. The mass is consistent with those estimated from molecular gas.

The spectral index map between 450 μm and 1,100 μm has a maximum at the center toward the compact sources. This is a finer image than Sievers *et al.* (1991) obtained. In the outer envelope, the spectral index is smaller than the center. The core with a diameter of 60″ has higher temperature than the envelope.

Chapter 5

INTERNAL STRUCTURE OF THE MASSIVE CORE

1. STAR FORMATION AND MASSIVE CORE

In previous chapters, I have presented millimeter and submillimeter observations of the massive core in W49A with single dish telescopes, and have discussed its properties. It has been argued that the core may be formed in a cloud-cloud collision event. Serabyn, Güsten, and Schulz (1993) identified three dense clumps with a few $10^4 M_\odot$ in the massive core in W49A from their CS multi-transition observations, and suggested that cloud-cloud collision is a reasonable scenario to account for the velocities of their clumps. I could not, however, sufficiently resolve the inside of massive core using single dish telescope.

High resolution observations with interferometers show internal structure of the massive core. VLA observations by Dreher *et al.* 1984 and Welch *et al.* 1987 have revealed a cluster of massive stars in W49A that appears as a rotating "necklace" (Welch *et al.* 1987). Dickel and Goss (1990) have observed the H_2CO line at 5 GHz, and estimated the density of molecular hydrogen for the velocity components of $\gtrsim$8.5 km s^{-1}, 8 km s^{-1}, and $\lesssim$5.5 km s^{-1}. NH_3 observation by Jackson and Kraemer (1994) have shown warm molecular gas associated with the "necklace". The velocity field of molecular gas indicates an inward radial motion at about 10 km s^{-1}They may correspond the localized accretion flows in individual star-forming fragments in massive core shown in theoretical calculations as the one by Keto, Lattanzio, and Monaghan (1991).

In this chapter, I present new high resolution images of the massive core taken with NMA (Nobeyama Millimeter Array) in the millimeter lines of $C^{32}S$ ($J = 1 - 0$), SiO ($J = 2 - 1$), and $H^{13}CO^+$ ($J = 1 - 0$), and discuss the internal kinematics and structure of the core.

2. OBSERVATIONS WITH NMA

2.1. *Observations of CS ($J = 1 - 0$) Emission*

Observations of $C^{32}S$ ($J = 1 - 0$) at 49 GHz toward W49A were made from April on 1988 to April 1989 using the Nobeyama Millimeter Array (NMA) on B, C and D configurations. Primary beam was $\sim$ 150″ at 49 GHz. The field center was taken at $\alpha(1950)=19^h07^m49\overset{s}{.}8$, $\delta(1950)=9°01'17\overset{''}{.}1$. I made no correction for the primary beam response for the CS maps resented in this paper. The antennas were equipped with SIS receivers having system noise temperatures of 200 K. They were turned to the frequency of $C^{32}S$ ($J = 1 - 0$; 48.990967 GHz) and a 1024-channel digital FFT spectro-correlator

covered a 80 MHz bandwidth. The spectral resolution (78 kHz) corresponds to a velocity resolution of 0.48 km s^{-1}. Bandpass calibration and flux calibration were carried out in the usual manner with 3C84 and 1749+096, respectively. The minimum and maximum baseline lengths were 20 m (3.1 kλ) and 210 m (32 kλ), respectively.

2.2. Observations of SiO ($J = 2 - 1$) and $H^{13}CO^+$ ($J = 1 - 0$) Emission

Observations of SiO ($J = 2 - 1$) and $H^{13}CO^+$ ($J = 1 - 0$) at 86 GHz toward W49A were made from January to April 1991 using the Nobeyama Millimeter Array (NMA) in C and D configuration. The SiO ($J = 2 - 1$) and $H^{13}CO^+$ lines were observed simultaneously in the 320 MHz band of the correlator. Primary beam was $\sim 80''$ at 86 GHz. I chose the field center at $\alpha(1950)=19^h07^m49^s.8, \delta(1950)=09°01'15''.5$. I made no correction for the primary beam response for the SiO and $H^{13}CO^+$ maps presented in this paper. The antennas were equipped with SIS receivers having system noise temperatures of 300 K. They were turned to cover the frequencies of SiO (v=0; $J = 2 - 1$; 86.846998 GHz) and $H^{13}CO^+$ ($J = 1 - 0$; 86.754330 GHz) with a 1024 channels digital FFT spectro-correlator with a 320 MHz bandwidth. The velocity resolution of one channel (312 kHz) was 1.08 km s^{-1}. Bandpass calibration and flux calibration were carried out in the usual manner with 3C273 and 1749+096, respectively. The minimum and maximum baseline lengths were 20 m (5.7 kλ) and 135 m (38 kλ), respectively.

2.3. Data Reduction

The visibilities of the continuum emission were estimated by interpolating between the visibilities at changed ranges free from emission or absorption features due to molecular lines. This continuum visibilities were subtracted from raw data to obtain the baseline of line visibility data.

I used the NRAO AIPS package to produce images. Continuum images were made by applying the self-calibration technique. The phase and amplitude correction found in this scheme were applied to make the line channel maps. The natural weighting was made. For 49 GHz observations, the resultant synthesized beams of the continuum and line images are $5''.6 \times 4''.3$ (PA=176.4°) and $9''.2 \times 6''.9$ (PA=-8.0°), respectively. The rms noise level in each channel map was less than 0.14 Jy/beam, which corresponds to 0.71 K. For 86 GHz observations, uniform weighting was taken and the synthesized beams of the continuum and lines images are $4''.7 \times 3''.7$ (PA=–65.2°). The rms noise level in each channel map was 0.15 Jy/beam, which corresponds to 2.6 K.

3. RESULTS OF INTERFEROMETRIC OBSERVATIONS

3.1. Continuum Emission

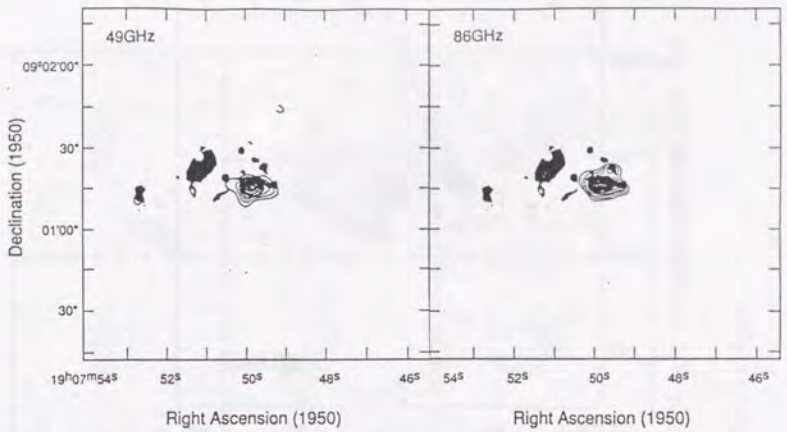

Figure 5-1: The Continuum Emission Maps at 49 GHz and 86 GHz (left) The 49 GHz continuum map superposed on 5 GHz continuum images (Dickel *et al.* 1990). Contour interval is 0.15 Jy/beam from 0.15 Jy/beam. Beamwidth is $5''.6 \times 4''.3$ (PA=176.4°), which is indicated at lower right corner of the panel. (right) The 86 GHz continuum map superposed on 5 GHz continuum images (Dickel *et al.* 1990). Contour interval is 0.15 Jy/beam. Beamwidth is $4''.7 \times 3''.7$ (PA=–65.2°), which is indicated at lower right corner of the panel.

The images of the continuum emission at 49 GHz and 86 GHz are shown in Figure 5-1 superposed on the 5 GHz continuum map (Dickel and Goss 1990). The positions of emission peaks are consistent with each other within errors. The brightest component is g with a flux of 2.89 Jy/beam and 2.44 Jy/beam at 49 GHz and 86 GHz. Our spatial resolution is not good enough to resolve the components g, d and a, but component c and j are resolved at 86 GHz and component c and a are merginally detected at 49 GHz. In the 5 GHz continuum map, the ultracompact H II regions appear to be arranged on an ellipse or ring with a major diameter of 30″ or 2 pc at a position angle 60° (Welch *et al.* 1987 and Dickel and Goss 1990). In the present 86 GHz continuum map, the ring structure is not as clear as in the 86 GHz image presented by Welch (1990). In his map with a $2''.5$ resolution components d and a are resolved. Extended component l, which may be older H II region than component a-j, is also detected in lowest contour level

3.2. Molecular Line Emission

3.2.1. CS ($J = 1 - 0$) Emission

Figure 5-2 shows an integrated intensity map of the CS emission for a velocity range of V_{LSR}= -6.0 km s^{-1} to 20.8 km s^{-1}Region of bright 5 GHz continuum emission (Dickel

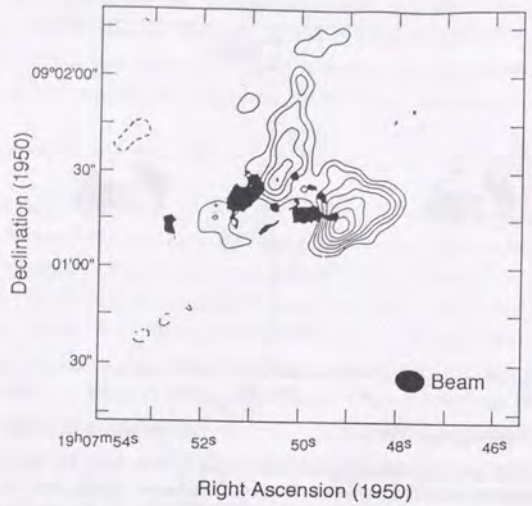

Figure 5-2: The Integrated Intensity Maps of $C^{32}S$ ($J = 1 - 0$) Emission The integrated intensity map of $C^{32}S$ ($J = 1 - 0$) at the velocity range from -6.1 km s^{-1} to 21.9 km s^{-1}. Contour interval is 0.05 Jy/beam from 0.1 Jy/beam.

and Goss 1990) are also shown. There are two peaks of the CS emission around W49N; one is at southwest of component g and another is between component h and i. Weak emission is detected also at southeast of component h.

Figure 5-3 shows a sequence of equi-velocity maps of the CS emission made at a 2 ch interval by averaging over 2 ch. The interferometric observations reproduce the basic results of single dish observations (MHH; Serabyn, Güsten, and Schulz 1993), except that extended structures are resolved out in the presented images. From -4.1 km s^{-1} to 18.9 km s^{-1}, the CS line has the strongest peak near W49N. The structure and kinematics around W49N are complicated. There are two major peaks; one is mainly at 15″ southwest from the component g and another is mainly at 25″ northeast of g. From -3.1 km s^{-1} to 2.6 km s^{-1}, the former peak is at 25″ northeast of g. This peak separates and one of them starts to get closer to the component g from V_{LSR}=2.6 km s^{-1}. It reaches 15″ north of g at V_{LSR}=5.5 km s^{-1}. This emission feature gets extended at velocities larger than V_{LSR}=9.3 km s^{-1}, and it appears as a shell-like structure at 12.2 km s^{-1} to 15.0 km s^{-1}. At V_{LSR}=14.1 km s^{-1} and V_{LSR}= 15.0 km s^{-1}, an elongation toward nor

Another southwest peak appears compact at V_{LSR} from 2.6 km s^{-1} to 5.5 km s^{-1}. From V_{LSR}=5.5 km s^{-1} to 9.3 km s^{-1}, this extends toward northwest and southeast direction. From V_{LSR}=9.3 km s^{-1} to 15.0 km s^{-1}, it peaks around W49N with sub-peaks located at 15″ west.

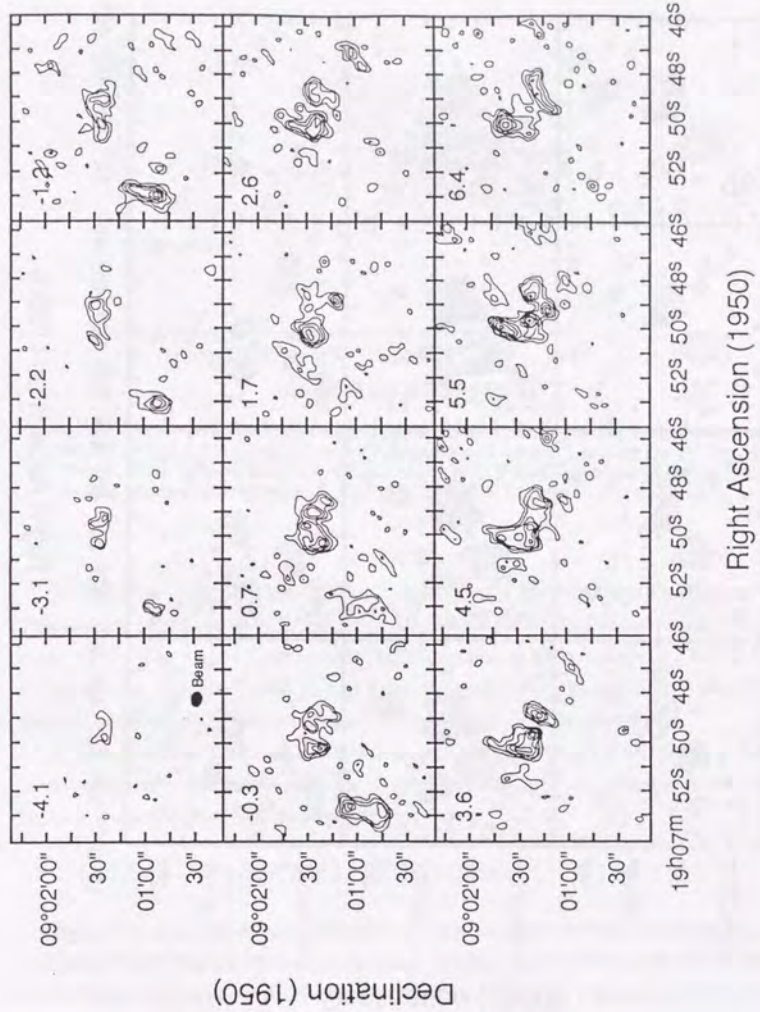

Figure 5-3: The Equi-Velocity Maps of $C^{32}S$ ($J = 1 - 0$) Emission The equivelocity maps of $C^{32}S$ ($J = 1 - 0$) averaged over 2 ch centered on the velocities from –4.1 km s^{-1} to 17.9 km s^{-1} shown in the upper left corner of the panels. The contour interval is 0.15 Jy/beam from 0.30 Jy/beam.

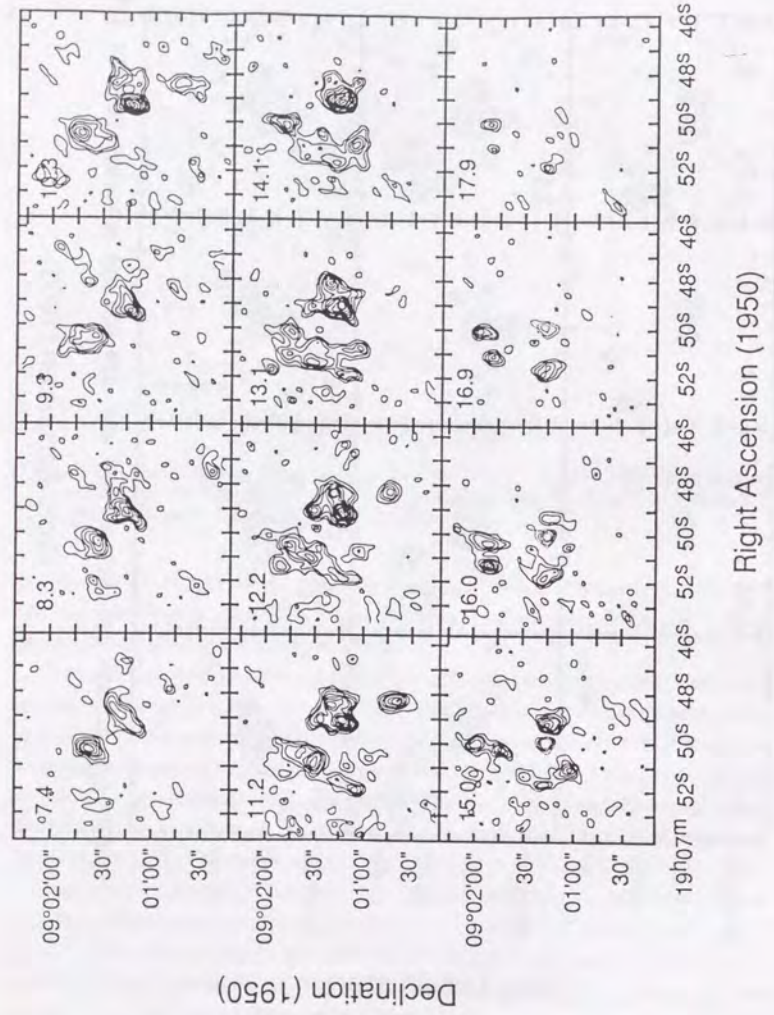

Figure 5-3: The Equi-Velocity Maps of $C^{32}S$ ($J = 1 - 0$) Emission

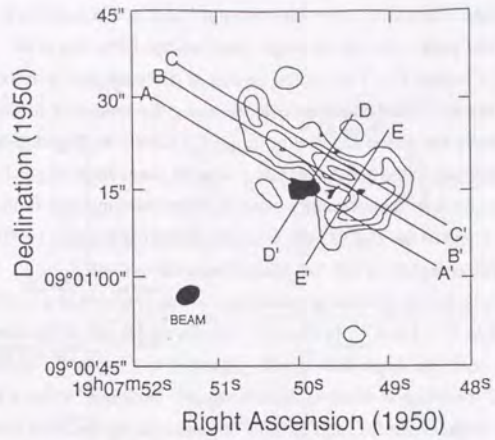

Figure 5-4: The Integrated Intensity Maps of SiO ($J = 2 - 1$) Emission The integrated intensity map of SiO ($J = 2 - 1$) at the velocity range from -1.4 km s^{-1} to 15.8 km s^{-1}. Contour interval is 0.1 Jy/beam from 0.2 Jy/beam. A-A' to E-E' cuts are shown in Figure 5-6a to 5-6e as position velocity maps.

At 15.0 km s^{-1} and 16.0 km s^{-1}, the CS absorption is observed toward component g. This can also be noticed in ^{12}CO and HCO^+ single dish and interferometer results (Welch *et al.* 1987). The 4 km s^{-1} component (MHH) appears to be surrounded by the 12 km s^{-1} component. The three dense clumps found by Serabyn, Güsten, and Schulz (1993) in their CS observations correspond to the velocity features described above.

A peak is seen at -3.1 km s^{-1} to 0.7 km s^{-1} at (100″, 30″) from the compone t g. This corresponds to the feature noticed in the ^{13}CO map in Chapter 3. Its structure is not clear because it was observed near the edge of field of view.

3.2.2. SiO ($J = 2 - 1$) and $H^{13}CO^+$ ($J = 1 - 0$) Emission

Figure 5-4 shows the image of the SiO ($J = 2 - 1$) emission integrated from V_{LSR}= -1.4 km s^{-1} to 15.8 km s^{-1}Å continuum image (Dreher *et al.* 1984) is also shown. The SiO emission is elongated in the northeast to southwest direction. The peak is at the center of the "necklace" of the H II regions. Another arc-shaped feature of strong emission is seen at the southwest side of the "necklace".

Figure 5-5 shows a set of equi-velocity maps of the SiO and $H^{13}CO^+$ emission made in a 2 channel interval by averaging over 3 channels. The SiO emission comes from

two regions; one is the center of the "necklace" and another is at southwest of it. These have different velocities. The SiO peak in the center of "necklace" occurs at $V_{LSR}\sim$ 6km s^{-1} coincident with the peak velocity of single observations (Downes *et al.* 1982; Ho and Haschick 1990; Chapter 2). The central region is detected over a velocity image of V_{LSR}=4.0 to 8.2 km s^{-1}. SiO emission extends along the near axis of the elliptical "necklace" as we clearly see in the channel at V_{LSR}=7.2 km s^{-1} in Figure 5-5a. On the other hand, the arc structure in the southwest has a velocity range from V_{LSR}=10.4 to 14.7 km s^{-1}. It may correspond to the secondary peak of molecular emission found in single dish map in Chapter 2 and to the H_2CO peak found by Dickel and Goss (1990). The SiO emission from the central feature in the "necklace" has a narrow vel

$H^{13}CO^+$ emission is mainly located at southwest of the component a in the velocity range from V_{LSR}=9.8 to 16.1 km s^{-1}. At 4 km s^{-1} it is located south of the component g. These are consistent with the single dish results presented in Chapter 3. The noticeable feature of the $H^{13}CO^+$ emission is an elongation along the "necklace" at 6 – 8 km s^{-1}.

Position velocity maps of the SiO and $H^{13}CO^+$ emission along the lines from A-A' to E-E' in Figure 5-4 are shown in Figure 5-6a to 6e. In the B-B' cut (Figure 5-6b) along the major axis of the "necklace", we note a velocity gradient from northeast to southeast, which is consistent with the results of the recombination line observations (Welch *et al.* 1987) . The velocity gradient found here matches in the larger-scale velocity gradient observed in the NH_3 lines (Jackson and Kraemer 1994)

3.3. Shell Structure in the Position Velocity Map

Figure 5-6a shows the cut A-A' through the strong continuum source g, parallel to the major axis of the "necklace". Figure 5-6d is the perpendicular cut D-D' across the "necklace" through the component g. In the SiO position velocity map in Figure 5-6a, an arc-shaped feature appears and it could be regarded as a part of a shell structure. The redshifted side is missing, and linewidth in the blueshifted side is only $\sim$ 1 km s^{-1} which is much narrower than the single dish spectra (Downes *et al.* 1982; Haschick and Ho 1990). The center of the shell may be located, if it is spherical, at $\delta(1950) = 9°01'15''.5$. The central velocity appears to be close to $\sim$8 km s^{-1} that is the central velocity of recombination lines from the H II regions in the "necklace" (*e.g.*, MHH). The SiO emission in the D-D' cut shows emission patches that can be regarded to form an arc reaching down to $V_{LSR}\sim$0 km s^{-1}. They could be part of the same structure noticed in the A-A' cut. Typical brightness temperatures of the

4. DISCUSSION

4.1. Contribution of Dust Emission to the Observed Continuum Fluxes

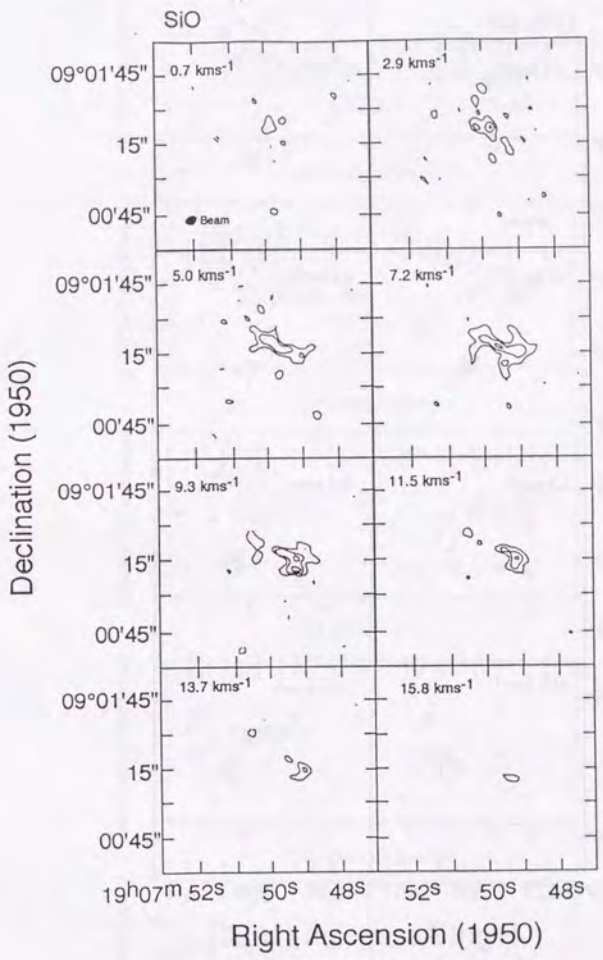

Figure 5-5a: The Equi-Velocity Maps of SiO and $H^{13}CO^+$ Emission The equivelocity maps of SiO ($J = 2 - 1$) averaged over 3 ch centered on the velocities from –0.7 km s^{-1} to 15.8 km s^{-1} shown in the upper left corner of the panels. The contour interval is 0.20 Jy/beam from 0.40 Jy/beam.

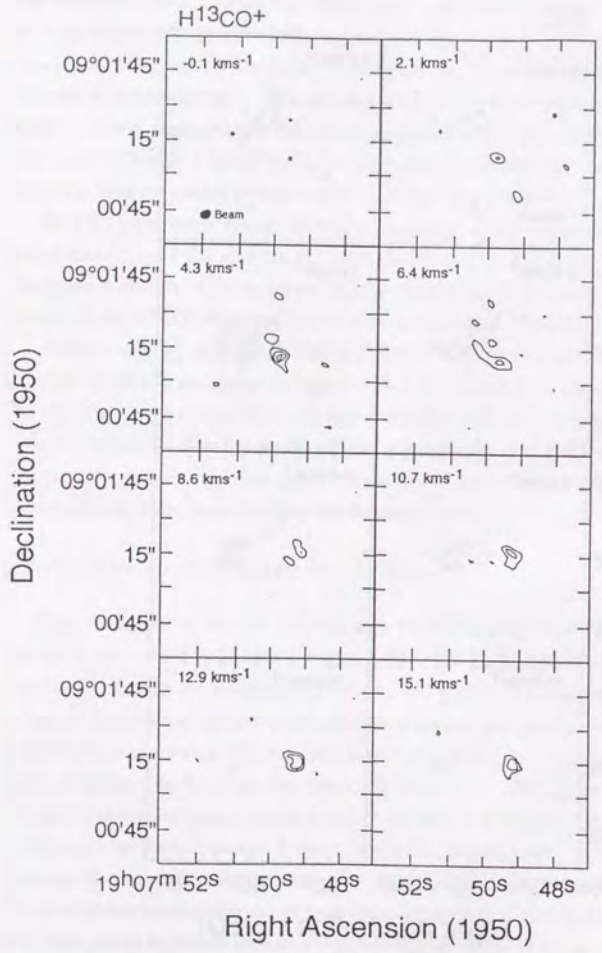

Figure 5-5b: The Equi-Velocity Maps of SiO and $H^{13}CO^+$ Emission The equivelocity maps of $H^{13}CO^+$ averaged over 3 ch centered on the velocities from –0.1 km s^{-1} to 15.1 km s^{-1} shown in the upper left corner of the panels. The contour interval is 0.20 Jy/beam from 0.40 Jy/beam.

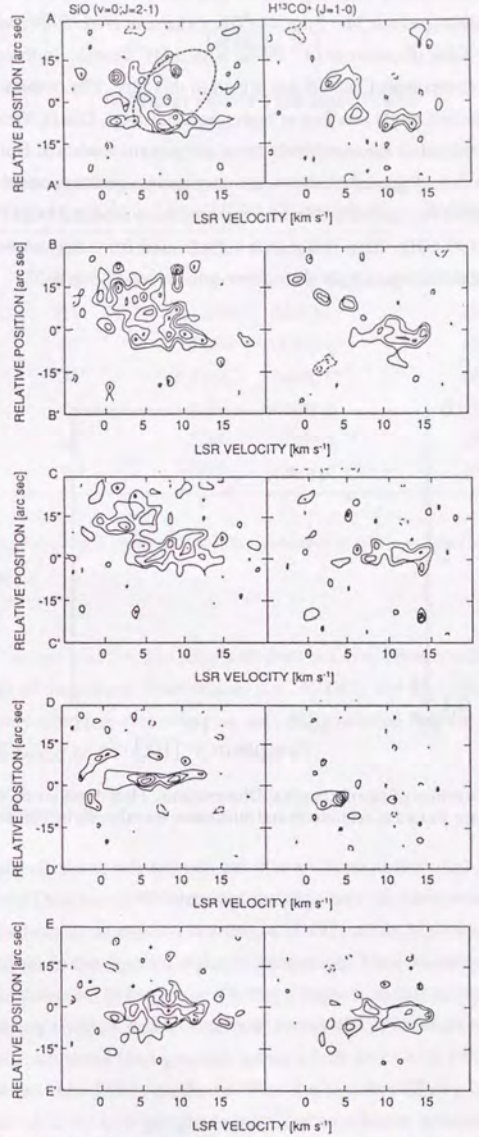

Figure 5-6: The Position Velocity Maps along A-A' to E-E' Cuts. Figures 5-6a to 5-6e correspond to A-A' to E-E' Cuts, respectively. Contour interval is 0.2 Jy/beam from 0.4 Jy/beam.

The continuum flux observed in interferometric observations is assumed to be a part of continuum emission measured by single dish. The flux densities observed toward W49N with single dish telescopes are 34.1 Jy at 43 GHz (Akabane *et al.* 1989; with a 45″ beam) and 33.0 Jy at 84 GHz (Gordon *et al.* 1986; with a 70″ beam). In these observations, fluxes of both the component C and B are mixed in this flux. The component C (h) is an evolved H II region, and emits less flux at high frequency (*e.g.*, Dieter, Welch, and Wright 1979). The interferometric measurements from the present work and from the literature are listed in Table 5-1. Figure 5-7 shows the continuum spectrum based on them. Flat spectrum from typical for optically thin free-free emission is seen 23 GHz to 86 GHz and it rises steeply at 110 GHz. This is due to a contribution from dust emission, which we have seen from submillimeter single dish observations (see Figure 4-5).

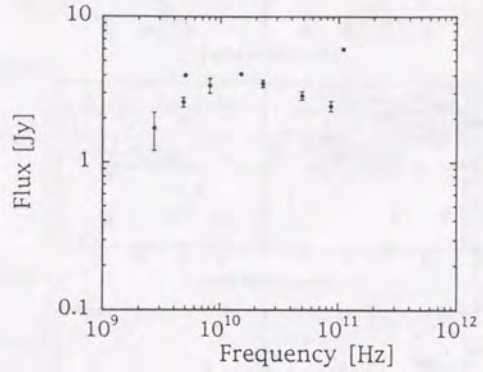

Figure 5-7: Flux Densities of Interferometric Observations. Flux densities of W49N, especially component g, are plotted at centimeter and millimeter wavelength by interferometer in Table 5-1.

TABLE 5-1

Millimeter-Wave Flux from W49N

Frequency [GHz]	Flux [Jy]	Components	Refferences
2.7	1.7±0.5	comp C	(1)
5.0	4.0	comp b+d+e+g	(2)
8.1	3.4±0.4	comp C	(1)
15	4.07	comp g	(3)
23	3.5±0.2	comp C	(4)
49	2.89	comp g	(5)
86	2.44	comp g	(5)
110	6.02	comp C	(6)

References: (1) Wink *et al.* (1975); (2) Dickel and Goss (1990); (3) Dreher *et al.* (1984); (4) Dieter *et al.* (1979); (5) This work; (6) Scoville *et al.* (1986)

Figure 5-7 shows that the dust emission does not contribute much to the total flux at the frequencies of the present observations (i.e., 49 GHz and 86 GHz). The 49 GHz flux is almost entirely from free-free emission, and dust emission contributes less than 5 % to the continuum flux at 86 GHz.

4.2. The SiO Abundance

The SiO abundance is related with gas phase chemical reactions and dust chemistry. Ziurys, Snell and Dickman (1989) detected emission near the various molecules toward the highly perturbed clouds of supernova remnant IC443, where high-temperature gas phase chemical reactions in the shocked region are expected. They found that the abundance of SiO relative to molecular hydrogen is 100 times larger than that in quiescent dark clouds. Shocked chemistry with the shock velocity as low as 40 km s^{-1} showed that silicate grains are more easily distracted than graphite grains (Serb and Shull 1983). The laboratory experiment shows that SiO is produced from the silicates (Duley and Boehlau 1986). Reactions such as Si + O_2 in gas phase may lead to efficient production of SiO in high temperature and high density conditions (Herbst *et al.* 1989), which may be consistent

with the observations by Ziurys, Friberg and Irvine (1989) and by Yamamoto *et al.* (1992). Langer and Glassgold (1990) suggested that the lack of Si

Another possibility is that the icy grain mantles, which can be destroyed at lower temperature than silicates, evaporate to form SiO in shocks as suggested by Herbst *et al.* (1989). Physical and chemical properties of dust are not, however, well known, so is the chemistry of SiO and Si bearing molecules. Dust may consist of small grains glued together in large, open conglomerates by an all enveloping carbonaceous mantle (Tielens 1989). These dust complexes get warm and icy mantles might melt or evaporate by radiation or shock near young H II regions.

These arguments suggest that the SiO emission in W49A arises in possibly shocked gas with a high density and temperature. Serabyn, Güsten, and Schulz (1993) reported that the SO_2 peak lies near the center of the "necklace". The abundance of SO_2 is expected to be greatly enhanced in shock gas, and this also supports the above idea. The SiO-emitting region to the southwest of the "necklace" is also known to be dense and hot (Dickel and Goss 1990)

4.3. Shell Structure of CS Emission and Cloud-Cloud Collision

>From their single-dish CS observations, Serabyn, Güsten, and Schulz (1993) found three dense clumps in the massive core of W49A. Two of the clumps to the southwest and to the northeast have velocities of $\sim$12 km s^{-1} while the one between them has a velocity of $\sim$4 km s^{-1}. The present interferometric observations of the CS ($J = 1 - 0$) line reveal their structure and kinematics in greater detail. Figure 5-8 show the CS intensities at velocities of 3.6 km s^{-1} and 14.1 km s^{-1} superposed on the 5 GHz radio continuum image by Dickel and Gross (1990). The emission at 3.6 km s^{-1}fills in the gap of the emission at 14.1 km s^{-1}. The eastern part of the 14.1 km s^{-1} emission is curved so as to encircle the 3.6 km s^{-1}emission as well as the "necklace", emission peaks at the two velocities are coincident with each other. This would be a reflection of a large linewidth due to a complex velocity field.

The structure described above is quite indicative of a cloud-cloud collision event, in which the clump at $\sim$4 km s^{-1} collided into the cloud at $\sim$12 km s^{-1}. We observe the event almost end-on, i.e., from a line of sight almost parallel to the axis of the collision.

Numerical simulations of a collision between clouds with unequal sizes were presented by Habe and Ohta (1992). As the collision proceeds, the larger, less dense cloud becomes severely distorted due to a bow shock in front of the denser, compact clump. The CS emission may dense regions of the colliding clouds.

The above comparison between the observations and the numerical simulation supports the cloud-cloud collision scenario. A schematic picture of W49A is shown in Figure 5-9. In Chapter 3, we have found that the masses of the 4 km s^{-1} and 12 km s^{-1} components are

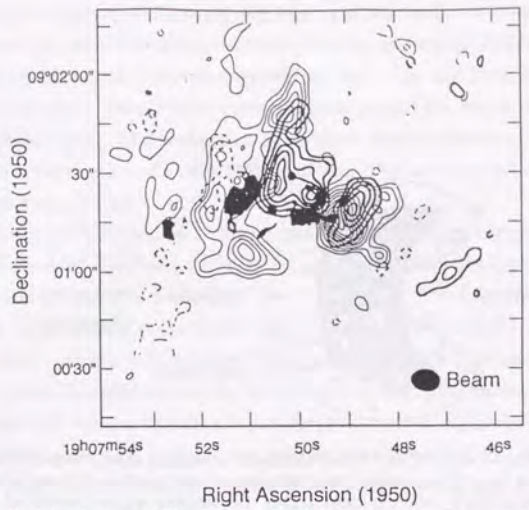

Figure 5-8: Distribution of The 4 km s^{-1} and 12 km s^{-1} Components. Thick line indicate 4 km s^{-1} component of 3.6 km s^{-1} feature and thin line indicate 12 km s^{-1} component of 14.1 km s^{-1} feature in Figure 5-3. Contour interval is 0.15 Jy/beam from 0.30 Jy/beam. Shade indicates 5 GHz continuum image (Dickel and Goss 1990).

similar with their sizes different. The colliding small, but denser clump at $\sim$4 km s^{-1} might be contracting now by self-gravity. This can explain the formation of the W49A massive core and its collapse. In the massive core several fragments have grown up and they have formed the massive stars, which are now observed as the "necklace" of ultracompact H II regions.

4.4. Infall Gas and Accretion Shock

The shell structure noticed in the SiO ($J = 1 - 0$) emission is inside the W49A dusty cocoon, but is more than 0.3 pc far from the ultracompact H II regions from its size. What is the shell structure and how was it formed? There are several possibilities, i.e., a bipolar flow or disk infalling gas and a shock front of the cloud-cloud collision.

The SiO thermal emission has also been detected in several low mass star forming regions, *e.g.*, L1448 (Bachiller, Martin-Pintado, and Fuente 1991), L1157 (Mikami *et al.* 1992), and B1 (Yamamoto *et al.* 1992). It arises from an interaction region between a bipolar outflow and dense gas.

The bipolar outflow associated with the component g (Scoville *et al.* 1986; Gwinn *et al.* 1992) should also affect surrounding molecular gas because the dense molecular gas and dust concentrate round the component g. The direction of the bipolar outflow is

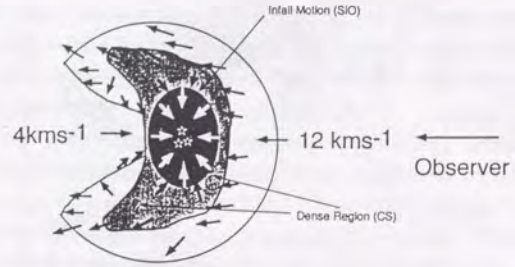

Figure 5-9: Schematic Model of Cloud-Cloud Collision. Molecular clouds with different sizes collide and the 4 km s^{-1} component cloud take place infall motion. SiO emitting region correspond to colliding or infalling shock region. CS emitting region correspond to dense part of colliding region and infalling molecular cloud.

northwest and southeast, fits comfortably in the rotating "necklace" picture. However the kinematics of the SiO shell structure disagrees in some points with what we expect for a shell swept up by the bipolar outflow. The velocity of the outflow source is V_{LSR}~5 km $s^{-1}$and is not at V_{LSR}~8 km s^{-1}, the central velocity of the shell. The blue-shifted side of the SiO shell appears to be inclined toward an opposite direction. It is not even perpendicular to the plane of the "necklace".

Another probability is that the shell-like appearance in the SiO emission is due to an infalling motion of the gas in the massive core. Expansion may not be possible because the massive core is gravitationally unstable (MHH). Indeed, Welth *et al.* (1987) found redshifted $H^{13}CO^{+}$absorption toward some of the ultracompact H II regions and suggested a gravitational infall of the core as a whole. Keto, Lattanzio, and Monagham (1991) presented a theoretical argument for the probability of infall toward each fragment of "necklace". It has been suggested that SiO emission in W49A is optically thick (Haschick and Ho 1990). If the motion is infall rather than expansion, the redshifted emission would be weak due to self-absorption. This is consistent with the observations. Our observations show that the density is more than $\sim 10^5 cm^{-3}$ (Chapter 3) in this region and the mass of the indivisual fragment is $\sim 5 \times 10^3 M_\odot$. The free fall time of each of the fragments is estimated to be $\sim 3 \times 10^5 yr$ and the free fall velocity is $\sim$ 3 km s^{-1}. This is consistent with the observed velocity of the shell.

Simple models of an accreting and rotating cloud can fit the observed shell structure. In Figure 5-6, I show one of them with an inclination angle i=60°, a cloud radius 15″, or 0.9 pc, and rotational and infall velocities of 2 ± 1 km s^{-1}/pc and 5 ± 2 km s^{-1}, respectively. The oval shape is more inclined and elongated toward the major axis when rotational velocity increases. The contamination of other broad emissions from the "necklace" disturbs determination of a unique set of values. The lack of redshifted shell makes the situation more difficult.

If this shell is formed by a cloud-cloud collision between compact cloud with 4 km s^{-1} and extended cloud with 12 km s^{-1}, it is natural that the redshifted side of the shell is not present because it is not formed

The sonic velocity is less than 1 km s^{-1} in ordinary molecular gas conditions. The shocks due to accretion or collision would stand around the component g. If the shocked shell is due to the infall motion, the mass accretion rate can be estimated as 0.06 $M_\odot yr^{-1}$, from the infall velocity of 5 km s^{-1} and the gas density of $n(H_2)=10^5 cm^{-3}$. This is much larger than what we get for formation of lower mass stars (e.g., GL 490; Nakamura *et al.* 1991). Mass accretion with this rate for 10^5 *yr* would form several fragments with a total mass of 5×10^3 $M_\odot$. They might have formed massive stars.

4.5. Star Formation in W49A Massive Core

Triggered collapse case of Habe and Ohta (1992) gives us a reasonable explanation for the star formation in W49A massive core. The observed 4 km s^{-1} component corresponds to the small cloud in their simulation and the 12 km s^{-1} component is the large cloud. Their model *14-h* may be close the actual case, in which the clouds have the same mass and their relative velocity is 10 Mach numbers.

First, strong shock waves occur in both colliding clouds and the shocks propagate into both clouds along the collision axis. The density of postshock gas in the small cloud increase and it takes a disklike shape. On the other hand, the shock wave becomes a bow shock in the large cloud. Secondary, when the shock wave reaches to a half of the small cloud, the outer portion of the post shock gas of the small cloud moves away from the collision axis by a rarefraction wave. Though the mass of small cloud decreases due to this expansion, the inner portion of small cloud contracts toward the center due to self-gravity and the central density increases exponentially. Third, after the shock wave completely passes through the small cloud, a rarefaction wave occurs in the back portion of postshock gas. The gravitational contraction and the expansion due to the rarefaction wave deform again the disk-like gas into a spherical shape. This process makes the post shock gas more compact. The contracting cloud may fragment into smaller denser parts, which will eventually form a cluster of massive stars. The fragments may have a strong magnetic field and a rotation. They preferentially form massive stars as discussed in Appendix 3.

Nakano, Hasegawa, and Norman (1995) examined the relation between masses of forming stars and the mass of molecular clumps which form the stars. They suggested that it is necessary for forming massive stars that molecular cloud core has high mass. Massive stars might need some external trigger that forms massive fragments.

5. CONCLUSIONS

I have observed the $C^{32}S$ ($J = 1 - 0$) emission at 49 GHz and the SiO ($v = 0$; $J = 2 - 1$) and $H^{13}CO^+$ ($J = 1 - 0$) emissions toward W49N with NMA. The 4 km s^{-1} component of the CS emission has a compact distribution surrounding the component g. On the other hand, the 12 km s^{-1} component is distributed at the edge of the 4 km s^{-1} component. This kinematical structure is interpreted in the context of a cloud-cloud collision seen end-on. A shell structure may be formed in the collision and the CS emission samples interface dense regions of colliding clouds. The compact and dense cloud at 4 km s^{-1} may be contracting by self-gravity. This may explain the formation of the W49A massive core and its collapse.

Around the component g, the SiO abundance is higher. A possibility to explain the shell structure observed in the SiO emission around the component g is a gravitational infall toward g. Shocks driven by this accretion or cloud-cloud collision may enhance the SiO abundance. The observed kinematics supports the formation process of "necklace" discussed in Chapter 3, which is consistent with the numerical simulation (Keto, Lattanzio, and Monaghan 1991).

Chapter 6

LARGE SCALE STAR FORMATION

1. LARGE SCALE GAS DISTRIBUTION

In previous chapters, I discussed structure and kinematics of W49A, mainly W49N. I have already discussed small scale distribution around W49N in Chapter 3. In case of massive star formation taken place by cloud-cloud collision, the relation between W49N and W49S must be also discussed. There was, however, no explanation about the relation between W49N and W49S in previous works and this works.

Large scale process of GMC formations and massive star formation in our Galaxy and external galaxies is discussed that once the density-wave developed, the accumulations in density inter arm, and creating systematic encounter velocities between gas cloud, and favorite cloud collisions. Collisions between molecular clouds are highly inelastic, and coalescence forms giants molecular clouds (GMC), where young star associations are produced. When I discuss star formation of W49A caused by cloud-cloud collision, I must consider not only W49N but another star forming region, W49S, neighborhood of W49N. W49S is cometary H II region dominated by a bright head with a steep brightness gradient in one direction and a diffusion tail of emission trailing in the opposite direction. W49S has large velocity width and velocity gradient of hydrogen recombination line (Gaume and Claussen 1990) like G34.3+0.2 (*e.g.*, Garay, Rodoriguez, and van Gorkom 1986).

Mufson and Liszt (1977) presented the large scale distribution of ^{12}CO. They revealed that other peak near W49S exists at 12 km s^{-1}. Their angular resolution was not able to resolved the distribution around W49S and there was no discussion of W49S. FIR results (Harvey, Campbell, and Hoffmann 1977) also detect emission from W49S but there was no discussion of the relation. Dickel and Goss (1990) discuss star formation of W49N and W49S but they seemed to consider that those are separate origin.

In this chapter, I discuss star formation of whole W49A including W49N and W49S by large scale mapping.

2. OBSERVATIONS WITH THE 45 M TELESCOPE

Observations were made on 1989 using the 45 *m* telescope of the Nobeyama Radio Observatory. I made mapping observations of ^{13}CO, HCO^+, and HCN in an area of 7′ × 6′ ($\alpha \times \delta$), or (48 pc × 41 pc), with a grid spacing of 30″ (1.7 pc) at the adopted distance of 11.7 kpc. The observational parameters about antenna parameters are listed in Chapter 2 in Table 2-1 and in Table 2-2. I used the following three single-sideband receivers. The receiver MIL100 had a frequency coverage from 85 to 115 GHz with an

instantaneous bandwidth of 500 MHz. The receiver AIL80 covered from 70 to 90 GHz with an instantaneous bandwidth of 2 GHz. I used it to observe molecular lines at the 80 GHz band simultaneously with the MIL100 receiver for 110 GHz lines. The receiver SIS40 was used for pointing.

The spectral data were taken with 16 banks of acousto-optical spectrometer (AOS) with 32,000 channels in total. Eight of them were high-resolution AOS with a frequency coverage of 40 MHz each and a resolution of 37 kHz, which corresponds to the velocity resolution of 0.10–0.13 km s^{-1} at 86–110 GHz . The other eight banks were wide-band AOS with a frequency coverage of 250 MHz each and a resolution of 250 kHz, which corresponds to the velocity resolution of 0.68–0.87 km s^{-1} at 86–110 GHz and 1.56 km s^{-1} at 48 GHz.

The pointing of the antenna was carefully checked during the observations by monitoring the SiO maser emission (v=1; $J = 1 - 0$) from R Aql at $\alpha(1950) = 19^h03^m57^s.68$, $\delta(1950) = 8°09'7''.7$ about every 2 hours. The change in antenna pointing was within 5″ in moset cases. I did not use the data when subsequent pointing varied more than 10 ″ under strong wind conditions.

All the data were taken under the position switching mode with the OFF position +17′ away in declination. Calibration was achieved by the standard chopper wheel method. The intensity scale is the antenna temperature, T_A^* corrected for atmospheric and ohmic losses (Ulich and Haas 1976). The spectra at the reference center was observed recurrently so that the variation of antenna gain was checked.

3. LARGE SCALE ^{13}CO DISTRIBUTION

Figure 6-1 shows integrated intensities maps of ^{13}CO, HCO$^+$, and HCN.

3.1. Large Scale Distribution of ^{13}CO

Integrated intensity ^{13}CO map of Figure 6-1 has two peaks at W49N and W49S. Feature around W49N is reported on results in Chapter 3. I could not obtain fine structure of W49A owing to 30″ gridding but obtained large scale distribution. There are north and north-east elongations whose sizes are both 150″ from W49N. South-west elongation from W49N also reach at (-200″,-180″). South-east part of W49N has diffuse feature and there is arc structure around W49S. Length of cometary structure is ∼6 pc. This structure was not seen in the results of Mufson and Liszt (1977) with their low spatial resolution of 65″.

^{13}CO map in Figure 6-1 is similar to 53 μm emission (Harvey, Campbell, and Hoffmann 1977) and 23 GHz continuum emission (Wink *et al.* 1975) as well as ^{12}CO results (Mufson and Liszt 1977). The similarity as well as the results in Chapter 3 between the ^{13}CO line and 53 μm continuum emission, which arise from hot (some hundreds of kelvins) dust

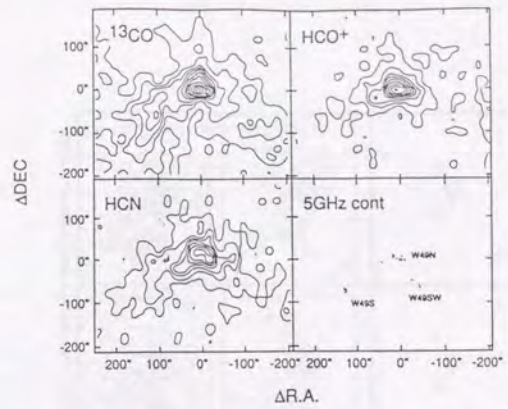

Figure 6-1: The Integrated Intensity Maps of ^{13}CO, HCO$^+$, and HCN (upper left) the integrated intensity map of ^{12}CO at the velocity range from -10 km s^{-1} to 25 km s^{-1}. Contour interval is 10 Kkm s^{-1}. (upper right) the integrated intensity map of HCO$^+$ at the velocity range from -10 km s^{-1} to 25 km s^{-1}. Contour interval is 10 Kkm s^{-1}. (bottom left) the integrated intensity map of HCN at the velocity range from -10 km s^{-1} to 25 km s^{-1}. Contour interval is 10 Kkm s^{-1}. (bottom right) The 23 GHz continuum image (Dieter *et al.* 1979).

grains in the H II region, is a natural consequence if the integrated ^{13}CO peak intensity reflects the gas temperature distribution of that velocity.

Figure 6-2 shows the equivelocity maps of ^{13}CO emission averaged over an 1 km s^{-1} and an 1 km s^{-1} interval. There are three velocity components, 4 km s^{-1}, 12 km s^{-1}, and 17 km s^{-1} components. The 17 km s^{-1} component is assumed to be associated with both W49N and W49S.

Over all velocity ranges, the peak is associated with W49N, and weak north elongation exists. Peak of the velocity ranges from -3 km s^{-1} to 2 km s^{-1} is at (75″, -50″). Another peak is adjacent to that peak at (120″, -20″) from 8 km s^{-1} to 12 km s^{-1}, and that shift to (100″, -70″) from 13 km s^{-1} to 15 km s^{-1}. (100″, -70″) peak is assumed to be connection with (120″, -80″) peak seen at the velocity of 16 km s^{-1} to 20 km s^{-1}. Both are assumed to be associated with W49S. The contours of velocity ranges from 10 km s^{-1} to 14 km s^{-1}in the integrated intensity of ^{13}CO are clumpy at southeast part including W49S. Southwest elongation is dominant from V_{LSR}= 0 km s^{-1} to 11 km s^{-1}.

Molecular line observations had already been presented by several authors. Mufson and Liszt (1977) presented that the 4 km s^{-1} and 12 km s^{-1} component have a north elongation, and that the 12 km s^{-1} component have also southwest elongation fromthe results of ^{12}CO obsevations with 65″ beamwidth. They also presented that the 12 km s^{-1}

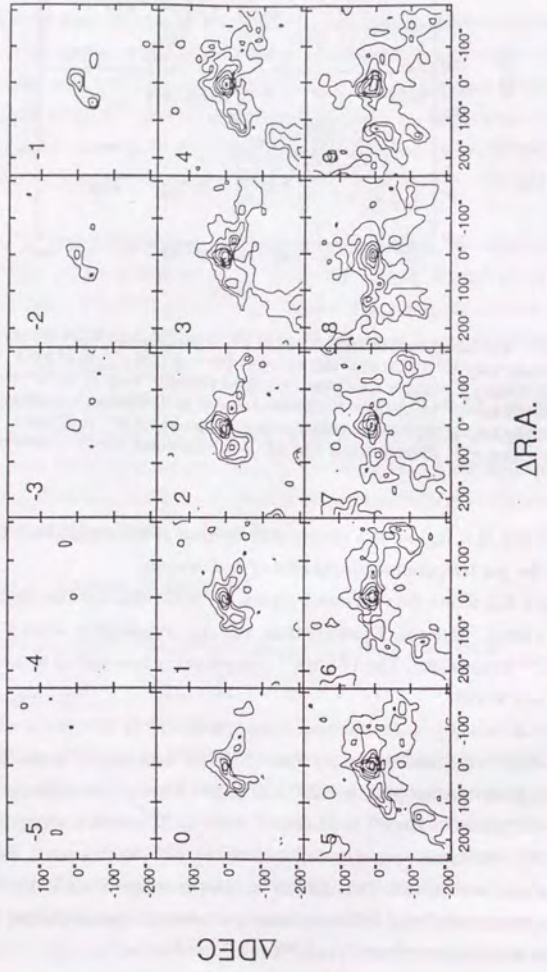

Figure 6-2: The Equi-Velocity Map of ^{13}CO. The equivelocity maps of ^{13}CO averaged over 1 km s^{-1} centered on the velocities from -5 km s^{-1} to 22 km s^{-1} shown in the upper left corner of the panels. The contour interval is 1 K. Plus and cross indicate W49N (component g) and W49S, respectively.

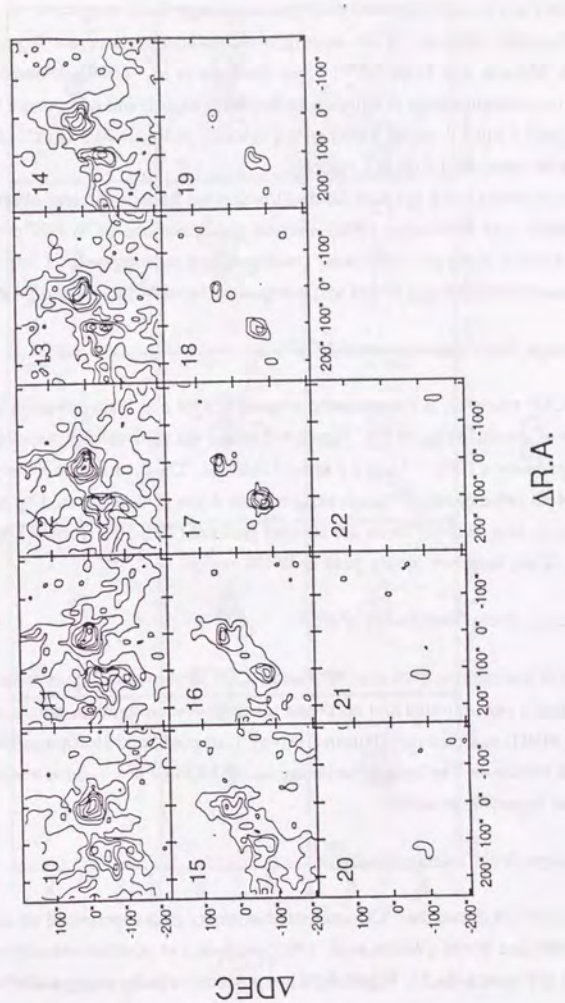

Figure 6-2: The Equi-Velocity Map of ^{13}CO.

component has a peak at W49S. Goss and Tilanus (1985) found that two major clouds are at V_{LSR}=4 km s^{-1} and 12 km s^{-1} and the entire complex of sources are covered with the 12 km s^{-1} component from H_2CO results. On the other hand, the 4 km s^{-1} component is absorbed and that is connected with the component C.

The LSR velocities of the hydrogen recombination lines are V_{LSR}~8 km s^{-1} (*e.g.*, MHH, Mufson and Liszt 1977). van Gorkom *et al.* (1980) showed the H109α line emission concentrations at component B (component l) and component C with a velocity of V_{LSR}=7.5 km s^{-1} and at W49S with a velocity of V_{LSR}=10.9 km s^{-1}. Component I and J are also associated with H II regions.

On the other hand, hot dust distribution derived from far infrared observations (Harvey, Campbell, and Hoffmann 1977) showed condensations of W49N and W49S. W49N condensation elongates southwest corresponding to component I and J. Warm dust is not concentrated around W49S and component I and J (Sievers *et al.* 1991).

3.2. Large Scale Distribution of HCO$^+$

HCO$^+$ emission is concentrated around W49N and little emission emit from W49S region as shown in Figure 6-1. Figure 6-3 shows the equivelocity maps of HCO$^+$ emission averaged over a 1 km s^{-1} and a 1 km s^{-1} interval. The distribution mainly concentrates at W49N all velocity range though images from 6 km s^{-1} are affected by self-absorption as discuss at next section. There are another peaks at (70″,-30″) from -4 km s^{-1} to 2 km s^{-1}. There is not, however, strong peak at W49S region.

3.3. Large Scale Distribution of HCN

HCN emission is between ^{13}CO and HCO$^+$ as shown in Figure 6-1c. Around W49N emission is concentrated and northeast to southwest elongation, which is consistent with C^{32}S (MHH) and dust distribution (Harvey, Campbell, and Hoffmann 1977). W49S have a weak emission. The velocity structure usung HCN ($J = 1 - 0$) is unclear because HCN line has hyperfine structure.

3.4. Large Scale Velocity Structure

Figure 6-4 shows the ^{13}CO integrated intensity map superposed on continuum images of W49N and W49S (Welch *et al.* 1987) with cuts of position-velocity maps , which are shown in Figure 6-5a-5d. Figure 6-5a is a position-velocity map parallel to right ascension across component g. This figure is similar to ^{12}CO position velocity map of Mufson and Liszt (1977). The 4 km s^{-1} component is more compact than the 12 km s^{-1} component, which is spread over to neighborhood of W49S. This tendency is also dominant at the figures with ±30″ cut of Figure 6-5a. Toward component g the 4 km s^{-1} and 12 km s^{-1}

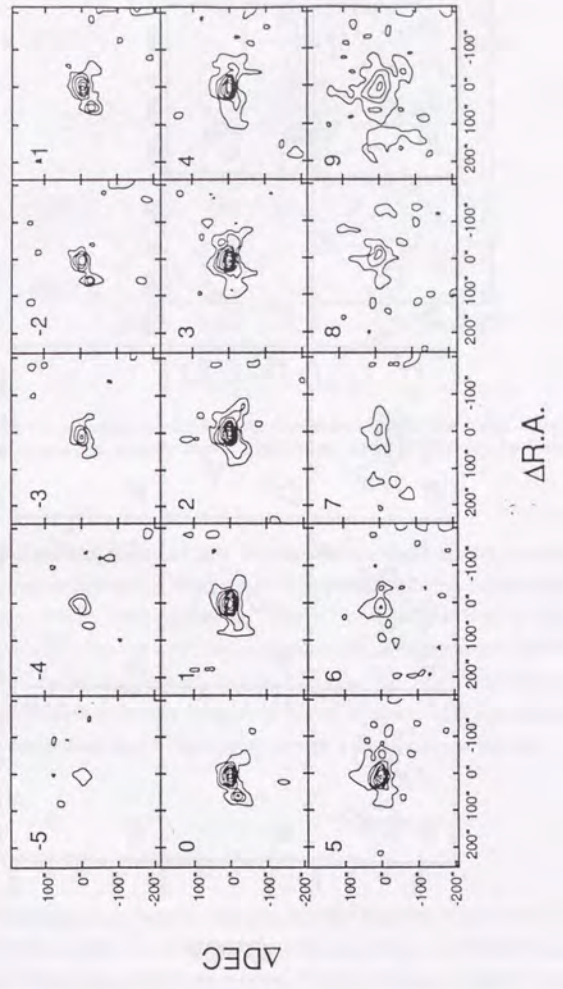

Figure 6-3: The Equi-Velocity Map of HCO$^+$ The equivelocity maps of HCO$^+$ averaged over 1 km s^{-1} centered on the velocities from -5 km s^{-1} to 22 km s^{-1} shown in the upper left corner of the panels. The contour interval is 1 K. Plus and cross indicate W49N (component g) and W49S, respectively.

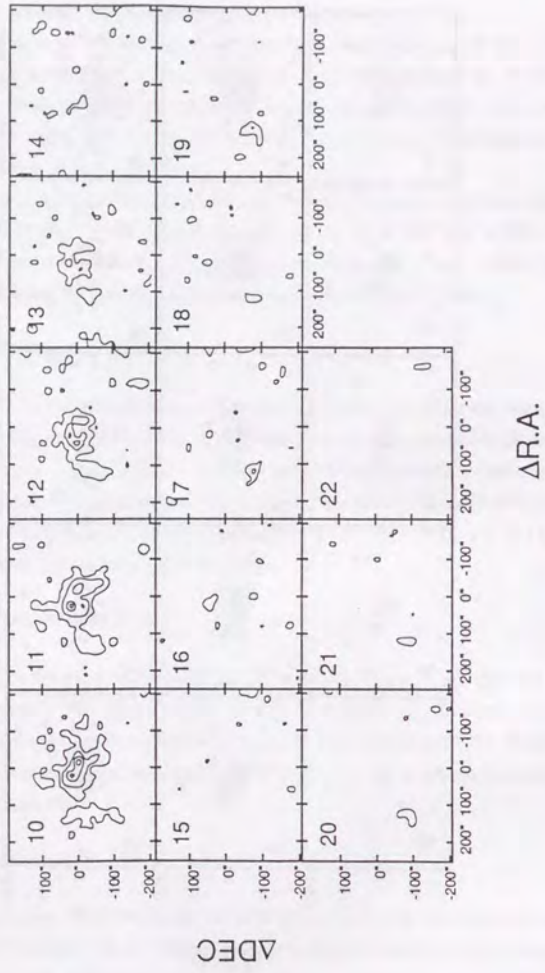

Figure 6-3: The Equi-Velocity Map of HCO^+

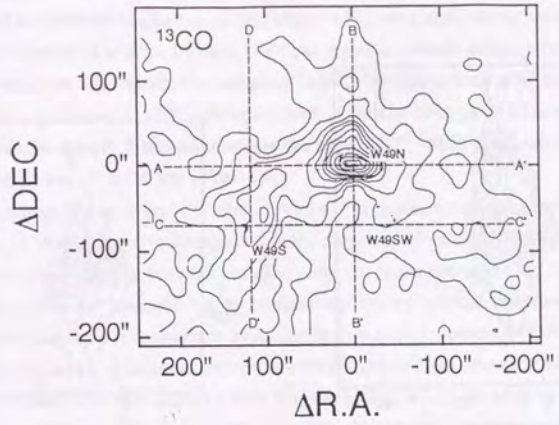

Figure 6-4: The ^{13}CO Intgrated Intensity Map Superposed on Continuum Image. Dashed lines indicate cuts of position velocity maps. Continuum image is obtained by Welch *et al.* (1987).

components distribute with similar extents. Figure 6-5b is a position-velocity map parallel to declination across component g. The 4 km s^{-1} component, which is brighter than the 12 km s^{-1} component, is more compact than the 12 km s^{-1} component as well as Figure 6-5a. Figure 6-5c shows a position-velocity map parallel to right ascension across W49S. W49S has a peak at 120″. Large velocity gradient with 0.25 $kms^{-1}pc^{-1}$ can be seen from west to east. The 17 kms component is only seen aroud W49S. Figure 6-5d is a position-velocity map parallel to declination, which has several clumps with varoious velocities.

4. DISCUSSION

4.1. Cloud-Cloud Collision and Massive Star Formation

As mentioned in previous chapters, cloud-cloud collision model is influential. Scoville, Sanders, and Clemens (1986) also suggested that OB stars form as a result of cloud-cloud collisions on the statistical basis that the number density of luminous galactic H II region show a quadratic dependence of on the local density of H_2. Scoville *et al.* (1987) presented that clouds with H II region exhibit higher peak of ^{12}CO temperatures, which is due to an effect of the high luminous stars rather than a cause of the massive star formation.

In case of W49A, several velocity components are interacting and there are several

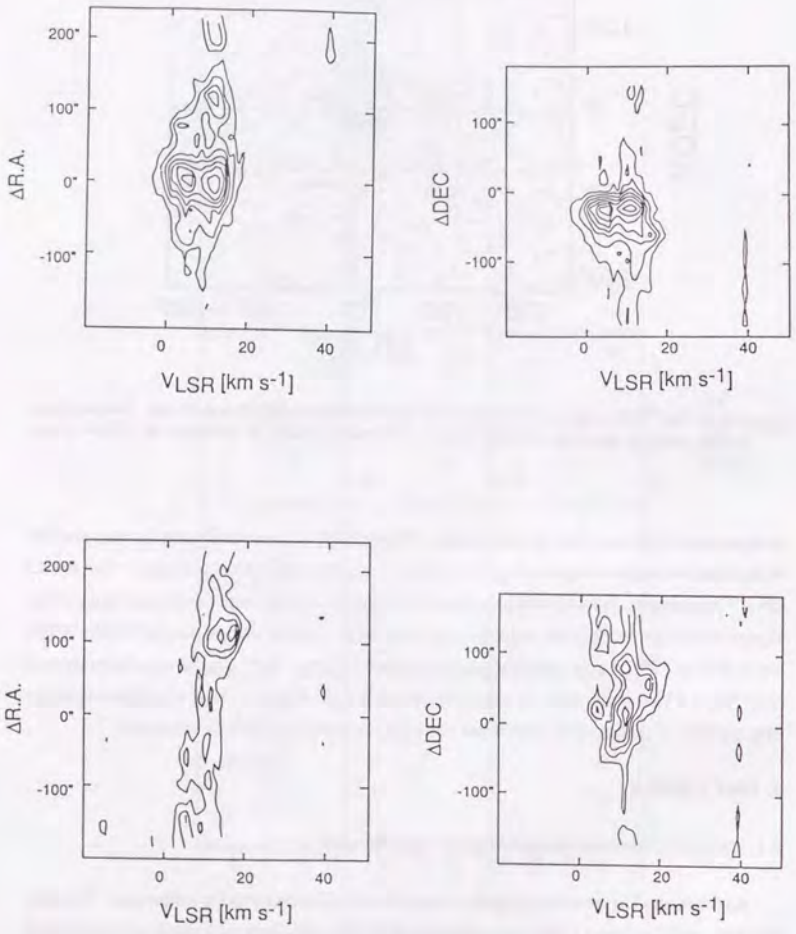

Figure 6-5: The Position Velocity Maps of ^{13}CO. (upper left) Position velocity map along right ascension through W49N. (upper right) Position velocity map along declination through W49N. (bottom left) Position velocity map along right ascension through W49S. (bottom right) Position velocity map along declination through W49S. Contour interval is 1 K.

warm and dense region with or without ultracompact H II regions. It is beacuse massive star have not formed in cores yet. Cloud-cloud collision events made massive core around W49N and around W49N small cores including W49S were also formed, in which massive stars were formed or will be formed. In these regions, several velocity components are seen and these are associated. For example, (100″, -70″) peak with a velocity of V_{LSR}~9 km s^{-1} is associated with (120″, -80″) peak with a velocity of V_{LSR}~13 km s^{-1}, and W49S is also associated with these components because (120″, -80″) peak can be seen at the velocity of 16 km s^{-1} to 20 km s^{-1}.

Elongations of the 4 km s^{-1} and 12 km s^{-1} components may be related with the formation of W49A massive core. Many dark clouds are formed by filaments and Orion Molecular Cloud also has filament structure, and cores are formed in the filament. Giant molecular clouds are assumed not to be spherical but cylindrical structure. Cylindrical giant molecular cloud is assumed to have collided each other around W49A. It is assumed that dense regions in cylindrical molecular clouds collide each other so that massive core was formed. Massive core contract with fragmentation, which grow up to protostars and massive stars. The rotational axis of "necklace" was assumed to be caused by off-center collision (*e.g.*, Keto and Lattanzio 1989).

The directions of magnetic fields of the 4 km s^{-1} component and 12 km s^{-1} component are assumed toward directions for elongations of those components. The directions of magnetic fields are probably toward 90°±3°with the strength 3.21±0.41 % (Tamura *et al.* 1994) from polarimetry of 1,100 μm observations in spite that Novak *et al.* (1989) only got the upper limit 1.1 %, which is due to larger beam and optically thick wavelength (100 μm). Kane *et al.* (1993) presented that the direction of magnetic field is 35°±12° from 1,300 μm observations. It is assumed that Tamura *et al.* (1994) sample the 4 km s^{-1} component and Kane *et al.* (1993) sample the 12 km s^{-1} component. The difference may be due to those beamwidths and observational positions.

4.2. Large Scale Star Formation in the Galaxy

Scoville, Sanders, and Clemens (1986) suggested that cloud-cloud collisions account for high rates of massive star formation. Does cloud-cloud collision frequently occur ? Sanders, Solomon, and Scoville (1985) presented 6,000 GMCs with mass of more than 10^5M$_\odot$ and a radius of grater than 10 pc in the inner Galaxy (R=2–10 kpc). Typical giant molecular cloud (GMC) has a mass of 5.8×10^5M$_\odot$ and a radius of 25 pc. The lower and the upper limits on their mass range are, respectively, 10^5M$_\odot$ and 1.8×10^6M$_\odot$, with radii in the range of 10 to 40 pc when I assumed that GMC is spherical.

The velocity dispersion of GMC is estimated by Burton and Gordon (1978) and Liszt and Burton (1983) as 4.0-4.2 km s^{-1} of one dimensional velocity (V_{1-D}). Stark (1984) estimated that molecular cloud around solar neighborhood has V_{1-D}=6.6 km s^{-1} with

masses in the range of $10^4 - 3 \times 10^5 M_\odot$. Afterward Stark and Brand (1989) also presented that the mean motion of nearby molecular clouds is drifting by ~ 4 km s^{-1} with respect to the LSR velocity. On the other hand, theoretical results of velocity dispersion of GMC (Jog and Ostriker 1988) is V_{1-D}=5–7 km s^{-1} and independent with cloud mass. I can estimated dispersion of GMC is 10 km s^{-1} of three dimensional velocity. Accordingly I can estimate collision rate (τ) of a GMC,

$$\tau = \frac{1}{n\sigma v}, \tag{6.1.}$$

where n is the GMC number density of in the unit of pc^3, σ is the cross section of GMC, which is estimated as πr^2, r is the radius of GMC, v is the velocity dispersion of GMCs. The GMC number density is estimated as

$$n = \frac{N}{2H\pi R^2}, \tag{6.2.}$$

where N is GMC numbers in the Galaxy, H is the height of Galactic disk assumed to be 75 pc, R is the radius of Galactic disk to be 10 kpc. The n is calculated 1.4×10^{-7}pc^{-3}. If the life of GMC is 1.5×10^7 *yr* (Bash, Gree, and Peters 1977), then a cloud collide an other cloud 2.8×10^{-2} times in the life time. In the Galaxy I can see 20 cloud collision events when the cloud collision last 10^6 *yr*.

Cloud-cloud collision events may more frequently take place in spiral arms. Srabyn, Güsten, and Schulz (1993) suggested that molecular clouds interact with the spiral density wave local to W49A. The two clouds of W49A, *e.g.*, the 4 km s^{-1} and 12 km s^{-1} components, are attributed to orbit crowding, where an enhanced spatial density of molecular clouds near spiral arm potential minimal (Levinson and Roberts 1981; Kwan and Valdez 1983). Local velocity field was affected by the perturbation to the local gravitational potential. Tangential velocities will be higher on the outside of spiral arm than on its interior. One molecular cloud will be accelerated inward and another cloud on the inside will be acerbated outward toward the spiral's arm potential minimum. It is assumed that the 4 km s^{-1} component move inward and the 12 km s^{-1} component move toward the spiral's arm potential minimum. Therefore the 4 km s^{-1} component might have several small clumps. The diffuse ^{13}CO emission has a velocity of $\sim$12 km s^{-1} with a velocity gradient although ^{12}CO and neutral hydrogen absorptions have a velocity of $\sim$8 km s^{-1} (*e.g.*, Radahakrishnan *et al.* 1972). The difference between the velocities of molecular gas, ^{13}CO and ^{12}CO, and neutral hydrogen gas might be due to effect of the perturbation. The relative contrast for the CO emission between the arm and interarm regions is 3 : 1 (Clemens *et al.* 1986), while contrast in the H II regions expects a (8 – 9) : 1 arm-interarm.

4.3. Arc Structure and Star formation in W49S

On the other hand, molecular cloud adjacent to W49S have an arc structure in the ^{13}CO integrated intensity map of Figure 6-1. Wood and Churchwell (1989b) observed 75 ultracompact H II region with 0.″4 resolution at 2 cm and 6 cm wavelengths using VLA. These radio continuum brightness distributions are classified into five types by morphology; cometary (20%), core-haro (16%), shell (4%), irregular or multiply peaked (17%), and spherical or unresolved (4%). G34.3+0.2, Sgr B2I, and NGC6334 F is classified into typical cometary compact H II region (Gaume and Mutel 1987). The characters of these cometary H II regions are summarized as follows (Buren *et al.* 1990); (1) an ionization front well described by a parabola, (2) surface brightness greatest at the coma, (3) limb brightening, (4) an extremely shape "upstream" edge, (5) radio recombination lines which are unusually broad.

W49S are also characterized as cometary H II regions with parabolic structures (Gaume and Mutel 1987; Dickel and Goes 1990). The line width of recombination line of are also broad, which is ΔV=39.9$\pm$1.2 km s^{-1} (Garay, Reid, and Moran 1985). This value is larger than W49N, which are typically $\Delta V \sim 30$ km s^{-1}. Especially, G34.3+ 0.2 has large velocity dispersion ΔV=48.9$\pm$3.0 km s^{-1}, and line velocity gradient is perpendicular to face of G34.3+ 0.2 (Garay, Rodoriguez, and van Gorkom 1986), which means the presence of large turbulent motions. Garay, Rodoriguez, and Gorkom (1986) suggested that large turbulence is seemed to be caused by champagne model proposed by Tenorio-Tagel (1979). On the other hand, large velocity dispersion of cometary H II region may suggest that the existence of ionized ring that is expanding or rotating as suggested on G45.07+ 0.13 and G34.3+ 0.2 (Garay, Rodoriguez, and Gorkom 1986), which is also seen in Sgr B2 H and I with ΔV=50.1$\pm$4.3 km s^{-1} and ΔV=42.2$\pm$1.9 km s^{-1}, respectively, by H76α observation (Gaume and Claussen 1990).

Wood and Churchwell (1989b) suggested another possibility of morphological difference of ultracompact H II regions. They explained that cometary ultracompact H II regions are produced by bow shocks formed around stars moving supersonically through a molecular cloud. van Buren *et al.* (1990) summarized various possibilities for formation of cometary structure; (1) supersonic Strömrgen regions; (2) distorted magnetic H II regions; (3) champagne flows; (4) distorted stellar wind bubbles; (5) moving cocoons; and (6) stellar-wind bow shocks. Since a bow shock will be present for as long as the star is moving through the molecular cloud, cometary ultracompact H II regions formed by this mechanism would have lifetimes equivalent to the length of time the star is inside a molecular cloud (Mac Low *et al.* 1991). It is consistent with a case of W49S. Because as shown in Figure 6-1 of ^{13}CO map, length of cometary structure is $\sim$6 pc toward line of sight. If runaway velocity is 10 km s^{-1}, then it takes 6×10^5 *yr*, which is less than lifetime $\lesssim 1.4 \times 10^6$ *yr* (Maeder and Meynet 1987) of an O4 star (Gaume and Mutel 1987). It is also consistent with suggestion of Wood and Churchwell (1989a) that 10%–20% of the main sequence lifetime of O and B stars is spent in embedded molecular clouds.

Moving model is, however, inconsistent with the age of compact H II regions assumed to be $\sim 10^3 - 10^4$ *yr*. The length of cometary structure of ^{13}CO is 6 pc. It takes 6×10^5 *yr* to move this distance when OB star have a moving velocity of 10 km s^{-1}. The champagne model (*e.g.*, Tenorio-Tagel 1979) may be more reasonable. The champagne phase of the evolution of H II region occurs when the ionization front of an H II region crosses a region of strong density gradients such as the boundary of a molecular cloud. The subsequent isothermal expansion of gas attain supersonic velocities of Mach 3 or more. The continuum image in champagne phase were calculated by Yorke, Tenorio-Tagle, and Bodenheimer (1983). That also have a cometary structure because the extend structure are resolved out when I make interferometric observations. The champagne flow expand to lower density regions and ionized gas is accelerated. The expanding velocity is, however, low with less than 10 km s^{-1} at the age of 10^4 *yr* (Bodenheimer, Tenorio-Tagel, and Yorke 1979). The expanding velocity become large with a range of 50–100 km s^{-1} within 10^4 *yr*, which is consistent with the age of compact H II regions. The cometary structure of ^{13}CO emission can be explained that the structure is due to the warm region heated by expanding H II region.

Dickel and Goss (1990) suggested that H II region is probably located near the front edge of the cloud because the hydorogen clolumn density derived from the H_2CO data is less than half the total hydorogen column density along this line of sight through the cloud as derived from the measurements of visual extinction by dust. The ionized gas of W49S has the velocity from 7 km s^{-1} to 11 km s^{-1} (van Gorkom *et al.* 1980; Garay, Reid, and Moran 1985), and the velocity of the molecular gas is between 11 km s^{-1} and 20 km s^{-1} (Garay, Reid, and Moran 1985; Martin-Pintado 1985b; Dickel and Goss 1990) with a core at V_{LSR}=17 km s^{-1}. From results of distribution of velocity components, molecular core with W49S was formed by the result of collision between the 17 km s^{-1} components and the 12 km s^{-1} components, or 4 km s^{-1} component.

5. CONCLUSIONS

I have observed the large scale distribution of W49A using ^{13}CO, HCO$^+$, and HCN molecular lines. Integrated intensity ^{13}CO, HCO$^+$, and HCN map has two peaks at W49N and W49S. There are several elongations. The equivelocity maps of ^{13}CO emission have three velocity components; 4 km s^{-1}, 12 km s^{-1}, and 17 km s^{-1} component. Over all velocity ranges, the peak is associated with W49N and north elongation exist. Peak at the velocity ranges of -3 km s^{-1} to 2 km s^{-1} locate at (75″, -50″). Another peak is adjacent to part of (120″, -20″) from 8 km s^{-1} to 12 km s^{-1}, and shift to (100″, -70″) at 13 km s^{-1} to 15 km s^{-1}. (100″, -70″) peak is connection with (120″, -80″) peak at the velocities of 16 km s^{-1} to 20 km s^{-1}. The contours have clumpiness at southeast part including W49S in integrated intensity map of ^{13}CO and velocity ranges from 10 km s^{-1} to 14 km s^{-1}. Southwest elongation is dominant from V_{LSR}=0 km s^{-1} to 11 km s^{-1}.

Cloud-cloud collision model is reasonable to account for these features. Interpretation of sizes of colliding clouds do not contradicted. Elongations of the 4 km s^{-1} and 12 km s^{-1} components are related with the formation of W49A massive core. Cylindrical giant molecular clouds is assumed to collide each other in the region of W49A. Dense regions in cylindrical molecular clouds collide each other so that massive core was formed. Massive core is contracting with fragmentation, which grow up to protostars and massive stars.

W49S have an arc structure in the ^{13}CO integrated intensity map. The length of cometary structure of ^{13}CO is 6 pc. It takes 6×10^5 *yr* to move this distance if OB star have a moving velocity of 10 km s^{-1}. It is, however, more reasonable that the champagne phase of the evolution of H II region occurs when the ionization front of an H II region crosses a region of strong density gradients such as the boundary of a molecular cloud. The cometary structure of ^{13}CO emission can be explained that the structure is due to the warm region heated by expanding H II region. The 17 km s^{-1} component is also associated with massive star formation in W49A as well as 4 km s^{-1} and 12 km s^{-1} components.

Chapter 7

MASSIVE STAR FORMATION AND MOLECULAR CLOUD CORES

In previous chapters, I have presented observations of the massive molecular cloud core of W49A, and have discussed distribution of gas and dust, properties of the core, and detailed structure and kinematics in the core. In this chapter, I will discuss the entire structure of W49A and star formation process in massive core summarizing this thesis.

1. MOLECULAR LINE ANALYSIS AND SPATIAL DISTRIBUTION

1.1. Spatial Distribution of Gas and Dust

In chapter 6, I presented the observations of the large scale distribution of molecular gas in W49A using ^{13}CO, HCO$^+$, and HCN molecular lines. The maps of ^{13}CO, HCO$^+$, and HCN integrated intensities shown in Figure 7-1 exhibit two peaks at W49N and W49S. The cloud at W49N has a massive core with higher density and temperature than surrounding gas. The W49S cloud has a warmer core surrounded by a colder envelope, and is less dense than the W49N cloud. The equivelocity maps of ^{13}CO emission show three velocity components; 4 km s^{-1}, 12 km s^{-1}, and 17 km s^{-1} components.

Large mass is packed in the core of the W49N cloud as suggested from C^{32}S observations (MHH). Its mass within a diameter of 50″ is estimated 3.4 $\times$ 10^4 M$_\odot$. Although there is a weak elongation to the northeast in ^{13}CO and HCO$^+$ maps, the core can be seen to be spherical as discussed in 1.2.2 of this chapter.

I presented the 450 μm and 1,100 μm continuum maps in Chapter 4 (Figure 7-3). They covered only the W49N region. The radiation originates from the thermal emission from dust and the free-free emission from ultracompact H II regions embedded in the core. The dust emission dominates at 450 μm while the free-free emission contributes ~20% of the 1,100 μm flux density. From the dust emission, I estimated the masses of the core as $5\times10^4 - 1.7 \times 10^5M_\odot$ for $\lesssim$30″ assuming that dust-to-gas ratio is 100. It is consistent with those estimated in previous works.

1.2. Molecular Line Analysis and Radial Distribution

1.2.1. Molecular Line Analysis

In Chapter 2, I presented various molecular line spectra observed forward W49A (Figure 7-4). They are classified into three groups based on their line shapes: spectra showing double peaks with a deep dip, spectra with a shallow dip, and spectra with a

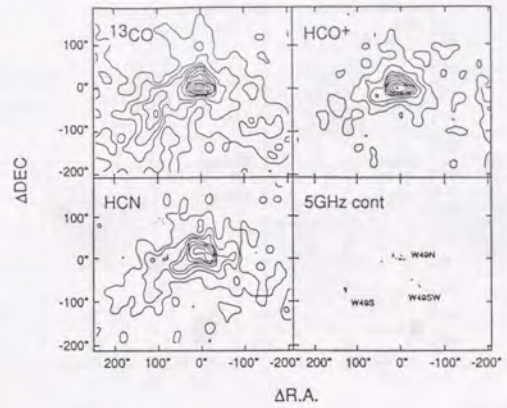

Figure 7-1: The large-area ^{13}CO, HCO$^+$, and HCN maps covering W49N and W49S. *Upper left* - The ^{13}CO (J=1-0) line intensity integrated from V_{LSR} = -10 km s^{-1} to V_{LSR} = 25 km s^{-1}. Contours are drawn at an interval of 10 K km s^{-1}. *Upper light* - The intensity of the HCO$^+$ (J=1-0) line. The velocity range of integration and the contour interval are the same as in the ^{13}CO map. *Lower left* - The integrated intensity map of HCN (J=1-0) line emission. The velocity range of integration and the contour interval are the same as in the ^{13}CO map. *Lower right* - The 23 GHz continuum image taken by Dieter et al. (1979).

single peak. They are called "deep dip lines", "shallow dip lines", and "single peak lines", respectively.

^{12}CO ($J = 1 - 0$), HCO$^+$ ($J = 1 - 0$), and HCN ($J = 1 - 0$) are classified into deep dip lines. "Deep dip lines" have a deep dip at the velocity of V_{LSR}=7.1 ±0.6 km s^{-1}. This feature has been noted by other researches. The velocities of two peaks are 2 and 11 km s^{-1}, respectively.

^{13}CO ($J = 1 - 0$), C^{18}O ($J = 1 - 0$), H^{13}CO$^+$ ($J = 1 - 0$), and C^{34}S ($J = 2 - 1$) are shallow dip lines. "Shallow dip lines" have a shallower dip than that of "deep dip lines" at the at the velocity of V_{LSR}=7.9 ±0.7 km s^{-1}. I also classify C^{34}S ($J = 1 - 0$) and SO_2 into the shallow dip lines because they can be regarded as a shallow dip case with much weaker blueshifted peaks. C^{32}S($J = 2 - 1$) (Nyman 1984) and HCN (Nyman and Miller 1989) are also classified into this type. SiO and SO are single peak lines.

The deep dip lines are transitions that can be easily optically thick. This suggests that the dip at V_{LSR}~7 km s^{-1} is due to self-absorption by cold foreground gas. The present situation is, however, not so straightforward because optically thin shallow dip lines also have a dip at the similar velocity. I discussed this problem in the previous paper (MHH) and gave more detailed discussion in Chapter 2 on the basis of presently available data.

The difference of the optical depth determine the different depth of dip. Phillips *et al.* (1981) compared the $J = 1 - 0$ and $J = 2 - 1$ emissions of CO and found that the

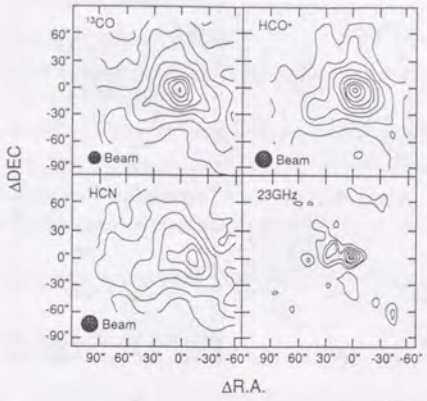

Figure 7-2: The ^{13}CO, HCO$^+$, and HCN maps of the massive molecular cloud core around W49N. *Upper left* - The ^{13}CO (J=1-0) line intensity integrated from V_{LSR} = -5 km s^{-1} to V_{LSR} = 20 km s^{-1}. Contours are drawn at an interval of 10 K km s^{-1}. *Upper right* - The HCO$^+$ (J=1-0) line intensity. The velocity range of integration and the contour interval are the same as in the ^{13}CO map. *Lower left* - The HCN (J=1-0) line intensity. The velocity range of integration and the contour interval are the same as in the ^{13}CO map. *Lower right* - The 23 GHz continuum image taken by Dieter et al. (1979).

CO emission is optically thick. They claimed that the lines of ^{13}CO do not have the same shape and conclude that the dip at 7 km s^{-1} is due to optically thick absorption by foreground gas. Bieging, Wilson, and Downes (1982) pointed out the similarity of the spatial distribution of two velocity components of H_2CO, which offers another support for the idea that the dip in CO profile is caused by self-absorption. Nyman (1983; 1984) and this work observed various molecular lines toward W49A and found that H^{13}CO$^+$ does not show the dip prominent in the profile of main isotope. This may indicate that the dip observed in the lines other than H^{13}CO$^+$ is caused by optically thick foreground gas. MHH estimated the optical depth of foreground CO gas to be ~3. Boreiko and Betz (1990) presented the $J = 9 - 8$ emission of CO. There is no doubt that the cold, less dense molecular gas exists in the foreground of W49A and it caused the self-absorption line in the "deep dip lines".

The shallow dip profiles are observed in lines that are believed to be optically thin. All the observed optically thin line profiles, except for the shock indicators, have double peaks with a shallow dip. On the contrary to the case for deep dip lines, the dips are shallow enough such that they can naturally be understood as a result of overlapping two velocity components. Examining the three shallow dip lines, ^{13}CO ($J = 1 - 0$), C^{18}O ($J = 1 - 0$), H^{13}CO$^+$ ($J = 1 - 0$) with high signal to noise ratio, I noticed that the peak

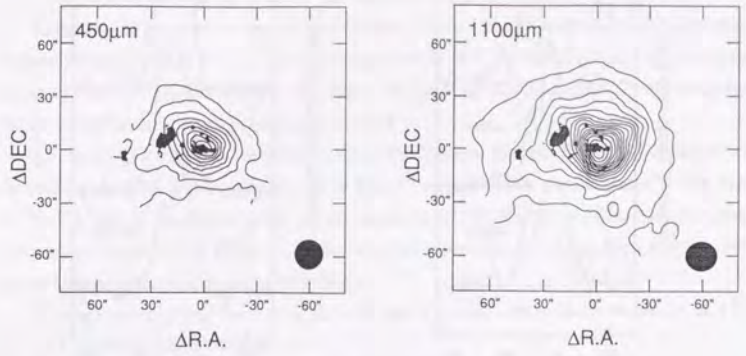

Figure 7-3: The 450 μm and 1100 μm continuum maps of the W49A massive core superposed on the 5 GHz continuum image taken by Dickel et al. (1990). *Left* - The map of the 450 μm continuum emission. Contours are drawn at an interval of 50 Jy/beam. The beamsize is shown in the lower right corner. *Right* - The map of the 1100 μm continuum emission. Contours are drawn at an interval of 2 Jy/beam.

velocities are remarkably constant among the lines, i.e., 4.2±0.3 km s^{-1} and 10.6±0.2 km s^{-1}, whereas the dip velocities varies more. Comparison of these three line profiles demonstrates that the dip velocity varies as the relative strength of the blue- and redshifted peaks changes; the dip is located just at the center of the two peaks for ^{13}CO ($J = 1 - 0$) and C^{18}O ($J = 1 - 0$) that have comparable blue- and redshifted peak intensity, while the dip is located relatively at redshifted velocity in the case of H^{13}CO$^+$ ($J = 1 - 0$) that has much stronger blueshifted peak intensity. The C^{34}S lines show a tendency opposite to H^{13}CO$^+$ that the redshifted peak feature is stronger and the shallow dip is blueshifted. I can naturally understand these facts when the two velocity components exist in the W49A cloud core with their corresponding line intensities different from one another reflecting the difference in their physical and chemical conditions.

An important point is that the self-absorption and the two velocity components inside the massive core of W49A do coexist. MHH showed the self-absorption is not significant for the CS emission line and the two peaks seen in the CS ($J = 1 - 0$) profiles correspond to two dense molecular clouds although the 8 km s^{-1} dip seen in the CO profile is evidently due to self-absorption. There is actually an increasing number of evidence that shows that at least two clouds exist within the W49A core as discussed in Chapter 3 and 6. They are listed as follows:

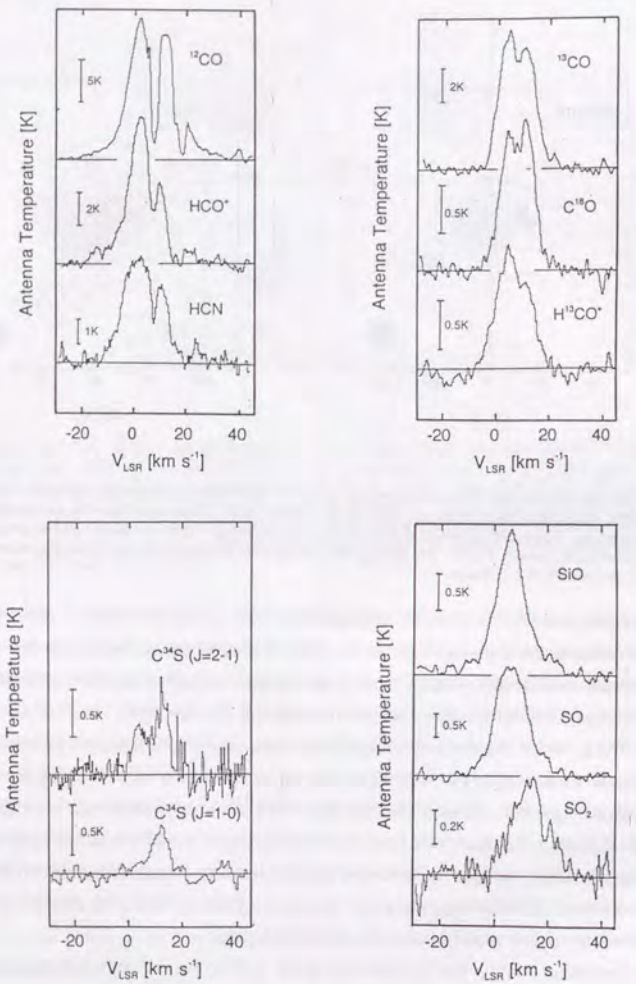

Figure 7-4: Line profiles toward W49A in various molecular lines that are classified into three groups, i.e., "deep dip lines", "shallow dip lines", and "single peak lines". *Upper left* - The deep dip lines: ^{12}CO (J=1-0), HCO$^+$ (J=1-0), and HCN (J=1-0). *Upper right* - The shallow dip lines: ^{13}CO (J=1-0), C^{18}O (J=1-0), and H^{13}CO$^+$ (J=1-0). *Lower left* - The shallow dip lines with the higher velocity (12 km s^{-1}) peak much stronger than the lower velocity (4 km s^{-1}) peak. *Lower right* - The single peak lines: SiO (J=2-1), SO (2_1-1_1), and SO_2 ($8_{3,5}$-$9_{2,8}$).

1. The C^{34}S emission, which is optically thin (τ <0.3), has a peak at 12 km s^{-1}, where a stronger peak of the CS emission exists, and not around 8 km s^{-1} as expected from the idea that the CS dip is due to self-absorption. Its asymmetry is caused by the prominent blue wing corresponding the 4 km s^{-1} component of the main isotope of CS.

2. the H_2CO absorption maximum often lies at the velocity where the self-absorption feature in the CO ($J = 1 - 0$) line. In the case of W49A, however, the H_2CO absorption maximum is at V_{LSR}=12 km s^{-1} and not at V_{LSR}=8 km s^{-1} suggesting that the optical depth of the absorbing gas is smaller at 8 km s^{-1}.

3. The H_2CO maps of Goss and Tilanus (1985) show that the 12 km s^{-1} cloud covers the entire complex sources, while the 4 km s^{-1} absorption is concentrated to the west of W49A and is prominent only in the direction of W49N. This difference in spatial distribution suggests the presence of the two absorbing clouds: one in front and the other in the side or back of the continuum source.

4. The optically thin lines such as C_2H lines (Nyman 1984) have two peaks at 4 km s^{-1} and 12 km s^{-1}, and not at 8 km s^{-1}.

5. MHH and this work presented the distribution of "shallow dip lines" emission, which is slightly different between the two peak velocities. The two distributions should be similar if the dip were caused simply by the self-absorption.

6. The carbon recombination line C166α has two peaks at 5 km s^{-1} and 14 km s^{-1} (Pankonin, Thomasson, and Barsuhn 1977). This indicates that there are two CII regions with different radial velocities.

Thermal emissions of SiO and SO have so far been detected in highly excited regions such as in the Orion hot core or in regions of molecular clouds interacting with outflows (Downes *et al.* 1982; Wright *et al.* 1983). There is an increasing number of evidence that such molecules come out from dust grains when grains are exposed to shocks. It is interesting that these shock indicators show different characteristics in their line profiles compared to the deep dip and shallow dip lines; their peak velocities are ~6 km s^{-1} which is between the two peaks of the lines with dips. This means that star formation in W49A is taking place at the velocity between the two velocity components.

1.2.2. Radial Distribution of Molecular Lines

Because W49A molecular cloud has considerable symmetry with respect to the mapping center under the spatial resolutions and coverages of the single-dish observations with the 45-m telescope (Chapter 3), I examined the radial distributions of the molecular line intensities by assuming circular symmetry (Figure 7-2). The radial distributions of ^{13}CO ($J = 1 - 0$), C^{18}O ($J = 1 - 0$), HCO$^+$ ($J = 1 - 0$), H^{13}CO$^+$ ($J = 1 - 0$), HCN ($J = 1 - 0$), H^{13}CN ($J = 1 - 0$), HC^{15}N ($J = 1 - 0$), C^{34}S ($J = 2 - 1$), C^{34}S ($J = 1 - 0$), H51α, SiO ($v = 0$, $J = 2 - 1$), SO ($J = 2_1 - 1_1$), SO_2 ($J = 8_{3,5} - 9_{2,8}$), and SO_2

(J =$18_{4,14} - 17_{5,3}$) are presented in Figure 7-5. The intensities decrease monotonically from the center to outward with moderate dispersion. This enables to make a power law fit to each radial distribution.

The optically thin lines with lower critical densities for collisional excitation such as ^{13}CO, and C^{18}O have relatively flat distribution with the power law index close to 1. The optically thick lines HCO$^+$ and HCN also show similar flat radial profiles. The optically thin lines with higher critical densities such as H^{13}CO$^+$ and H^{13}CN tend to exhibit steeper decrease with the power law index close to 1.5. The single peak lines SiO and SO show the steepest decrease, suggesting that these line emissions are localized to a compact region comparable to or smaller than the telescope beam at the center of the W49A molecular cloud.

1.3. Interpretation of Spectra and the Structure of W49A

The following conclusions have been drawn from the analyses of the single-dish data:

1. There is a core with two velocity components at 4 km s^{-1} and 12 km s^{-1}. The core is massive and gravitationally unstable.

2. At the velocity between the two cloud velocities, star forming activities is vigorous.

3. Star formation is occurring in the core, which was possibly formed as a result of interaction between the two clouds.

2. THE STRUCTURE OF MASSIVE AND UNSTABLE CORE

2.1. CS Observations

In Chapter 5, I presented the interferometric observations with high angular resolution that revealed the detailed internal structure of the massive core. The 4 km s^{-1} component of CS (J = 1 − 0) emission has compact distribution surrounding the ultracompact H II region component g, and the 12 km s^{-1} component of CS emission encircles the the 4 km s^{-1} component (Figure 7-6). These features are consistent with the clumps identified by Serabyn, Güsten, and Schulz (1993), and further resolve their structure.

The detailed shape and kinematics of the CS emission strongly suggest that the two clouds have collided in the W49A core. The two clouds have similar mass, but the core seen at 4 km s^{-1}is more compact and dense. The shell structure appears to be formed in the course of cloud-cloud collision, and the CS emission of our observations sample interface and dense regions of the colliding clouds. The 4 km s^{-1}cloud formed a massive core after the collision which is now contracting by self-gravity.

2.2. SiO Observations

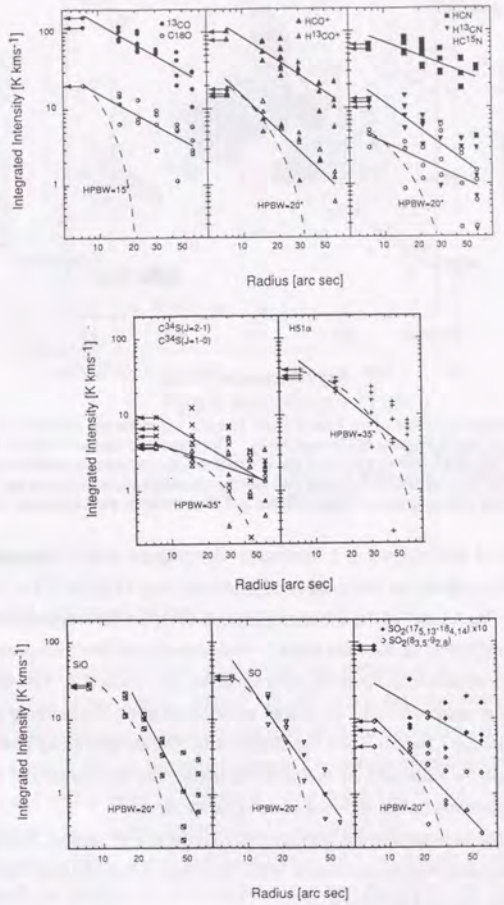

Figure 7-5: Radial distribution of the intensities of various molecular and atomic lines around W49A. *Upper* - Radial distribution of the ^{13}CO (J=1-0), C^{18}O (J=1-0), HCO$^+$ (J=1-0), H^{13}CO$^+$ (J=1-0), HCN (J=1-0), H^{13}CN (J=1-0), and HC^{15}N (J=1-0) emission. Straight lines are eye fits to the data and the Gaussian beam patterns (i.e., responses to a point source) are shown by dashed curves. *Middle* - Radial distribution of the C^{34}S (J=2-1), C^{34}S (J=1-0), and H51α emission. *Lower* - Radial distribution of the SiO (J=2-1), SO (2_1-1_1), SO_2 ($17_{5,3}$-$18_{4,14}$), and SO_2 ($8_{3,5}$-$9_{2,8}$) emission.

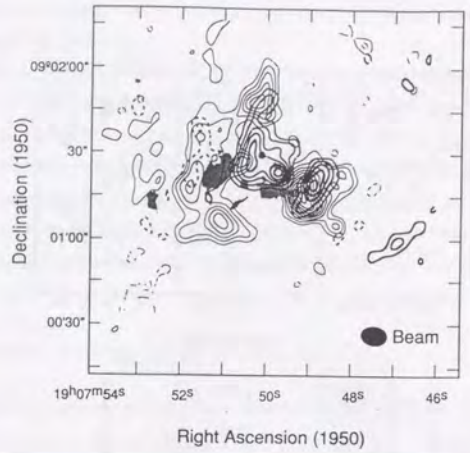

Figure 7-6: The detailed structure of the 4-km s^{-1} and 12-km s^{-1} components observed in the CS (J=1-0) emission with the Nobeyama Millimeter Array. Thick and thin contours represent the emission at V_{LSR} = 3.6 km s^{-1} and V_{LSR} = 14.1 km s^{-1}, respectively. Contours are drawn from 0.30 Jy/beam at an interval of 0.15 Jy/beam, and the synthesized beam is shown in the lower right corner. The 5 GHz continuum image (Dickel and Goss 1990) is shown shaded.

Distribution of SiO ($J = 2 - 1$)emission is compact and is elongated along the ultracompact H II regions in the integrated intensity map (Figure 7-7). The peak is at the center of the "necklace" of the ultracompact and compact H II regions. Another strong emission is at southwest of the "necklace". The velocity of the SiO peak in the center of "necklace" corresponds to the peak velocity at $V_{LSR}\sim$ 6 km s^{-1}. The another peak of strong emission at southwest of "necklace" may correspond to the other peak found in the single dish data in Chapter 2 and the H_2CO data (Dickel and Goss 1990). In contrast to a relatively narrow linewidth of the SiO emission from the center of "necklace", the emission from southwest peak shows a wide velocity range.

The SiO emission is sometimes regarded as an indicator of shocks. SiO emission may arise from the shocked region associated with the cloud-cloud collision or the dynamical impact due to star forming activities.

2.3. Cloud-Cloud Collision

Figure 7-8 shows the CS distribution of 4 km s^{-1} and 12 km s^{-1} components superposed on the integrated intensity of SiO map. The SiO emission is detected from regions between the 4 km s^{-1} and 12 km s^{-1} components of CS emission. This further supports the model that the 4 km s^{-1} and 12 km s^{-1} clouds collided and star formation in W49A started at the

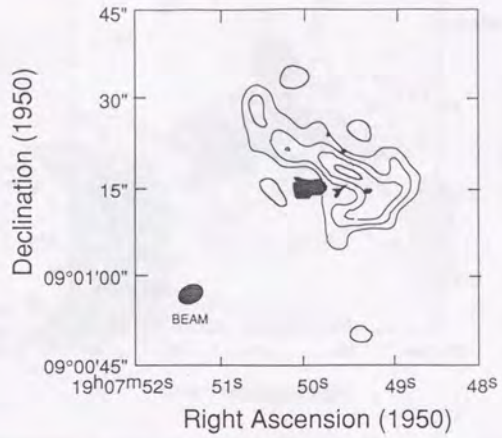

Figure 7-7: The interferometric image of the SiO (J=2-1) line intensity integrated from V_{LSR} = -1.4 km s^{-1} to V_{LSR} = 15.8 km s^{-1}. Contours are drawn from 0.2 Jy/beam at an interval of 0.1 Jy/beam, and the synthesized beam is shown in the lower left corner.

velocity in between.

3. STAR FORMATION IN W49A

The above observational results imply that star formation in W49A occurs not by a simple trigger but in two stages. Figure 7-9 shows a schematic model of W49A. Two clouds collide, and a massive core is formed between the two clouds with the mean velocity. SiO emission arises from star forming region at the interface between the two clouds. In addition, cold gas with a velocity of 8 km s^{-1} lies in front of W49A. I can not determine where cold gas is at envelope or independent foreground gas.

Hasegawa *et al.* (1994) showed clear evidence for a large-scale cloud collision event, which triggered the intense star formation in the Sgr B2 molecular cloud complex. It is, however, difficult to imagine that this collision has directly triggered the burst of star formation. Rather, two stages, *i.e.*, formation of the massive dense cores during the collision event and subsequent massive star formation in them, may be required (Lis *et al.* 1991).

How were massive core of W49A and massive stars formed? Habe and Ohta (1992) presented numerical simulations of collisions of two clouds with different size. Strong shock waves occur in both colliding clouds and afterwards, the shock waves propagate into

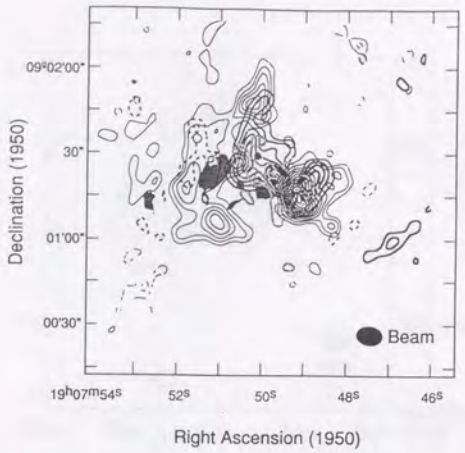

Figure 7-8: The detailed comparison of the spatial distribution of the CS (J=1-0) emission [thick and thin solid contours; adapted from Figure 7-6] and that of the SiO (J=2-1) emission [gray contours; adapted from Figure 7-7]. The "single peak" SiO emission arises from the interface between the two velocity components of the "deep dip" CS (J=1-0) line emission. The 5 GHz continuum image (Dickel and Goss 1990) is shown shaded.

both clouds along the collision axis toward outer sides. The density of postshock gas in the small cloud increase and have a disklike shape. On the other hand, in the large cloud the shock wave becomes a bow shock. Afterward the inner potion of small cloud contract due to self-gravity toward the center and the density increase exponentially. Contracting clouds might fragment into several pieces if it has a rotation as several numerical calculations show. These fragments, possibly with strong magnetic field and rotation, collapse by self-gravity to form stars.

As Shu, Adams, and Lizano (1987) suggested, self-gravity of molecular fragment with a "supercritical" mass can overwhelm the magnetic support even if the fields remain frozen in the molecular gas. Cloud contraction under these circumstances efficiently form protostars with high mass nearly isothermally even if core is heating. The protostar grows hydrostatically by accreting matter from infalling gas and dust. Kelvin-Helmholz time scale of massive stars are shorter than infall time scale. When mass of star is 30 $M_\odot$, τ_k is $\sim 10^4 yr$, and when mass of star is 50 $M_\odot$, τ_k is $\sim 3 \times 10^3$ yr. Mass of the star forming core is important in determining the mass of a forming star. Large cloud mass is in need to form massive stars as Nakano, Hasegawa, and Norman (1994) showed. The fragments form a cluster of compact H II regions.

The above scenario may explain the coherent formation of many massive stars in

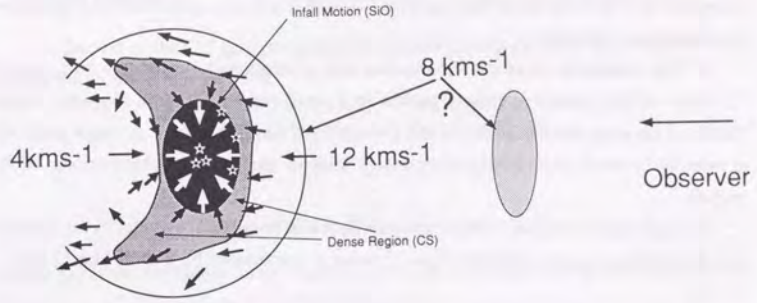

Figure 7-9: Schematic picture of the W49A complex seen from its side.

W49A, which can be called localized starburst. Other region of localized starburst in the Galaxy are Sgr B2 and W51A.

Miyawaki *et al.* (1994) noted a large shear velocity field in the massive core of Sgr B2, another region of localized starburst, from CS ($J = 1 - 0$) observations at NMA. Ultracompact H II regions are situated at this region of larger velocity shear. Around Sgr B2(M), massive core and diffuse halo coexist with the same velocity reminiscent of the coexistence of the massive core and the foreground self-absorbing gas in W49A. This common structure might have been formed in the process core formation in a cloud collision event.

Other region of localized starburst, W51A, also show hints that suggest that formation of massive stars has been triggered by cloud-cloud collision. Two velocity components are seen and they appear to have collided with each other. W51A also has a massive core with a mass comparable to W49A, and luminous infrared sources are observed in it. Ultracompact H II regions are observed at 2.2 μm (Little *et al.* 1989). The cluster of massive stars are located at the edge of massive core and illuminates it. This can be understood if massive stars was formed not only in the massive core but also the interface of colliding clouds in W51A.

4. CONCLUDING REMARKS

I have observed the W49A molecular cloud complex, which is the most luminous star-forming region in our Galaxy, at millimeter and submillimeter waves. The main results are summarized as follows.

1. Analyses of molecular lines show that there are two velocity components in the W49A molecular cloud. The high excitation lines arise at the velocity between two components. Optically thick lines are observed with a self-absorption feature arising from the foreground cold gas.

2. The molecular cloud core is massive and gravitationally unstable with a mass of (3–10)$\times$ $10^4 M_\odot$, which is closely packed in a small region 3.0 pc in diameter. In the center of the core, there is an active and compact star forming region. A single peak with a velocity between two velocity components arise in spectral lines characteristic of this region.

3. High angular resolution observations with NMA reveal that two velocity components are distributed in a way that the 4 km s^{-1} cloud is surrounded by a shell-like 12 km s^{-1} cloud.

4. This feature strongly supports the scenario in which two molecular clouds collided with each other, and a massive core formed in which a dozen of massive stars are formed.

5. W49A is regarded as a region of localized starburst. Sgr B2 and W51A are similar in nature; Cloud collisions may have played an essential role in triggering the localized starburst in these regions.

APPENDIX

APPENDIX 1

EXCITATION TEMPERATURE, OPTICAL DEPTH, AND MASS

distribution of the CO gas, we adopt the simplest configuration of an isothermal slab, so that the solution may be used,

$$T_b(s) = T_b(0)exp(-\tau_\nu) + T(1 - exp(-\tau_\nu), \qquad (A1.1.)$$

or

$$T_b = T_0(F(T_0) - F(T_{BG})(1 - exp(-\tau_\nu)), \qquad (A1.2.)$$

where T_{ex} is the excitation temperature, T_{BG}=2.7 K is the cosmic background radiation T_0 is $h\nu/k$, and F(T)= 1 / [exp(-T_0/T_{ex})-1].

The procedure outlined by Dickman (1978) is applicable if the following assumption are valid that all molecules along the line-of-sight possess a uniform excitation temperature in the $J = 1 - 0$ transition. The different isotopic species have the same excitation temperatures which are equal to the kinetic temperature of the gas, and the optical depth in the ^{12}CO line is large. Then the peak excitation temperature can be determined from the measured $T_{^{12}CO}$,

$$T_{ex} = 5.532ln\left(1 + \frac{5.532}{T_{^{12}CO} - 0.8182}\right)^{-1}. \qquad (A1.3.)$$

The optical depth of the ^{13}CO($J = 1 - 0$) line is obtained by solving (A1.2.) for

$$\tau_{^{13}CO} = -ln\left(1 - \frac{T_{^{13}CO}}{5.289}\left(exp\left(-\frac{5.289}{T_{ex}} - 1\right)^{-1} - 0.1642\right)^{-1}\right), \qquad (A1.4.)$$

where we use

$$\tau_{^{13}CO}\Delta V = \int \tau(V)dV. \qquad (A1.5.)$$

The column density is related to $\tau_{^{13}CO}$ by

$$\int \tau(V)dV = \frac{c^2}{8\pi\nu^2}\frac{1}{g_1}\frac{g_2}{g_1}A_J[1 - exp(-T_{^{13}CO}/T_{ex})]\frac{N(^{13}CO)}{Q}, \qquad (A1.6.)$$

where A_J is the Einstein transition probability of the $J = 1 - 0$ transition of ^{13}CO, A_J=7.4 $\times$ $10^{-8}$$s^{-1}$ and Q is the partition function of ^{13}CO, Q=2T_{ex}/$T_{^{13}CO}$.

We finally obtained the column density of ^{13}CO,

$$N(^{13}CO) = 2.42 \times 10^{14}\frac{\tau_{13}\Delta V_{13}T_{ex}}{1 - exp(-5.289/T_{ex})} \quad (cm^{-2}) \qquad (A1.7.)$$

where τ_{13} is the maximum optical depth of ^{13}CO line from Table II-4 τ_{13} is 0.34, ΔV_{13} is the line width (FWHM) of ^{13}CO in km s^{-1}, and T_{ex} is the excitation temperature estimated from the ^{12}CO antenna temperature in K, which is assumed to be equal to kinetic temperature and dust temperature.

APPENDIX 2

AGE OF ULTRACOMPACT HII REGION

Churchwell (1989b) suggested that if density of the ambient medium is $\sim 10^5$ cm^{-3} the initial expansion will take only a few years, which is for all practical purpose, and unobservable. When an O star embedded in a molecular cloud core begins producing UV photons, an I-front will form and expand rapidly outward to fill an initial Strömgen sphere. The velocity of the ionization front (I-Front) is very large at first, but because a greater and greater volume must be kept ionized as radius of the I-front increase, which is short-lived. If n_0 is the density of ambient medium (10^5 cm^{-3}) and β is recombination coefficient ($\sim 3 \times 10^{-13}\ cm^3 s^{-1}$), then sound speed spend in a time,

$$c_i \sim 4(n_0\beta)^{-1} \sim 13\ kms^{-1}. \qquad (A2.1.)$$

The radius, r_i of the initial Strömgen sphere is given by

$$r_i = \left(\frac{3N_c^*}{4\pi n_e n_H \beta}\right)^{\frac{1}{3}} \qquad (A2.2.)$$

where N_c^* is Lyman continuum photon flux, and n_e is electron density. Typical ultracompact H II region without dust have ~0.05 pc (Wood and Churchwell 1989b). Ultracompact H II regions in W49N (Dreher *et al.* 1984) are consistent with those ultracompact H II region except component g, which has complicated structure and are assumed that clusters of ultracompact H II region or complicated interaction between H II region and molecular cloud.

If dust absorbs 90 % of the UV photons (f_d=0.9), then r_i will be reduced by a factor of $(1 - f_d)^{\frac{1}{3}}$=0.46. We can expect these objects to have initial Strömgren radii of ~0.023 pc, we will assume f_d=0.9. When the cold dense neutral molecular gas with temperature T_0 and particle density n_0 is ionized, its pressure increase dynamically. Unless other force act on it, the ionized gas will expand to reach pressure equilibrium is reached. We will have

$$P_i = 2n_f kT_e = n_0 kT_o = P_0, \qquad (A2.3.)$$

where n_f is the final density of the H II region with electron temperature T_e. The factor of two accounts for the fact the ionized gas has approximately equal numbers of electrons

and photons when pressure equilibrium is reached, the initial and final density of the H II region must satisfy

$$n_f = \frac{2T_e}{T_0} n_0. \qquad (A2.4.)$$

The radii of the initial and final Strömrgen sphere will be related by

$$r_f = \left(\frac{2T_e}{T_0}\right)^{\frac{3}{3}} r_i. \qquad (A2.5.)$$

For typical value T_e=10^4 K, T_0=45 K (Harvey, Campbell and Hoffmann 1977), we find r_f=58. Using a strong shock approximation, the radius of the H II region as a function of this follows,

$$r(t) = r_i\left(\frac{1 + 7c_i t}{4r_i}\right)^{\frac{4}{7}}, \qquad (A2.6.)$$

where c_i is the sound speed in the ionized gas (~13 km s^{-1}). From this and the condition that r_f=58r_i predicted that it will take $\sim 1.6 \times 10^6\ yr$ for H II region to reach pressure equilibrium. This is approximately the main-sequence lifetime of an O6 star with mass loss ($2.4 \times 10^6\ yr$; Maeder and Meynet 1987). At equilibrium it will be ~1.3 pc in diameter within the lifetime of stars. Most of massive core will be ionized by OB stars in their life time.

When negative feedback work, mass accretion, growth time of expanding of H II region is later than no negative feedback.

APPENDIX 3

UPPER MASS OF STARS IN MASSIVE CORE

The star formation in the W49A molecular cloud complex is different from what we observe in the neighborhood as Orion region. W49N contains over dozen of OB stars in a diameter of 3 pc. The total mass of these massive stars are estimated about 500 $M_\odot$. Age of compact H II regions in Sgr B2(M) is assumed to be $10^3 - 10^4\ yr$ (Dreher *et al.* 1984). This gives a current star formation rate is a order of 0.1 $M_\odot yr^{-1}$. This rate of star formation will exhausts the gas in the core to form stars in $10^3 - 10^4 yr$ assuming star forming efficiency of 1% – 10% (MHH). Absence of supernova remnant means that a highly synchronized star formation process start from the beginning of a certain event.

As mentioned about Sgr B2 (Hasegawa *et al.* 1994) shows clear evidence for a large-scale cloud collision event. It is difficult to imagine, however, that this collision has directly triggered the burst of star formation. Rather, two stages, i.e., formation of the massive dense cores during the collision event and subsequent massive star formation, may be required (Lis *et al.* 1991).

Our high resolution image reveals that the massive core of dense molecular gas associated with one of colliding molecular clouds. Massive core is assumed to be composed

of several supercritical fragments. As Shu, Adams, and Lizano (1987) suggested in supercritical case, self-gravity of molecular fragment can overwhelm the magnetic support even if the fields remain frozen in molecular cloud. A cloud with supercritical mass will suffer relatively rapid contraction and compress the embedded magnetic fields well. Cloud contraction under these circumstances efficiently form protostars with high mass nearly isothermally even if core is heating. The protostar grows hydrostatically by accreting matter from infalling gas and dust. For massive star Kelvin-Helmholz time scale will be shorter than infall time scale. If radiation pressure is negligible, Kelvin-Helmholz time is obtained as followed,

$$\tau_k = \frac{GM^2}{RL} \sim 10^5 \left(\frac{10M_\odot}{M}\right)^2 yr, \qquad (A3.1.)$$

when mass of star is 30 $M_\odot$, τ_k is $\sim 10^4 yr$, and when mass of star is 50 $M_\odot$, τ_k is $\sim 3\times10^3 yr$.

Massive star will reach the main sequence while still gaining mass from the infalling envelope though the radiation pressure acting on dust grains may become large enough to halt the infall or the infall may be nonspherical owing to rotation. Mass accretion rate in massive core is derived as follows,

$$\dot{M} \sim \frac{c_s}{G} \sim 10^{-1} \left(\frac{n_{H_2}}{10^5 cm^{-3}}\right)^{-\frac{1}{3}} \left(\frac{B}{3mG}\right)^3 M_\odot yr^{-1}, \qquad (A3.2.)$$

where n_{H_2} is the density of hydrogen molecule and B is magnetic field, which is derived from OH masers (Gaume and Mutel 1987), these value is gives c_s is the sound speed $\sim$ 10 km s^{-1}. On the other hand, upper mass of star is estimated from mass accretion rate as equation (A3.3.).

$$M \sim 5 \left(\frac{\dot{M}}{10^{-5} M_\odot yr^{-1}}\right)^{\frac{1}{3}} \sim 100 M_\odot, \qquad (A3.3.)$$

The ages of compact H II regions of W49A are assumed to be within 10^4 yr though age of ultracompact H II region have uncertainty that expansion of H II region may be restricted by infall materials (Wood and Churchwell 1989b). As mentioned above, it is not surpassing that compact H II regions were formed on the same time and star formation in W49A took place in short time scale.

REFERENCES

Aannestad, P. A. 1975, ApJ, **200**, 30.

Akabane, K., and Kerr, F. J. 1965, *Australian J. Phys.* , **18**, 91.

Akabane, K., Sofue, Y., Hirabayashi, H., and Inoue, M. 1989, PASJ, **41**, 809.

Arquilla, R., and Goldsmith, P. F. 1985, ApJ, **297**, 436.

Bachiller, R. B., Guilloteau, S., and Kahane, C. 1987, A&A, **173**, 324.

Bachiller, R., Martin-Pintado, J., and Fuente, A. 1991, A&A, **243**, L21.

Ball, J. A., Gottlieb, C. A., Lilley, A. E., and Radford, H. E. 1970, ApJ, **162**, L203.

Bash, F. N., Gree, E., and Peters, W. L., 1977, ApJ, **217**, 464.

Becklin, E. E., Neugebauer, G., and Wynn-Williams, C. G. 1973, *Ap. Letters* , **13**, 147.

Beichman, C. A., Myers, P. C., Emerson, J. P., Harris, S., Mathieu, R. 1986, ApJ, **307**, 337.

Benson, J. M., and Johnston, K. J. 1984, ApJ, **277**, 181.

Bodenheimer, P., Tnorio-Tagel, G., and Yorke, H. W., ApJ, **233**, 85.

Boreiko, R. T., and Betz, A. L. 1991, ApJ, **369**, 382.

Brown, R. L., and Broderick, J. J. 1973, ApJ, **181**, 125.

Burke, B. F., and Wilson, T. S. 1967, ApJ, **150**, L13.

Burke, J. R., and Hollenbach, D. J. 1983, ApJ, **265**, 223.

Burton, W. B. and Gordon, M. A., 1978, A&A, **63**, 7.

Chini, R., Kreysa, E., Mezger, P. G. and Gemünd, H. -P., 1984, A&A, **137**, 117.

Chini, R., Kreysa, E., Mezger, P. G. and Gemünd, H. -P., 1986a, A&A, **154**, L8.

Chini, R., Kreysa, E., Mezger, P. G. and Gemünd, H. -P., 1986b, A&A, **157**, L1.

Chini, R., Krügel, E., and Kreysa, E., 1986, A&A, **167**, 315.

Clemens, D. P., Sanders, D. B., Scoville, N. Z., and Solomon, P. M. 1986, ApJS, **60**, 297.

Cox, P., Krügel, E., and Mezger, P. G. 1986, A&A, **155**, 380.

Cox, P., Güsten, R., and Henkel, C. 1988, A&A, **206**, 106.

Cox, P.,, and Mezger, P. G. 1989, *Astron. Astrophys. Rev.*, **1**, 49.

Dame, T. M., and Thaddus, P. 1985, ApJ, **297**, 751.

Dame, T. M., Elmegreen, B. G., Cohen, R.S., and Thaddus, P., 1986, ApJ, **305**, 892.

Day, K. 1976, ApJ, **210**, 614.

Dickel, H. R., and Goss W. M. 1990, ApJ, **351**, 189.

Dickel, H. R., and Auer, L. H. 1994, ApJ, in press.

Colloquium 140 Astronomy with Millimeter and Submillimeter Wave Interferometry p.253.

Dickman, R. L. 1978 ApJS, **37**, 407.

Dieter, N. H., Welch, W. J., and Wright, M. C. H. 1979, ApJ, **230**, 768.

Downes, D., and Wilson, T. L. 1967, A&A, **34**, 133.

Downes, D., Genzel, R., Hjalmarson, A., Nyman, L. Å., and Ronnang, B. 1982, ApJ, **252**, L29.

Dreher, J. W., Johnston, K. J., Welch, W. J., and Walker, R. C. 1984, ApJ, **283**, 632.

Dulley, W. W., and Boehlau, E. 1986, MNRAS, **221**, 659.

Efanov, V. A., Kislyaknov, G. A., Kuznetsov, I. V., Moissev, I. G., and Troitskii, A. V. 1975, *Soviet Astro.*, **18**, 410.

Elmegreen, B. G., and Lada, C. J. 1977, ApJ, **214**, 725.

Erikson, E. F., and Tokunaga, A. T. 1980, ApJ, **238**, 596.

Fiebig, D., and Güsten, R. 1989, A&A, **214**, 333.

Forster, J. R., Goss, W. M., Wilson, T. L., Downes, D., and Dickel, H. R. 1980, A&A, **84**, L1.

Frerking, M. A., Langer, W., and Wilson, R. W. 1987, ApJ, **313**, 320.

321.

Gardner, F. F., and Martin-Pintado, J. 1983, A&A, **121**, 265.

Garay, G., Reid, M.J., and Moran, J. M. 1985, ApJ, **289**, 681.

Garay, G., Rodoriguez, L. F., and van Gorkom, J. H. ApJ, **309**, 553.

Gaume, R. A., and Mutel, R. L. 1987, ApJS, **65**, 193.

Gaume, R. A., and Claussen, M. J. 1990, ApJ, **351**, 538.

Gear, W. K., Robson, E. I., and Griffin, M. J., 1988, MNRAS, **231**, 55p.

ed. R. S. Roger and P. E. Dewdney (Dordrecht: Reidel), p251.

Genzel, R., Reid, M. J., Moran, J. M., and Downes, D. 1981, ApJ, **244**, 884.

Genzel, R., Downes, D., Schneps, M. H., Reid, M. J., Moran, J. M., Kogan, L. R., Kostenko, V. I., Matveyenko, L. I. and Ronnang, B. 1981, ApJ, **247**, 1039.

Goldreich, P., and Kwan, J. 1974, ApJ, **189**, 441

Gordon, M. A., Jewell, P. R., Kaftan-Kassim, M. A., and Salter, C. J., 1986, ApJ, **308**, 288.

Gordon, M. A., and Jewell, P. R. 1987, ApJ, **323**, 766.

Goss, W. M., and Tilanus, R. P. J. 1985 MNRAS, **215**, 197.

Gordon, M. A. 1988, ApJ, **331**, 509.

Greaves, J. S., White, G. J., Ohishi, M., Hasegawa, T. and Sunada, K. 1992, A&A, **260**, 381.

Greenberg, J., M., 1989, in *IAU Symposium 135, Interstellar Dust*, ed. L. J. Allamandola and A. G. G. M. Tielens, (Kluwer Academic Publisher), p285.

Gwinn, C. R., Moran, J. M., and Reid, M. J. 1992, ApJ, **393**, 149.

Habe, A. and Ohta, K 1992, PASJ, **44**, 203.

Harvey, P. M., Campbell, M. H., and Hoffmann W. F. 1977, ApJ, **211**, 786.

Haschick, A., D., and Ho, P., T., P. 1990, ApJ, **352**, 630.

Iwashita, H., Morita, K., Tojo, A., and Akabane, K. 1984, ApJ, **283**, 117.

Hasegawa, T., Morita, K-I., Okumura, S., Kaifu, N., Suzuki, H., Ohishi, M., Hayashi, M., and Ukita, N. 1986, in *Masers, Molecules, and Mass outflows in Star-Forming regions* , ed. A. D. Haschick (Westford, MA: Haystack Observatory), p.275.

Hasegawa, T., Sato, F., Whiteoak, J. B., and Miyawaki, R. 1994, ApJ, **429**, L77..

Hayashi, M., Hasegawa, T., Omodaka, T., Hayashi, S. S., and Miyawaki, R. 1987, ApJ, **312**, 327.

Hayashi, M., Sunada, K, Hasegawa, T., Ohashi, N. , Kawabe, R., and Fukui, Y. 1991, in *Haystack Observatory Conference on the Interstellar Medium: Skylines – Atoms, Ions and Molecules – New Results in Spectral Line Astrophysics*, eds. A. D. Haschick and P. T. P. Ho, p223.

Hayashi, M., Ohashi, N., and Miyama, S. M. 1993, ApJ, **418**, L71.

Hayashi, M., Hasegawa, T., Ohashi, N., and Sunada, K. 1994, ApJ, **426**, 234.

Helou, G. 1989, in *IAU Symposium 135, Interstellar Dust*, ed. L. J. Allamandola and A. G. G. M. Tielens, (Kluwer Academic Publisher) p285.

Herbig, G. 1962, *Advance Astron. Astrophys.*, **1**, 47.

Herbst, E., Miller, T. J., Wlodek, S., and Bohme, D. K. 1989, A&A, **222**, 205.

Hildebrand, R. H. 1983, *Quart, J. R. A. S.*, **24**, 267.

Ho, P. T., and Haschick, A. D. 1981, ApJ, **248**, 622.

Ho, P. T., Klein, R. I., and Haschick, A. D. 1986, ApJ, **304**, 501.

Hobbs, R. W., Modali, S. B., Maran, S. P. 1971, ApJ, **165**, L87.

Hoffmann, W. F., Frederick, C. L., Emerry, R. J. 1971, A&A, **170**, L89.

Iglesias, E. R., and Silk, J. 1978, ApJ, **226**, 851.

Jackson, J. M., and Kraemer, K. E. 1994, ApJ, **429**, L37.

Jaffe, D. T., Harris, A. I., and Genzel, R. 1987, ApJ, **316**, 231.

Jaffe, D. T., Genzel, R., Harris, A. I., Lugten, J. B., Stancey, G. J. and Stutzki, J. 1989, ApJ, **344**, 265.

Jog, C. J., and Ostriker, J. P., 1988, ApJ, **328**, 404.

Johnston, K. J., and Hansen, S. S. 1982 AJ, **87**, 803.

Joseph, R., D., and Wright, G., S. 1985, MNRAS, **214**, 87.

Kaifu, N., Suzuki, S., Hasegawa, T., Morimoto, M., Inatani, J., Nagane, K., Miyazawa, K., Chikada, Y., Kanzawa, T., and Akabane, K. 1984, A&A, **134**, 7.

Kane, B. D., Clemens, D. P., Barrainis, R., and Leach, R. W., 1993, ApJ, **411**, 708.

Kazes, I., and Nguyen-Quang-Rieu. 1970 A&A, **4**, 111.

Keel, W., C., Kennicutt, R., C., Hummel, E., and van der Hulst J., M., 1985, AJ, **90**, 708.

Kent, S. R., and Mutel, R. L. 1982, ApJ, **263**, 145.

Kerr, F. L., and Lynden-Bell, D. 1986, MNRAS, **221**,1023.

Keto, R. E., Ho, P. T. P., and Haschick, A. D. 1987, ApJ, **318**, 712.

Keto, R. E., and Ho, P. T. P. 1988, ApJ, **324**, 920.

Keto, R. E., and Lattanzio, J. C. 1989, ApJ, **346**, 184.
Keto, R. E., Lattanzio, J. C., and Monaghan, J. J. 1991, ApJ, **383**, 639.
Klein, R. I., Sanford, M. T. II., and Whitaker, R. W. 1983, ApJ, **271**, L69.
Klein, R. I., Whitaker, R. W., and Sanford, M. T. II. 1985, in *Protostars and Planets II*, eds. D. C. Black and M. S. Mathews (Tucson: University of Arizona Press), p.340.
Koike, C., Hasegawa, H., and Hattori, T. 1987, *Ap. Space Sci.*, **134**, 95.
Kutner, S. R., and Mutel, R. L. 1982, ApJ, **263**, 145.
Kwan, J., and Valdez, F. 1983, ApJ, **245**, 465.
Langer, W. D., and Glassgold, A. E. 1990, ApJ, **352**, 123.
Langer, W. D., and Penzias, A. A. 1990, ApJ, **357**, 477.
Larson, R. B., and Tinsley, B. M. 1978, ApJ, **219**, 46.
Larson, R. B. 1981, MNRAS, **194**, 809.
Larson, R. B. 1986, MNRAS, **218**, 409.
Larson, R. B. 1987, in *Starbursts and Galaxy Evolution* , eds. T. X. Thuan, T, Montmerle, and J. T. T. Van (Editions Frontieres, France: Gif Sur Yvette), p.467.
Lattanzio, J. C., Monaghan, J. J., Pongracic, H., and Schwarz, M. P. 1985, MNRAS, **215**, 125.
Lattanzio, J. C., and Henriksen, R. N. 1988, MNRAS, **232**, 565.
Leung, C. M., Kutner, L., and Mead, L. 1982, ApJ, **262**, 583.
Levinson, F. H., and Roberts, W. W. 1981, ApJ, **245**, 465.
Linke, R. A. and Goldsmith, P. F. 1980, ApJ, **235**, 437.
Lis, D. C. and Goldsmith, P. F. 1990, ApJ, **356**, 195.
Listz, H. S., and Burton, W. B., 1981, ApJ, **243**, 778.
Little, S. J., Gullixson, C. G., Dietz, R. D. Hackwell, J, A., Gehrz, R. D., and Grasdalen, G. L. 1989, **AJ.**, **97**, 1716.
Lowenstein, R. F. *et al.* 1977, *Icarus*, **31**, 315.
MacLaren, I., Richardson, K. M., and Wolfendale, A. W. 1988, ApJ, **333**, 821.
Mac Low, M.-M., van Buren, D., Wood, D.O. S., and Churchwell, E. 1991, ApJ, **369**, 395.
Madden, S. C., Irvine, W. M., Matthews, H. E., Brown, R. D., and Gadfrey, P. D. 1986, ApJ, **300**, L79.
Maeder, A., and Meynet, G. 1987, A&A, **182**, 243.
Malkamäki, L., Sandell, G., Mattila, K., and Gebler, K.-H. 1979, A&A, **71**, 198.
Maloney, P. 1990, ApJ, **348**, L9.
Martin, R. N., and Barrett, A. H. 1978, ApJS, **36**, 1.
Martin-Pintado, J., Wilson, T. L., Gardner, F. F., and Henkel, C. 1985a, A&A, **142**, 131.
Martin-Pintado, J., Wilson, T. L., Johnston, K. J., and Henkel, C. 1985b, ApJ, **299**, 386.
Martin-Pintado, J., Bachiller, R., and Fuente, A. 1992, A&A, **254**, 315.

Mathis, J.S., and Whiffen, G., 1989, ApJ, **341**, 808.
Matthews, H. E., and Irvine, W. M., 1985, ApJ, **298**, L21.
Matthews, H. E., Madden, S. C., Avery, L. W., and Irvine, W. M., 1985, ApJ, **307**, L69.
Mezger, P. G., and Henderson, A. P. 1967, ApJ, **147**, 471.
Mezger, P. G., Schraml, J., and Terzian, Y. 1967, ApJ, **150**, 807.
Mezger, P. G., and Smith 1977, in *Proceeding of IAU Symp. No.75* , eds. Jonge and Maeder, (Reidel), p.133..
Mikami, H., Umemoto, T., Yamamoto, S., and Saito, S. 1992, ApJ, **392**, L87.
Miyama, S. 1992, PASJ, **44**, 193.
Miyawaki, R., Hayashi, M., and Hasegawa, T. 1986, ApJ, **305**, 353.
Miyawaki, R., Hasegawa, T., and Hayashi, M. 1988, PASJ, **40**, 69.
Miyawaki, R., Hayashi, M., and Hasegawa, T. 1990a, in *Submillimeter Astronomy* , ed. G. D. Watt and A. S. Webster, (Kluwer Academic Publisher), p279.
Miyawaki, R., and Hayashi, M. 1992 PASJ, **44**, 557.
Miyawaki, R., Hayashi, M., and Hasegawa, T. 1992, in *Proceeding of IAU Colloquium 140 Astronomy with Millimeter and Submillimeter Wave Interferometry* p251..
Miyawaki, R., Hasegawa, T., Sato, F., Whiteoak, J. B., and Kobayashi, H. 1994, in preparation.
Morimoto, M., Ohishi, M., and Kanzawa, T. 1985, ApJ, **288**, L11.
Morita, K-I., Hasegawa, T., Ukita, N., Okumura, S. K., and Ishiguro, M. 1992, PASJ, **44**, 373.
Morris, M., 1976, ApJ, **210**, 100.
Mufson, S. L., and Liszt H. S. 1977, ApJ, **212**, 664.
Myers, P. C., and Goodman, A. A. 1988, ApJ, **329**, 392.
Myers, P. C., Linke, R. A., and Benson, P. J. 1983, ApJ, **264**, 517.
Myers, P. C., and Benson, P. J. 1983, ApJ, **266**, 309.
Myers, P. C. 1983, ApJ, **270**, 105.
Myers, P. C. 1983, in *Protostars and Planets II*, eds. D. C. Black and M. S. Mathews (Tucson: University of Arizona Press), p81.
Myers, P. C., Fuller, G. A., Mathieu, R. D., Beichman, C. A., Benson, P. J. and Schild, R. E. 1987 ApJ, **319**, 340.
561.
Nakamura, A., Kawabe, R., Kitamura, Y., Ishiguro, M., Murata,, Y., and Ohashi, N. 1991, ApJ, **383**, L81.
Nakano, T. 1989, ApJ, **345**, 464.
Nakano, T., Hasegawa, T., and Norman C. A. 1994, ApJ, submitted.
Noguchi, M. 1987, MNRAS, **228**, 635.
Noguchi, M. 1988, A&A, **203**, 259.

Novak, G., Gonatas, D. P., Hildebrand, R. H., and Platt, S. R. 1989, ApJ, **345**, 802.
Nyman L. Å. 1983, A&A, **120**, 307.
Nyman L. Å. 1984, A&A, **141**, 323.
Nyman L. Å., and Miller, T. J. 1989, A&A, **222**, 231.
Ohashi, N., Kawabe, R., Hayashi, M., and Ishiguro, M. 1991, AJ, **102**, 2054.
Omodaka, T., Kobayashi, H., Kitamura, Y., Nakano, M., and Ishiguro, M. 1992, PASJ, **44**, 447.
Pajot, F., Gisport, R., Lamarre, J. M., Peyturaux, R., Puget, J. L., Serra, G., Coron, N., Dambier, G., Leblanc, J., Moalic, J. P., Renault, J. C., and Vitry, R., 1986, A&A, **154**, 55.
Pauliny-Toth, I. I. K., Wade, C. M., and Kerr, F. J., 1967, ApJS, **13**, 65.
Phillips, T. G., Knapp, G. R., Huggins, P. J., Werner, M. W., Neugebouer, G., and Ennis, D. 1981, ApJ, **245**, 512.
Radahakrishnan, V. Goss, W. M., Murray, J. D., and Brook, W., 1972, ApJS, **203**, 49.
Raimond, E., and Eliasson, B. 1969, ApJ, **155**, 817.
Reid, M. J., Haschick, A. D., Burke, B. F., Moran, J. M., Johnston, K. J., and Swenson, G. W. 1980, ApJ, **239**, 89.
Ronnang, B. 1988, ApJ, **330**, 809.
Reifenstein, E. C. III, Wilson, T. L., Burke, B. F., Mezger, P. G., and Altenhoff, W. J. 1970, A&A, **4**, 357.
Rengarajan, T. N., Cheung, L. H., Fazio, G. G., Shvanandan, K., and McBreen, B. 1984, ApJ, **286**, 573.
Riegel, K. W., and Epstein, E. E. 1968, ApJ, **151**, L33.
Rieke, G. H., Harper, D. A., Low, F. J., and Armstrong, K. R., 1973, ApJ, **183**, L67.
Lebofsky, M. J., and Elston, R.1985, ApJ, **290**, 116.
Rieke, G. H., Lebofsky, M. J., and Walker, C. E., 1988, ApJ, **325**, 679.
Rouleau, F. and Martin, P. G. 1991, ApJ, **377**, 526.
Rudolph, A., Welch, W. J., Palmer, P., and Dubrulle, B. 1990, ApJ, **363**, 528.
Salpeter, E. E. 1955, ApJ, **121**, 161.
Salter, C.J., Emerson, D. T., Steppe, H., and Thum, C. 1989, A&A, **225**, 167.
Sanders, D. B., Scoville, N. Z., Young, J. S., Soifer, B. T., Schloerb, F. P., Rice, W. L., and Danielson, G. E. 1986, ApJ, **305**, L45.
Sanders, D. B., Scoville, N. Z., and, Soifer, B. T. 1991, ApJ, **370**, 158.
Sargent, A. I., Beckwith, S. V. W., Keene, J., and Masson, C. 1988, ApJ, **333**, 936.
Sato, F. , Akabane, K., and Kerr, F. J. 1967, *Australian J. Phys.* , **20**, 197.
Sato, F. 1968, PASJ, **20**, 303.
Sato, F. *et al.* 1994, in preparetion.
Scalo, J. M., and Pumphrey, W. A. 1982, ApJ, **258**, L29.

Scalo, J. M. 1986, *Fund. Cos. Phys.* , **11**, 1.
Schenewerk, M. S., Snyder, L. E., Hollis, J. M., Jewell, P. R., and Ziurys, L. M. 1988, ApJ, **328**, 785.
Schloerb, F. P., and Snell, R. L. 1987, ApJ, **319**, 426.
Schneps, M. H., Lane, A. P., Downes, D., Moran, J. M., Genzel, R., and Reid, M. J. 1981, ApJ, **249**, 124.
Schraml, J., and Mezger, P. G. 1969, ApJ, **156**, 269.
Schwarz, P. R., 1982, ApJ, **252**, 589.
Scoville, N. Z., and Solomon, P. M. 1973, ApJ, **180**, 31.
Scoville, N. Z., and Good, J. C. 1989, ApJ, **339**, 149.
Scoville, N. Z., Sargant, A. I., Sanders, D. B., Claussen, M. J., Masson, C. R., Lo, K. Y. and Phillips, T. G. 1986, ApJ, **303**, 416.
Scoville, N. Z., Sanders, D. B., and Clemens, D. P. 1986, ApJ, **310**, L77.
Scoville, N. Z., Yun, M. S., Sanders, D. B., and Waller, W. H. 1987, ApJS, **63**, 821.
Scoville, N. Z. 1991, in *Dynamics of Galaxies and Their Molecular Cloud Distributions*, eds. F. Combes and F. Casoli, pp315-322.
Seab, C. G., and Shull, J. M. 1983, ApJ, **275**,652.
Serabyn, E., Güsten, R., and Schulz, A. 1993, ApJ, **413**, 571.
Shu, F., Adams, F. C., and Lizano, S. 1987, ARA&A, **25**, 23.
Sievers, A. W., Mezger, P. G., Gordon, M. A., Kreysa, E., Haslam, C. G. T., and Lemke, R. 1991, A&A, **251**, 231.
Snell, R. L., and Loren, R. B. 1977, ApJ, **211**, 122.
Snell, R. L., Langer, W. D. and Frerking, M. A. 1982, ApJ, **255**, 149.
Snyder, L.E., and Buhl, D. 1975, ApJ, **201**, L31.
Soifer, B. T., Rowan-Robinson, M., Houck, J. R., de Jong, T., Neugebauer, G., Aumann, H. H., Beicheman, C. A., Boggess, N. Clegg, P. E., Emerson, J. P., Gillett, Habing, H. J., Hauser, M. G., Low, F. J., Miley, G., and Young, E. 1984, ApJ, **278**, L71.
Solomon, P. M., Sanders, D. B., and Rivolo, A. R. 1985, ApJ, **292**, L19.
Solomon, P. M., Rivolo, A. R., Barrett, J. W., and Yahil, A. M. 1987, ApJ, **319**, 730.
Solomon, P. M., Sage, L. 1988, ApJ, **334**, 613.
Stark, A. A., 1984, ApJ, **281**, 624.
Stark, A. A., and Brand, J., 1989, ApJ, **339**, 763.
Sugitani, K., Fukui, Y., Mizuno, A., and Ohashi, N. 1989, ApJ, **342**, L87. Sume, A., and Irvine, W. M. 1977, A&A, **60**, 337.
Swade, D. A. 1989, ApJ, **345**, 828.
Tamura, M., 1994, in preparetion.
Tatematsu, K., Umemoto, T., Kameya, O., Hirano, N., Hasegawa, T., Hayashi, M., Iwata, T., Kaifu, N., Mikami, H., Murata, Y., Nakano, M., Nakano, T., Ohashi, N., Sunada, K., Takaba, H., and Yamamoto, S. 1993, ApJ, **404**, 643.

Tenorio-Tagel, G., 1979, A&A, **71**, 59.
Tielens, A. G. G., in *IAU Symposium 135, Interstellar Dust*, ed. L. J. Allamandola and A. G. G. M. Tielens, (Kluwer Academic Publisher) p239.
Tinney, C. G., Scoville, N. Z., Sanders, D. B. and Soifer, B. T., 1990, ApJ, **362**, 473.
Turner, B. E. 1984, *Vistas in Astronomy*, **27**, 303.
Ulich, B. L., and Haas, R. W. 1976, ApJS, **30**, 247.
Ulich, B. L., Dickel, J. R., and dePater, I. 1984, *Icarus*, **60**, 590.
van Gorkom, J. H., Goss, W. M., Sharer, P. A., Schwarz, U. J., and Harten, R. H. 1980, A&A, **89**, 150.
van Buren, D., and M-M., Mac Low, 1992, ApJ, **394**, 534.
Walker, R. C., Johnston, K. J., Burke, B. F., and Spencer, J. H. 1977, ApJ, **211**, L135.
Walker, R. C., Matsakis, D. N., and Garcia-Barreto, J. A. 1982, ApJ, **255**, 128.
Ward-Thompson, D., and Robson, E. I. 1990, MNRAS, **244**, 458.
Welch, W. J., and Marr, J. 1987, ApJ, **317**, L21.
Welch, W. J., Dreher, J., Jackson, J., Terebey, S., and Vogel, S. 1987, *Science* , **238**, 1550.
Welch, W. J. 1990, in *Submillimeter Astronomy* , ed. G. D. Watt and A. S. Webster, (Kluwer Academic Publisher), p81.
Westbrook, W. E., Werner, M. W., Elias, J. H., Gerzari, D. Y., Hauser, M. G., Lo, K. Y., and Neugebouer, G. 1976, ApJ, **209**, 94.
Westerhout, G. 1958, *Bull.Astr.Inst.Netherlands* , **14**, 215.
Whittet, D. C. B., 1988, in *Dust in the Universe*, eds. Baily, M. E., and Williams, D. A., (Cambridge University Press), p25.
Wink, J. E., Altenhoff, W. J., and Webster, W. J., Jr. 1975, A&A, **38**, 109.
Wood, D. O. S., and Churchwell, E. 1989a, ApJ, **340**, 265.
Wood, D. O. S., and Churchwell, E. 1989b, ApJS, **69**, 831.
Woodward, C. E., Helfer, H. L., and Phpher, J. L. 1984, MNRAS, **209**, 209.
Wooten, A. H., Sargent, A., Knapp, G., and Huggins, P. J. 1983, ApJ, **269**, 147.
Wright, M. C. H., Plambeck, R. L., Vogel, S. N., Ho, P. T. P., Welch, W. J. 1983 ApJ, **267**, L41.
Wright, E. L. 1987, ApJ, **320**, 818.
Wynn-Willams, C. G. 1969, MNRAS, **142**, 587.
Wynn-Willams, C. G. 1987, in *IAU Symposium 115, Star Forming Regions* , ed. M. Peimbert, J. Jugaku, (Dordrecht: Reidel), 587.
Yamamoto, S., Mikami, H., Saito, S., Kaifu, N., Ohishi, M., and Kawaguchi, K. 1992, PASJ, **44**, 459.
Yorke, W., Tenorio-Tagle, G., and Bodenheimer, P., 1983, A&A, **127**,313.
Young, J., S., Kenny, J., D., Tacconi, L., Claussen M., J., Huang Y., L., Tacconi-Garman L., Xie, S., and Schloerb, F., P. 1986, ApJ, **311**, L17.
Ziurys, L. M., Snell, R. L., and Dickman, R. L. 1989, ApJ, **341**, 857.
Ziurys, L. M., Friberg, P., and Irvine, W., M. 1989, ApJ, **343**, 201.